공학박사 학위논문

레이저로 유도되는 마이크로젯을 활용한 경피 약물 전달 시스템

A Transdermal Drug Delivery System Based on Laser-generated Microjet

2017년 8월

서울대학교 대학원

기계항공공학부

장 헌 재

레이저로 유도되는 마이크로젯을 활용한 경피 약물 전달 시스템

A Transdermal Drug Delivery System Based on Laser-generated Microjet

지도 교수 여 재 익

이 논문을 공학박사 학위논문으로 제출함

2017년 5월

서울대학교 대학원

기계항공공학부

장 헌 재

장헌재의 공학박사 학위논문을 인준함

2017년 6월

위 원 장 _____ (인)

부위원장 _____ (인)

위 원 _____ (인)

위 원 _____ (인)

위 원 _____ (인)

Abstract

A Transdermal Drug Delivery System Based on Laser-generated Microjet

Hun-jae Jang

Mechanical and Aerospace Engineering

The Graduate School

Seoul National University

Needle syringe injection is a widely used transdermal drug delivery method because of its low cost and high efficiency. However, needle syringes have disadvantages such as affliction of needle phobia and pain, generation of medical waste, and potential contamination due to reuse. Therefore, there is a need for an alternative that will replace the existing needle-based drug delivery system.

The transdermal drug delivery systems penetrate the skin barrier using various chemical or physical processes including diffusion and permeation. Among them, use of liquid jet has attracted significant attention as one of the effective drug delivery methods. Unexpectedly, the liquid injection method has the potential for cross-contamination due to splash back during injection. Furthermore, if the liquid jet dose not have high speed and narrow cross-

section, this method yields poor reliability in terms of delivering correct dosage at appropriate depth as well as insignificant or no reduction in pain.

In the current study, a breakthrough in the efficient transdermal drug delivery of a laser-generated microjet has been reported. Such a microjet injector systems accelerate and deliver drugs without needles to overcome the weaknesses of traditional jet injectors. For example, microjets with reduced jet diameter and jet volume per pulse and repetitive injection have been implemented in order to achieve better performance in terms of the reliability by controlling the penetration depth and delivered drug dose.

Simultaneously, a detailed analysis of the injection mechanism was carried out by studying the process of bubble growth and drug release with a high speed camera. The high speed visualization provided an improved understanding of the basic driving mechanism of the microjet injector developed in this study. The efficiency of the present drug delivery scheme was also evaluated by injection tests on animal skin.

In conclusion, all aspects of the drug delivery system have been discussed. The study achieves the enhancements in microjet ejection and repetitive jet generation process, making the injector suitable for general clinical applications. The reported results provide a design guideline to build a reliable and functionally optimized microjet injector system.

Keywords: Drug delivery, Transdermal injection, Pain reduction, Microjet, Laser, Bubble dynamics

Student Number: 2011-20747

Contents

List of Tables

List of Figures

Preface

This thesis is based on the following publications and manuscripts.

Paper 1

Mi-ae Park, Hun-jae Jang, Fedir V. Sirotskin and Jack J. Yoh. Er:YAG laser pulse for small-dose splashback-free microjet transdermal drug delivery. Optics Letters, 2012, 37.18

Paper 2

Hun-jae Jang, Mi-ae Park, Fedir V. Sirotskin and Jack J. Yoh. Laser-induced microjet: wavelength and pulse duration effects on bubble and jet generation for drug injection. Applied Physics B, 2013, 113.3

Paper 3

Hun-jae Jang, Hyeonju Yu, Seonggeun Lee, Eugene hur, Yoonkwan Kim, Seoul-Hoon Lee, Naegyu Kang and Jack J. Yoh. Towards clinical use of a laser induced microjet system aimed at reliable and safe drug delivery. Journal of Biomedical Optics, 2014, 19.5

.

Paper 4

Hun-jae Jang, Eugene Hur, Yoonkwan Kim, Seol-Hoon Lee, Nae G. Kang and Jack J. Yoh. Laser-induced microjet injection into preablated skin for more effective transdermal drug delivery. Journal of Biomedical Optics, 2014, 19.11

Paper 5

Jack J. Yoh, Hun-jae Jang, Mi-ae Park, Tae-hee Han, Jung-moo Hah. A bio-ballistic micro-jet for drug injection into animal skin using a Nd:YAG laser. Shock Waves, 2016, 26.1

Paper 6

Hun-jae Jang, Seonggu Yeo and Jack J. Yoh. Synchronization of skin ablation and microjet injection for an effective transdermal drug delivery. Applied physics A, 2016, 122.4

Paper 7

Hun-jae Jang, Seonggu Yeo and Jack J. Yoh. Skin pre-ablation and laser assisted microjet injection for deep tissue penetration. Lasers in Surgery and Medicine, 2016

Chapter 1. Introduction

Transdermal drug delivery method based on needle syringe has been widely adopted because of its low cost and high efficiency. However, the use of needle syringe has known drawbacks such as affliction of needle phobia, site lesions, pain associated with the invasive procedure, disposal of medical waste, possible contamination from reuse of needles. Therefore, there have been calls for an alternative for the conventional needle-based drug delivery system by overcoming already acknowledged drawbacks.

Still, percutaneous drug delivery is one of the most effective method and it can be improved by understanding the skin structure. Human skin can be divided into three layers: stratum corneum, the viable epidermis and the dermis. The thickness of these layeres are 10-20 μm, 50-100 μm and 1-2mm, respectively. The stratum corneum which is main obstacle to deliver drug is the physical and chemical barrier composed of dead cells and free of blood vessels and verves. The amount of blood vessels and nerves increases with the penetration depth and significantly increases in dermis. Viable epidermis contains relatively small amount of blood vessels and nerves. Therefore, the significant reduction of the pain with acceptable delivery efficiency can be achieved when a drug is delivered into the viable epidermis. The key to this approach is the need for external forces breach the skin barrier, called stratum corneum.

The transdermal drug delivery systems penetrate the skin barrier using

various chemical or physical processes including diffusion and permeation. Among them, use of liquid jet has attracted significant attention as one of the efficient drug delivery methods. Because this needle free drug delivery system is expected to overcome the disadvantages of needle syringes. However, contrary to expectations, liquid jet injectors have the potential for cross-contamination from splash-back during injection. Furthermore, if the liquid jet dose not have high speed and narrow cross-section, resulting in poor reliability in terms of delivering correct dosage at appropriate and depth as well as insignificant or no reduction in pain.

As an improvement, microjet is adopted for safe and efficient drug delivery. Several different mechanisms of generating the microjet range from spring, compressed gas, piezoelectric transducer, linear Lorentz force piston, electronic driven bubble, and laser-induced wave or bubble. In the spring or gas-powered devices, it is difficult to control drug dose or jet speed with its piston unit, whereas in the piezoelectric transducer, rather precise control of drug dose was deemed possible. The Lorentz force driven injector has shown quite reliable performance in comparison to aforementioned devices.

In currnet study, laser-generated microjet is chosen to solve potential concerns addressed by the medical practitioners. The injector design is evolved around the use of two separate chambers that independently contain driving water (in the upper chamber) and drug (in the lower reservoir), separated by a thermally resistant silicon rubber membrane. The laser ablation occurs within the upper driving chamber only, while the drug solution beneath the membrane is protected from the laser ablation. The strong bubble

generation in the driving chamber gives rise to an elastic deformation of the membrane which then causes an instantaneous ejection of the drug solution from a drug reservoir through a narrow micro nozzle. The microjets with a reduced jet diameter and volume per pulse, and repetitive injections have been implemented in order to achieve better performance in terms of the reliability by controlling the penetration depth and delivered drug dose.

Simultaneously, a careful analysis of the injection mechanism was carried out by studying the process of bubble expansion and microjet ejection with high speed camera. Furthermore, bubble motion in confined condition was analyzed to describe real bubble behavior inside of microjet injector. The efficiency of the present drug delivery scheme was also evaluated by injection tests on animal skin.

In conclusion, all aspects of the system including laser parameters effects on bubble growth, microjet generation and skin penetration aspects, repetitive and reliable microjet generation, bubble expansion in confined condition, laser-assisted drug delivery system have been discussed. The reported results provide a design guideline to build a reliable and functionally optimized non-invasive transdermal drug delivery system based on laser-generated microjet.

Chapter 2. Experimental Apparatus

Laser induced microjet is necessary to apply transdermal injection. In this study, drug delivery system based on microjet is introduced to transfer various type of drug into tissue. Microjet is accelerated up to 100 ~ 200m/s with narrow diameter by using focused laser beam in water. Explosive phase change occurs inside of microjet injector and this bubble expansion is main power source to release drug as microjet. The high speed camera provided good understand characteristics of bubble and microjet behavior as main diagnostic tool.

2.1 Laser

Powerlite (Continuum Inc.) and Spectra (Lutronic Corp.) Q-switched Nd:YAG laser are used as driving sources for microjet generation. Action (Lutronic Corp.) and Anybeam (B&B sys. Corp.) Er:YAG laser are also used. Powerlite emits a laser pulse at maximum 3 J with 1064 nm wavelength, 9 ns duration. Spectra emits dual wavelength laser beams of 1064 and 532 nm with 7 ns pulse width. Maximum energy is 1200 and 400 mJ at 1064 and 532 nm, respectively. Action emits a laser pulse at maximum 2.2J with 2940nu wavelength, 250 μs duration. Anybeam emits a laser pulse at maximum 1J with 2940 nm wavelength and there is a variable laser pulse mode with intervals of 50 μs from 100 to 300 μs.

Fig. 2.1. Image of Powerlite, Continuum Inc.

Fig. 2.2. Images of Spectra (left) and Action (right), Lutronic Corp.

Fig. 2.3. Image of Anybeam, B&B sys. Corp.

2.2 High Speed Camera

Phantom v711 (Komi Corp.) high speed camera is used to capture the bubble and microjet motion. Widescreen 1280x800 CMOS sensor allows long time tracking of moving targets. 7,500 frames per second is possible at full resolution and maximum shooting speed is 1,400,000 (fast option). The standard exposure time is 1μs and optional 300ns exposure time mode is also available.

Fig. 2.4. Image of phantom, Komi Corp.

2.3 Microjet Injector

Microjet injector can be divided into two areas. The first area consists of transparent window and chamber. This window prevents the liquid in the chamber from escaping while allowing the laser beam to pass through and water is contained inside of chamber. Explosive phase change due to focused laser beam occur inside of chamber. The second part is composed of membrane and nozzle as the space filled with the drug. Water in chamber and drug in nozzle are separated by elastic membrane. This membrane transport generated momentum from chamber to nozzle while prohibit unfavorable heat transfer. . Chamber is sealed with M4 screw and O-ring to prevent any drug contamination problems and the volume of drug reservoir is 327 mm^3 (327μL).

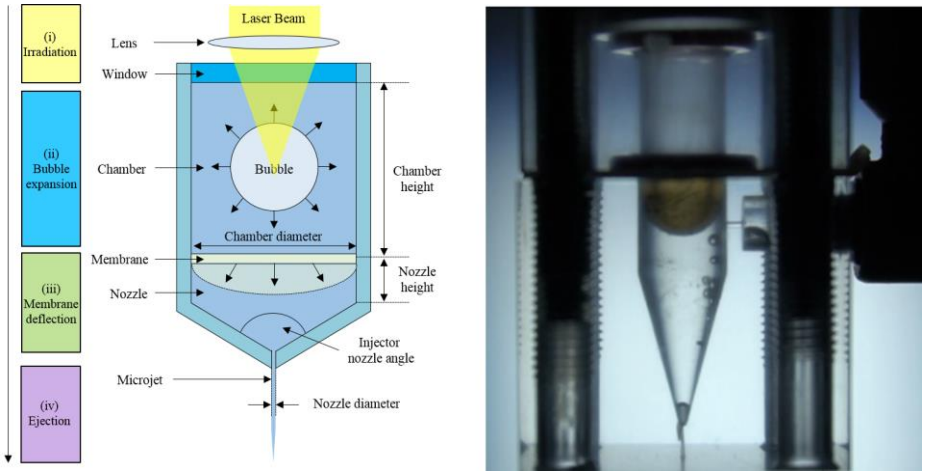

Fig. 2.5. Schematic and images of microjet injector

Chapter 3. Characteristics of Laser-generated Microjet

3.1 Bubble and Microjet Characteristics Generated by Laser

3.1.1 Background and Motivation

The use of needle-free injection may potentially remedy known drawbacks such as needle phobia and possible contamination from reuse of needles[1-3]. A drug delivery system based on the microjet can penetrate topmost skin layer by using the kinetic energy of a microjet[4, 5].

Generation of a microjet is possible in several ways. Use of an actuator based on spring, gas powered, Lorentz-force, piezoelectric element, or laser has been reported [2, 4-6]. We revisit the laser-induced microjet injector [5, 6] where a laser beam is focused inside a small container filled with water. A bubble forms upon the laser irradiation, and expansion of the bubble pushes the membrane separating drug from driving liquid, causing fast ejection of the drug. The discharged liquid forms a jet with the typical velocity in 20–100 m/s range. The dynamics of bubble depends on laser parameters such as wavelength and pulse duration [7-9]. In particular, the resulting penetration depth, which determines performance of the microjet injector, depends on the jet velocity and jet length.

In this study, Nd:YAG and Er:YAG lasers are compared for analyzing the

efficiency of the microjet device. The paper is divided into two parts. First part deals with dynamics of bubble generated by the laser beams of different wavelength and pulse duration. Both dimensional and dimensionless analyses are used to understand the dependence of bubble characteristics on the laser parameters by using images taken from high-speed camera. Second part deals with the characteristics of jets and their relation to the driving bubble that allows the microjet ejection for drug delivery.

3.1.2 Experimental Approach

Two experiments that are performed are (1) formation and evolution of the laser-induced bubble in a water tank and (2) generation of the microjet. The applied lasers used are skin treatment lasers (Spectra Nd:YAG and Action Er:YAG by Lutronics Co., Korea). In both experiments, we use the same laser energy of 408 mJ, while wavelength and the pulse duration are kept different. The Nd:YAG laser has wavelength of 1064 nm and the pulse duration of 7 ns, while the Er:YAG laser has 2940 nm wavelength and pulse duration of 250 μs. Both lasers have built-in focusing system with focal length of 78 mm (Nd:YAG) and 67 mm (Er:YAG). The high-speed camera Phantom V710 is used for visualization.

In the first experiment, the laser is focused into the water tank of 10 × 5.5 × 5.5 cm in dimension. The difference in wavelength leads to a different penetration depth $\delta_p = 1/\alpha$, where α is the absorption coefficient. For the

given wavelength, the optical penetration depths are 1.65 cm and 0.8 μm for Nd:YAG and Er:YAG, respectively [10]. Because of high water absorption in Er:YAG case, the bubble forms near to the water surface. In order to isolate the bubble from ambient air, the interface is kept separate by a glass (MgF2) window. The process of bubble development is recorded by the high-speed camera at 90,909 fps in the Nd:YAG case and at 28,986 fps in the Er:YAG case.

A schematic of the microjet injector experiment is given in Fig. 3.1. The laser is focused inside of the chamber which contains a driving liquid (water). The generated bubble gives rise to chamber pressure and pushes the elastic membrane which separates the drug reservoir underneath the membrane from upper driving liquid chamber. The membrane deflection pushes the drug out of the reservoir through a nozzle. The discharging liquid forms a jet. The process of microjet development is recorded by a high speed camera at 37,016 fps in the Nd:YAG case and at 42,001 fps for the Er:YAG case, respectively.

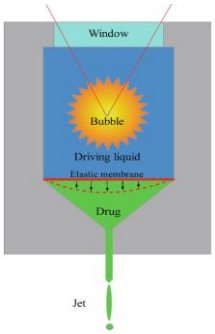

Fig. 3.1. Schematic of the microjet generation experiment using an injector with 150μm nozzle.

3.1.3 Results and Discussion

The bubble dynamics is essential for the present microjet device. The expansion of the bubble starts with the formation of an initial nucleus. The nucleus is formed at a spot where the optical breakdown occurs. The energy of the laser pulse per unit area increases toward the focal point and the laser energy density reaches breakdown threshold at some distance. The shape of the bubble nuclei is far from spherical because it is affected by the spherical aberrations [11].

The behavior of the bubble triggered by the Er:YAG beam is distinct from that of Nd:YAG. Since the optical penetration depth is much shorter for Er:YAG laser, the beam cannot penetrate deeper into the water. Instead, the bubble starts growing from the water surface. A transparent window is used to keep the vapor from escaping and to prevent the pressurized gas inside the bubble from interacting with the water surface.

The sequential images of the bubble development in both cases are given in Fig. 3.2. The temporal evolution of the bubble radius is given in Fig. 3.3 with black dots where vertical bars illustrate the error. The behavior of the bubble which is triggered by Nd:YAG laser is typical to that observed in many studies, while Er:YAG case is seemingly distinct.

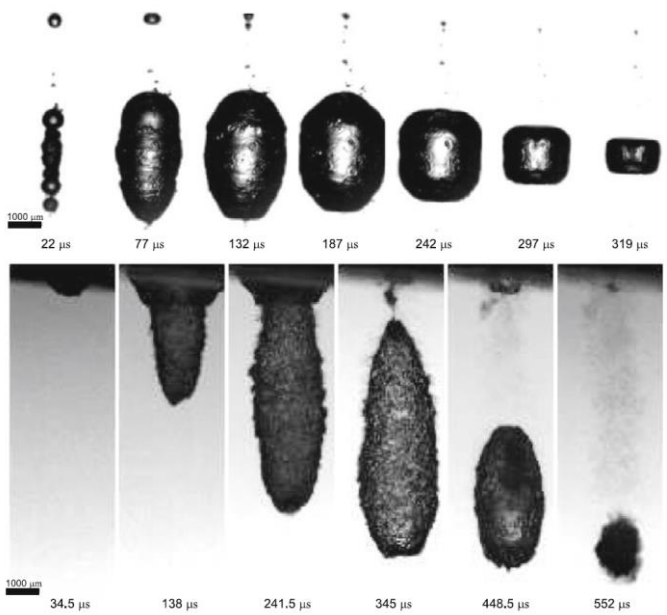

Fig. 3.2. Sequential images of bubble expansion for Nd:YAG (top panels) and Er:YAG (bottom panels) cases

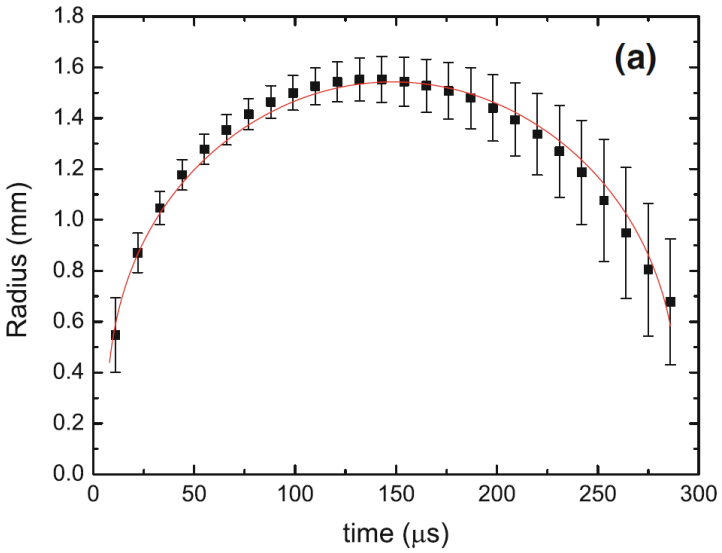

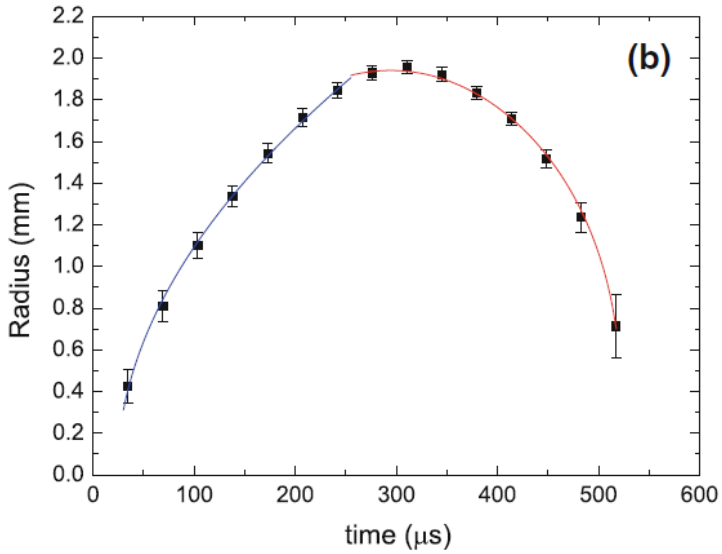

Fig. 3.3. Measured bubble radius as function of time for Nd:YAG (a) and Er:YAG (b) cases with analytical approximation given by the *solid line*

The temporal dependence of the radius in Nd:YAG case can be approximated with a well-known equation:

$$R = R_{\max}\left[\sin\left(\frac{\pi(t-t_0)}{\tau_l}\right)\right]^{1/3} \qquad (3.1)$$

where τ_l = 249 ± 18 μs is the bubble lifetime, t_0 is the shift between the first captured image and the start of the bubble expansion. The high speed camera and the laser are not synchronized so that $t_0 \leq 27.02$ μs and $t_0 \leq 23.81$ μs in Nd:YAG and Er:YAG cases, respectively. The approximation given by Eq. (3.1) is illustrated in Fig. 3.3(a) with the solid red line. Maximum radius is

estimated as R_{max} = 1.53 ± 0.08 mm with Eq. (3.1)for the Nd:YAG case. The average velocity $\dot{R}$ can be estimated as

$$\dot{R} = 2\frac{R_{\max}}{\tau_l} \tag{3.2}$$

Using $\dot{R}$ and R_{max}, we estimate the inertia timescale τ_{in}

$$\tau_{in} = \frac{R_{\max}}{\dot{R}} \tag{3.3}$$

Combining (3.2) and (3.3) leads to τ_{in} = $0.5\tau_l$. For Nd:YAG case, the pulse duration is much shorter than the inertia timescale, so that the laser energy is assumed to be transformed (deposited) into the bubble energy instantly.

In Er:YAG case, the pulse duration τ = 250 μs is comparable with the bubble lifetime. The bubble reaches the maximum diameter when the laser pulse is over, so that formation of the bubble nuclei was observed during half of the life time. The detailed description of this stage requires explicit description of the processes such as absorption, ionization and recombination. However, we found that the temporal evolution of the radius during a pulse duration can be approximated by the following power-law dependence

$$R = C_R(t - t_0)^{1/2} \tag{3.4}$$

where C_R = 0.1253 ± 0.0009 and t0 = 23.8 ± 1 μs is the time shift between the first captured image and the start of the laser pulse. This dependence is illustrated in Fig. 3.3(b) with the solid blue line. The power in Eq. (3.4) is the same as in the Plesset and Prosperetti [12] equation which describes the temporal evolution of the vapor bubble:

$$R = \left(\frac{12}{\pi}\right)^{1/2} \frac{k_l}{L\rho_v} \frac{T_\infty - T_b}{D_l^{1/2}} t^{1/2} \tag{3.5}$$

where T_b is the boiling temperature, $\rho_v = \rho_v(T_b)$ is the equilibrium vapor density at the boiling temperature, L is the latent heat, D_l is thermal diffusivity and k_l is the conductivity. Adopting typical values of L, D_l, and k_l, we estimate T_∞ = 156℃. Therefore, the expansion of the bubble is similar to a vapor bubble which expands in superheated liquid. While initial stage is strongly affected by the thermal effects in Er:YAG case, the collapse of the bubble and its subsequent rebound is typical for cavitation bubble in both cases.

The mechanism of the jet formation in the microjet device can be described as follows. The laser is focused at the driving liquid (water) inside of a chamber, the laser induces formation of the bubble, the bubble expansion increases the pressure inside of the chamber, the increment of the pressure leads to the deflection of the elastic membrane and the membrane pushes the drug in the reservoir out through the nozzle. The discharging liquid forms a jet shown in Fig. 3.1. Figure 3.4(a), 3.4(b) are the sequential images of microjet

development for Er:YAG and Nd:YAG cases, respectively.

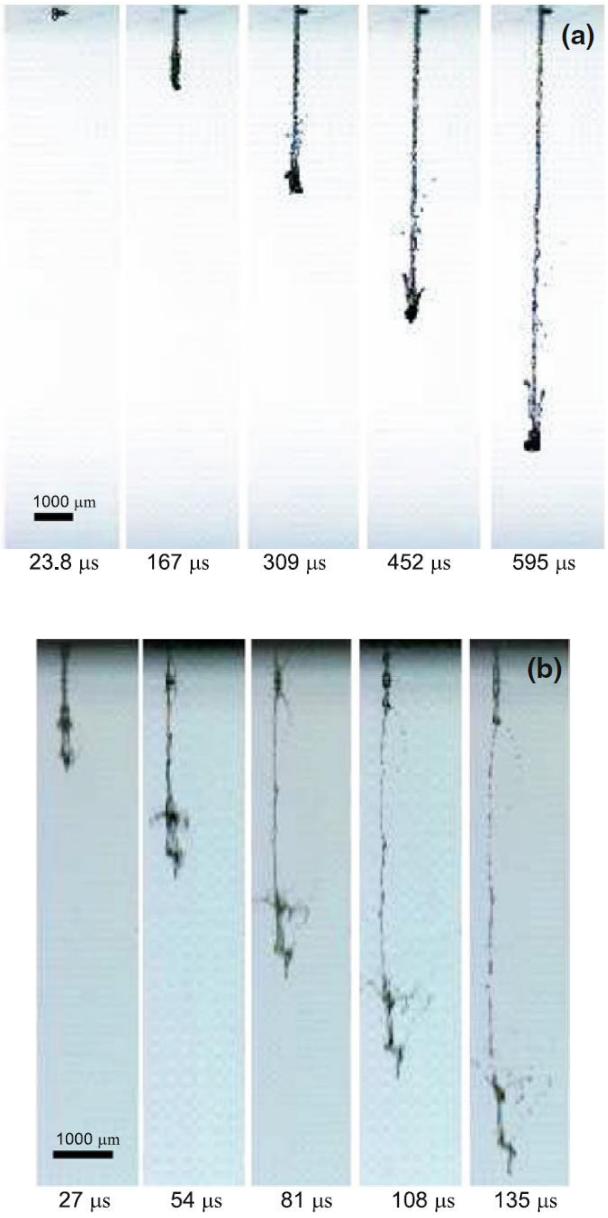

Fig. 3.4. Sequential images of microjet for Er:YAG (a) and Nd:YAG (b) cases

The velocity of the jet and breakup length are important parameters which determine the skin penetration ability when dealing with transdermal drug delivery. The average velocity of the jet generated by Nd:YAG laser is 74 ± 8 m/s while for Er:YAG case, the velocity is 28 ± 4 m/s. Since the main driving mechanism of the jet generation is bubble expansion, the difference in estimated jet velocity can be explained in terms of the average growth rate of the bubble. The average growth rate is twice higher when the bubble is triggered with Nd:YAG laser than that with Er:YAG one, while the life time is comparable. This leads to a higher pressure gradient in Nd:YAG case and consequently, to a higher jet velocity.

The microjet which is generated by Nd:YAG laser breakups into small drops earlier comparing to that for Er:YAG case. The ratio of breakup length to nozzle diameter is 36.9 ± 8.9 and 67.1 ± 0.4 for Nd:YAG and Er:YAG, respectively. The nozzle diameter is 150 μm. Such behavior of liquid jets imply that they belong to a common jet regime where the breakup length decreases with the jet velocity. In this regime, the aerodynamic force is the main factor which induces atomization process. Aerodynamic effects acting on the microjet can be seen from the jet head shape which is illustrated in Fig. 3.4(a) and 3.4(b).

3.2 Penetration Using Nd:YAG Laser-generated Microjet

3.2.1 Background and Motivation

In transdermal drug delivery systems, external forces breach the skin barrier (stratum corneum) and deliver drugs into the underlying viable epidermis [13-16]. While utilizing the kinetic energy of an accelerated jet via the ballistic method, microjets with a reduced jet diameter and jet volume achieve better performance in terms of the reliability of delivery dose and depth by reducing splash-back. Moreover, laser energy in the laser-based method can provide a faster jet, which would exceed speeds obtained by other means of generating microjets [6].

The outer dermal layer called the epidermis is an important site for painless drug delivery because it lacks blood vessels and sensory nerve endings. Systemic drug delivery through the skin has been used since the introduction of transdermal scopolamine patches for treating motion sickness [2]. This type of delivery creates micro-pores using several different methods, and drugs are delivered actively through the pores. A micro-needle patch has an array of microscopic needles which creates micron-scale pathways into the skin [13]. In other techniques, micro-pores are created via a vaporization process or the reversible disruption of lipid bilayer structures in the skin using electric pulses or ultrasound [13, 17].

Ballistic methods based on a liquid jet or a powder jet deliver drugs directly, with a reduced release time. Liquid jet injectors generate a high-velocity jet

with a small diameter of greater than 100 μm while powder jet injectors deliver drugs in their dry form. Contrary to expectations, liquid jet injectors have the potential for cross-contamination from splash-back during injection If the speed is not fast enough and is not a narrow jet, resulting in poor reliability of delivery dose and depth, and insignificant or no reduction in pain [18]. As an improvement, Arora et al. [16] introduced a piezoelectric transducer to generate a pulsed microjet. The microjet with a reduced injection diameter and volume improved jet performance but with a limited penetration depth of up to 200 μm. It is to be noted that the epidermal layer of the human skin extends from 100 to 400 μm below the outer layer and in the animal skin, particularly the guinea pig's abdominal skin, it extends from 40 to 200 μm.

A micro-jet injector (see Fig. 3.5) consists of a micro-nozzle with liquid drugs of various viscosities, a driving fluid with 3 % salt concentration, a heat-resistant flexible elastic membrane separating the liquid drug from the driving fluid and confinement glass. A high energy nanosecond infrared laser beam pulse generates a shock wave which is released in a few tens of microseconds upon the laser irradiation. Approximately 150 μs later, the diameter of the cavitation bubble in the driving fluid reaches its maximum before the bubble starts collapsing. The displaced volume of driving liquid, in correspondence with the degree of bubble expansion in the driving liquid, then pushes the elastic membrane separating the blue driving fluid from the yellow liquid drug (see Fig. 3.5(a)).

The resulting high pressure stretches the elastic membrane, and the drug

content inside the nozzle is squeezed out of the nozzle at high velocity, reaching 230 m/s before breakup. The instant pressure peak during the single laser pulse based cavitation process may reach several thousand bars, which results in 2–3 squirts of micro-jets within 150 μs. Previously, degassed water was successfully injected into 3–5 % gelatin samples and a pig fat tissue sample, verifying the feasibility of the needleless transdermal drug delivery scheme, which is both dose and depth controlled by a laser beam pulse [19].

In this study, we demonstrate that our method of laser based microjet drug delivery is capable of penetrating a guinea pig's skin tissue sample to deliver a controlled dose of a drug to the targeted region 10–400 μm beneath the outermost layer of the skin. Imaging of the skin after injection of fluorescein isothiocyanate and biotin revealed that the epidermal and dermal layers were stained well below 60 μm underneath the outer layer of the abdominal guinea pig's skin sample.

3.2.2 Experimental Approach

A Q-switched Nd:YAG laser beam was focused within the driving fluid by a set of three lenses (bi-convex: focal length 50 mm; plane-convex: focal length 145 mm; and plane concave: focal length 100 mm). Laser energy was varied from several hundred milli-joules up to 3 J to identify the optimal energy needed for delivery. Three percent salt water was used in the driving liquid chamber for maximization of atomic breakdown as well as for generation of

strong cavitation.

A gelatin gel was used as the skin model. The gelatin (Geltech Co. Ltd., Korea) of 60 bloom was dissolved in 70 ◦C water at 3–7 percent. The bloom number, a measure of surface tension, indicates the toughness of gels. Liquid gelatin samples were poured into a 4 × 4 × 4 cm3 acrylic box and cooled at 5 ◦C for 1 h.

The injection liquid was prepared by dissolving fluorescein isothiocyanate (FITC, 0.05 mg/ml) and biotin (0.1 mg/ml) in a dimethyl sulfoxide (DMSO) solution. Both FITC and biotin were used to verify the performance of micro-jet penetration. The positive controlled skin from the FITC test was analyzed using a fluorescence microscope (Nikon Eclipse Ti-U) and the immunohistochemistry (IHC) method was used to monitor the biotin staining of the skin layer.

A male Hartley guinea pig was purchased from Reference Biolabs (Seoul, Korea). The guinea pig was between 250 and 260 g in weight. A skin sample of the guinea pig abdomen was first disinfected in a phosphate-buffered saline (PBS) solution before sectioned into a 15×15 mm target. The skin was epilated with wax for 24 hours before sectioning. The prepared skin sample was affixed on a foam board with pins, as shown in Fig. 3.5(b).

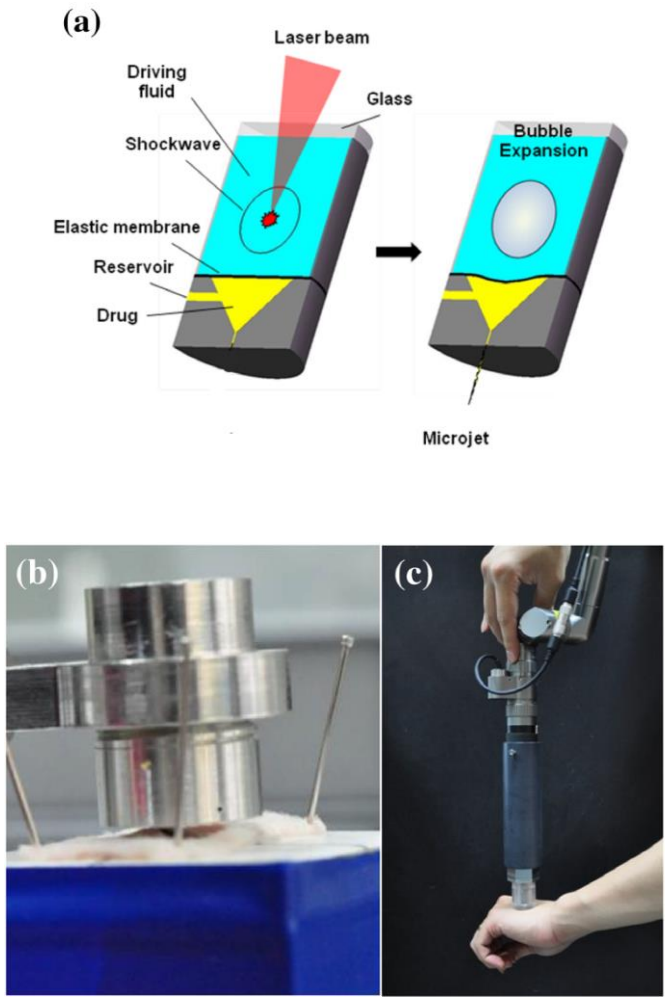

Fig. 3.5. (**a)** Basic mechanism of micro-jet formation based on the elastic membrane response to bubble expansion; (**b)** the abdominal guinea pig skin sample for micro-jet injection; (**c)** handheld injector for projected skin therapy

3.2.3 Results and Discussion

The target toughness was varied to identify the optimal laser energy for penetration. A range of gelation concentration from 3 to 7 % was considered for the test target. 7 % gelatin replicated the toughness of animal skin. Figure 3.6 (a) shows the penetration depth measurements for various levels of target toughness. Laser energy above 1400 mJ per pulse was required to successfully penetrate 7% gelatin, whereas lower laser energy ranging from 400 to 1200 mJ was required to reach 400–1800 μm in depth for softer targets.

The drug viscosity was varied. De-gassed water and hyaluronic acid (HA) filler with viscosity which is 10 times greater than that of water were injected into a gelatin (3 %) target. As shown in Fig. 3.6 (b), even at much higher viscosity, the HA solution of a common anti-wrinkle filler showed only about 20% decrease in the resulting penetration depth.

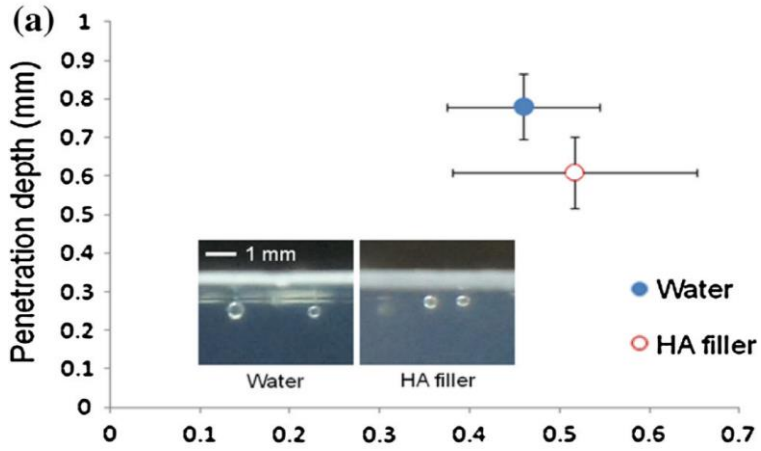

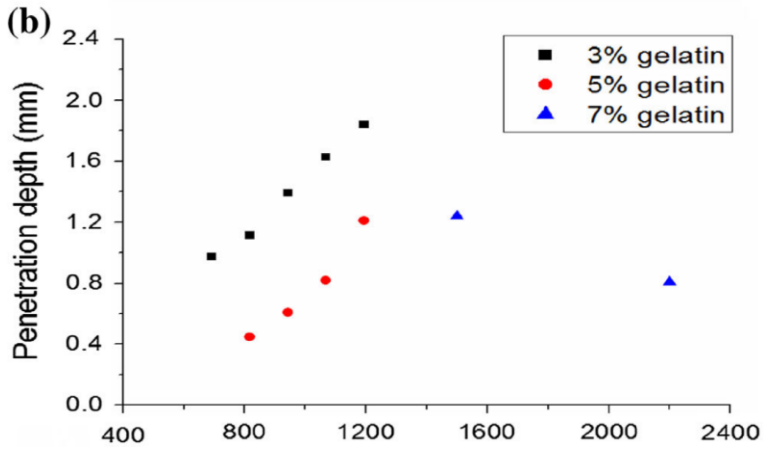

Fig. 3.6. Penetration depth measured: (**a)** different target toughness; (**b)** 1× and 10× drug viscosities

Conventional light microscopy of the guinea pig abdominal skin sample was used to evaluate the drug delivery efficiency. Two types of staining techniques were adapted to verify the transdermal delivery of a liquid drug into a skin sample. A fluorescent microscope was used to analyze the injected fluorescein dye in the epidermis and dermis, and biotin IHC staining was used to confirm the additional content of the biotin protein in the cellular region of the guinea pig dermis.

Figure 3.7 demonstrates IHC micrographs of skin from the guinea pig abdomen, showing the cross-sections of epidermis and dermis. Biotin is a water-soluble B-complex vitamin which is naturally present in uncontrolled skin, as shown in Fig. 3.7 (a). With the addition of biotin delivered by a micro-jet, we expected to see an enhanced level of staining. The epidermis

and thick bundles of collagen are visible in Fig. 3.7 (b) and (c) for the (+) control groups. The existence of biotin in the (−) control result (Fig. 3.7 (a)) suggests the selection of an alternative substance, such as FITC, for further identification of the delivered drug dose in the epidermal layer.

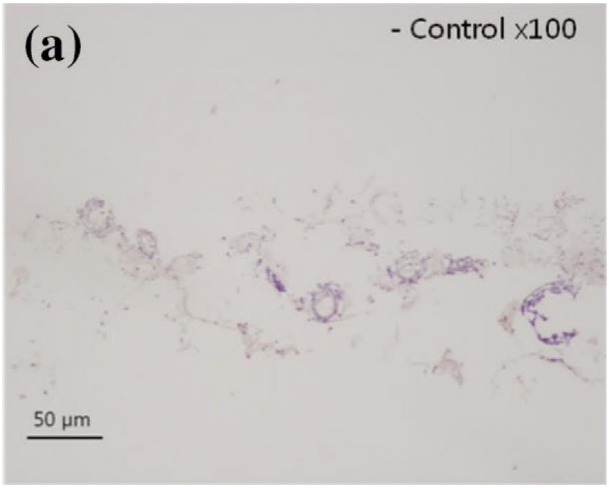

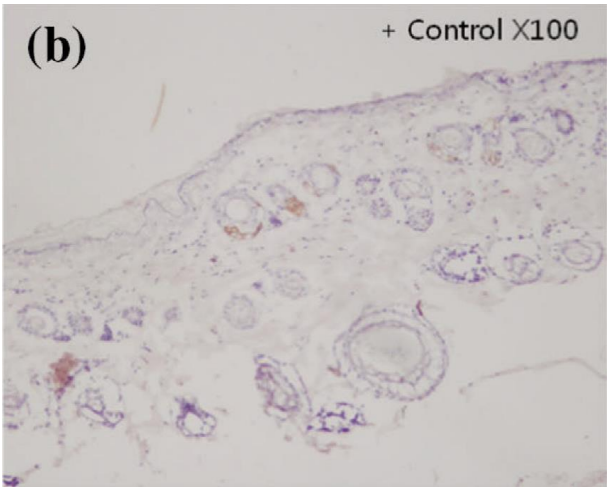

Fig. 3.7. Biotin IHC results showing natural, maximum, and positive staining results for (**a)** no control, (**b)** regular syringe, and (**c)** micro-jet injection

In the laser-assisted micro-jet injection (Fig. 3.8), we noticed well spread sites of FITC in the epidermis and the uniform distribution of fluorescence several tens of microns deeper in the dermal layer. More than 10 pulses of microjets amounted to about 1 μl of FITC solution were applied to achieve uniform distribution of the administered dose in the target region of the guinea pig skin sample. No hot spot of coagulated drug was seen; instead, a smoothly distributed stain of FITC was observed, as in the microscope image shown in Fig. 3.8.

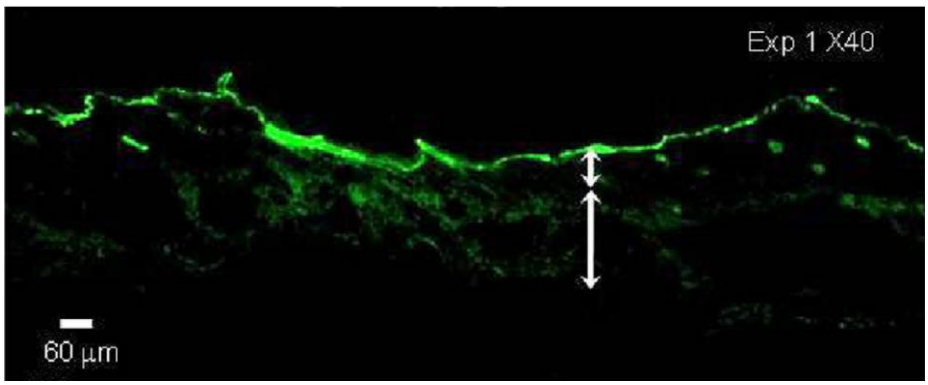

Fig. 3.8. Transdermal FITC staining results: the guinea pig's abdominal skin treated with micro-jet injections. The epidermis extends up to 60 μm, and staining shows the uniform distribution of fluorescence well below the epidermal layer

The vapor formed upon laser focusing in the driving fluid above the rubber membrane has a low density, and the latent heat flow effect is not important. The inertia of the liquid plays the dominant role in the generation of the cavitation bubble; the process of bubble expansion and collapsing due to the pressure gradient across the interface separating the liquid and vapor phase becomes significant. During this isothermal expansion and collapse, the pressure gradient across the bubble interface controls the dynamics of interface motion governed by the following relation [20]:

$$\frac{dR}{dt} = \left(\frac{2}{3} \frac{P_v - P_\infty}{\rho} \right)^{1/2} \tag{3.6}$$

where R is the bubble radius; t is time; P_v and P_∞ are pressures of the inner and outer bubble interface, and ρ is the fluid density. Figure 3.9 shows snapshot images taken under 408 mJ irradiation in water, resulting in a maximum bubble diameter of 3.2 mm at 151 μs.

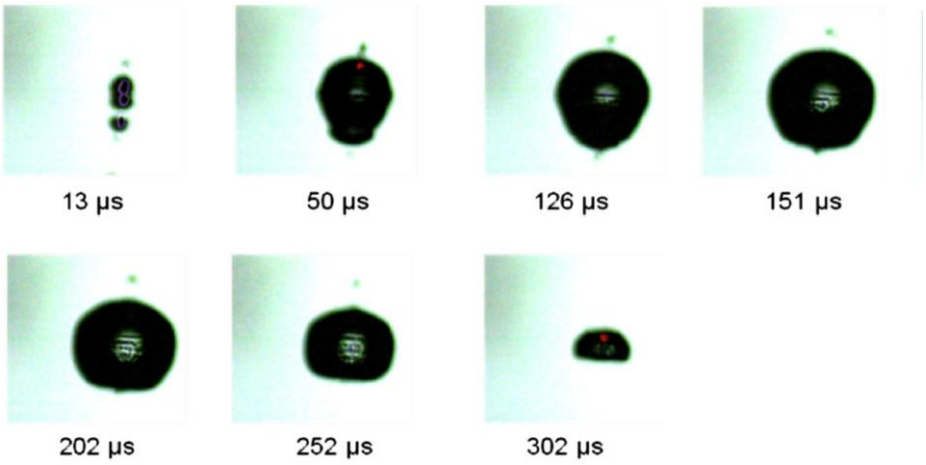

Fig. 3.9. Sequential images of cavitation bubble growth and collapse inside the driving fluid of a micro-jet injector. The maximum bubble size of 3.22 mm is achieved at 151 µs

The images captured during the Nd:YAG laser-induced cavitation bubble expansion inside the chamber indicate the approximate time duration in which the microjet was ejected. After a focused laser pulse was delivered, 7 ns later bubble expansion starts from the optical breakdown point. Vapor and non-condensable gas reduce the rate of heat transfer between the hot breakdown point and cold liquid. As the bubble expands, the increased chamber pressure exerts tensile loading on the chamber and ultimately the elastic membrane that effectively ejects the drug into the reservoir below, out from the micro-nozzle at several hundred meters per second.

The cavitation bubble formation (shock generation) and expansion result in the ejection of a high-speed micro-jet out of the nozzle as visualized in Fig. 3.10. Increasing the micro-jet breakup length helps to delay atomization,

causing a clean jet head impact on the target surface and allowing deeper and more efficient delivery of the drug to the targeted depth beneath the skin surface. In all the animal tests, we allowed less than 2 mm standoff distance between the target and the injector, and therefore the resulting micro-jets were expected to be stable and free from atomization, ensuring good penetration efficiency.

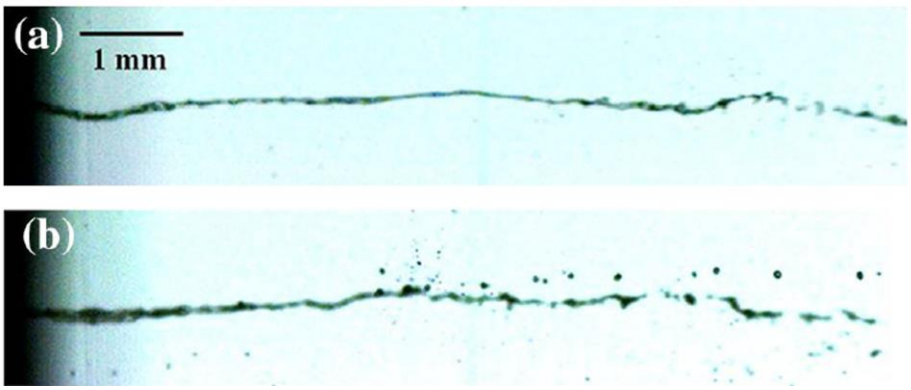

Fig. 3.10. (**a)** The first jet due to a shock wave shown with a breakup length of 5.47 mm, (**b)** the second jet resulting from the bubble expansion shown with a breakup length of 3.53 mm

Furthermore, the characteristics of the observed microjet driven by the Nd:YAG laser system were analyzed. The calculated Reynolds and Weber numbers based on the nozzle diameter (Table 3.1) suggest that the present micro-jet is a fully developed turbulent jet. The gaseous Weber number of both the first and second microjets is well above the critical Weber number of 0.4 [21], suggesting that the breakup length is inversely proportional to the jet

velocity. The key to stable penetration of a micro-jet into a tissue is the breakup length 'long enough' to delay any disintegration of the liquid jet body into droplets, as clearly is the case in our animal tests.

Table 3.1. Calculated Reynolds and gaseous Weber numbers for the Nd:YAG-driven micro-jet

	Re	We_g
1st jet due to shock wave	11,078	13.5
2nd jet due to bubble growth	7081	7.8

3.3 Penetration Using Er:YAG Laser-generated Microjet

3.3.1 Background and Motivation

The laser-based microjet injection system uses the hydrodynamic impact of a narrow liquid jet onto skin. The immediate delivery would enable minimized prescription of topical drugs intended to work on the outer layers of the skin, avoiding any skin irritation or allergic reaction and preventing uncontrolled evaporation of active ingredient and unpleasant odor associated with noninvasive procedures. Several types of injection mechanism have been considered, including spring compression, expansion of piezoelectric transducer, linear Lorentz force driven piston actuator, and expansion of laser-initiated waves in water [6, 22, 23]. Such mechanisms would eliminate

abundant needle wastes, and they are favored for highly needle-phobic patients [3].

A narrow, high pressure jet of 100 to 200 m/s velocity is required to accelerate the drug to penetrate the animal skin with 20 MPa of yield strength [3]. Reducing the jet diameter to a 100 μm size has shown the advantage in drug delivery of minimizing damage to the tissue [22]. The present scheme of injection via Er:YAG laser beam at 250 μs pulse duration generates pressure by the displacement of liquid via laser-induced vapor bubbles and the elastic pumping of the drug through a nozzle by a membrane separating the driving liquid from the drug.

Success in jet injection requires sufficient impulse of the jet to penetrate the target tissue. In the case of an Nd:YAG laser at 7 ns pulse duration, high irradiance of a Q-switched beam produced instantaneous expansion of bubbles and generated multiple shockwaves [6]. The consequent jets due to both shock and bubble expansion reached up to 230 m/s while the short length of the jet is insufficient for ensuring a sizable dose of drug targeting a treatment site.

Here we adopted a quasi-long pulsed Er:YAG beam at 250 μs to power source of injector. The high absorbance of the beam to water (2940 nm) also enables a stronger generation of a jet at lower laser energies. We present the enhanced controllability and dosage of delivered drug into a guinea pig's skin through fluorescent staining on both postmortem abdominal and living dorsal skins. Furthermore, to verify test results, the Plesset equation of the vapor bubble theory has been adopted to confirm the measured jet velocity resulting

from the laser-initiated microjet.

3.3.2 Experimental Approach

When the low irradiance laser energy reaches the driving liquid in the upper chamber of the injector [6], the temperature rise in a focal point in water admits a sudden vaporization and generation of a vapor bubble [20]. The process of constant pressure phase transformation is marked by a superheated liquid formation of vapor voids. The Er:YAG laser has 250 μs pulse duration and wavelength of 2940nmat which water best absorbs the beamed energy. Once vapor is accumulated in the bubble, any additional radiation passes through the expanding bubble without being directly absorbed by the vapor. Elongation of the bubble discontinues as the initiation of the bubble stabilizes beyond 250 μs and reaches a maximum radius.

We adopt explosive bubble expansion induced by a laser irradiation as an actuator for ejecting a coherent microjet. The present injector consists of a micro nozzle for storing liquid drug, a chamber for driving fluid separated by a heat resistant flexible membrane between drug and water, and air-tight confinement glass at the beam incident and with O-ring type sealing. A highly water absorbant Er:YAG beam irradiates the water for vapor bubble generation within the driving liquid chamber. Ideally sealed in the chamber, growth of the bubble would cause a sizable pressure impulse on the elastic membrane. The elastic response of the membrane ejects liquid drug out from

a 150 μm nozzle at a velocity needed to penetrate skin.

In Fig. 3.11(a), the ejected jet shown in an air background reaches up to 30 m/s, which has larger injection volume than the speed previously attainable by a nanosecond pulsed Nd:YAG laser system [6]. The laser system offers various jet properties with a change in laser energy. The flow through a narrow nozzle experiences turbulent and frictional losses. Figure 3.11(b) indicates that friction at the nozzle exit causes velocity reduction in the region below 800 mJ and the turbulence shortens the jet length in the region beyond 800 mJ [24]. The instability causes spray and a decrease in energy of the jets, a process known as atomization. In all injections of the present scheme, the stand off distance between the nozzle and the skin is less than 3 mm to avoid any instability due to these jet properties.

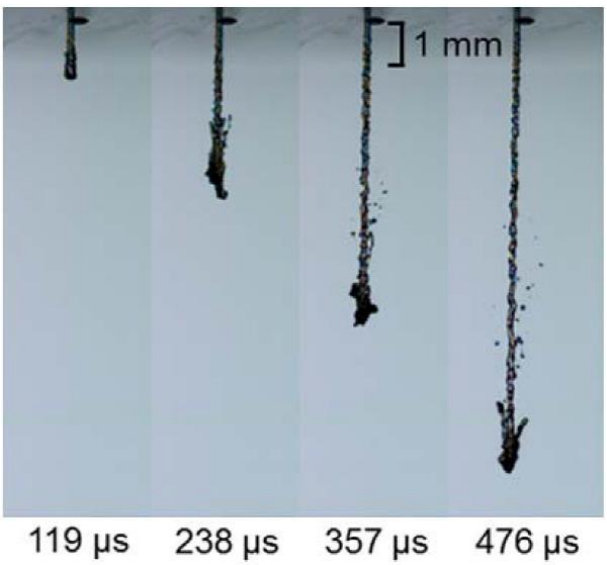

(a)

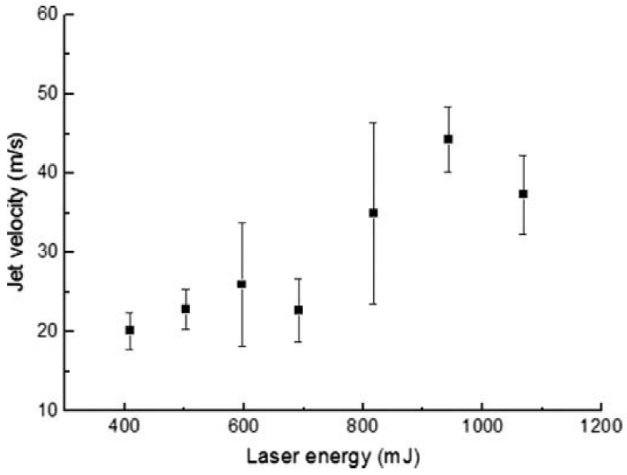

(b)

Fig. 3.11. Ejected microjet in air, (a) Images of Er:YAG microjet at 408 mJ, 250 μs pulse duration showing jet velocity of ~ 30 m⁄s, (b) Jet velocity shown for varying laser energy $E = 0.5\rho(\pi r^2)u_{jet}t$.

The injection liquid was prepared by dissolving fluorescein isothiocyanate (FITC, 0.05 mg ⁄ml) in dimethyl sulfoxide (DMSO) solution for verifying microjet penetration performance. The treated skin from the FITC test was analyzed by a fluorescence microscope (Nikon Eclipse Ti-U), and hematoxylin and eosin (H&E) staining was used to monitor alteration of tissue after injection.

The stained skin samples were frozen and chopped by cryotome (Leica). Three pieces of a sample were made with the injection point being the center. Each cross section was vertical to the injected area and made into a slide to

analyze with a microscope. The embedded sites of fluorescent trace observed with the microscope would confirm drug penetration and the range of spread underneath the outer skin layer.

A male Hartley guinea pig was laid on a table to perform jet injection on the back for a dorsal skin test. In the abdominal case, the relevant skin was first sectioned into a 15 × 15 mm target and cleaned to remove fat and subdermal tissues. The prepared skin sample was affixed on a foam board with pins. The laser irradiated the driving fluid, and the jet was ejected from the nozzle vertically to a target material. The guinea pig used was 250 grams of weight. The skin was epilated with wax for 24 h before the experiment and immediately used without freezing.

For the skin mockup for instant visualization of penetration, a gelatin gel was used, which offers controllable mechanical properties depending on its weight percent. Gelatin of 60 Bloom was dissolved in water at 5 percent. The Bloom number indicates the toughness of gels, and 60 meets the typical animal skin toughness.

3.3.3 Results and Discussion

Figure 3.12 is the staining result on a sectioned sample of guinea pig abdominal skin. The fluorescence is dispersed in all directions around an impact point. The microjet initiated with a 1.19 J laser beam delivers the drug over the epidermis and dermis within 280 μm from the skin (Fig. 3.13).

Figure 3.13 shows the results of microjet injection on dorsal skin as administered on a living guinea pig laid on a table. The drug is evenly dispersed on the skin tissue similar to the abdominal case. The dorsal skin is thicker (500 μm) than the abdominal skin such that deeper wetting of the relevant layers is effectively treated with FITC.

The H&E staining shown in the upper-right windows after microjet injection displays the architecture of the treated sites, and it shows that the drug is delivered with no alteration of skin morphology adjacent to the injection site. The microjet initiated with a 1.57 J laser beam, however, achieves a targeted local delivery rather than dispersion [Fig. 3.13(b)]. Unlike the abdominal case of a sectioned sample affixed to an acrylic plate, the underlying structure of dorsal skin supports jet propagation, allowing a deeper penetration. Even though the injection spot had been ruined following the path of a jet, these microstructural changes are expected to be recovered by the barrier recovery process [25].

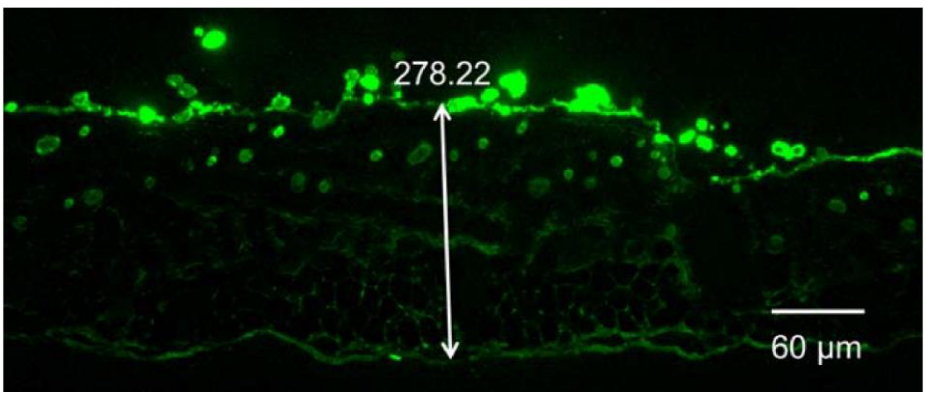

Fig. 3.12. FITC staining of guinea pig abdominal skin treated with

1.19 J/pulse.

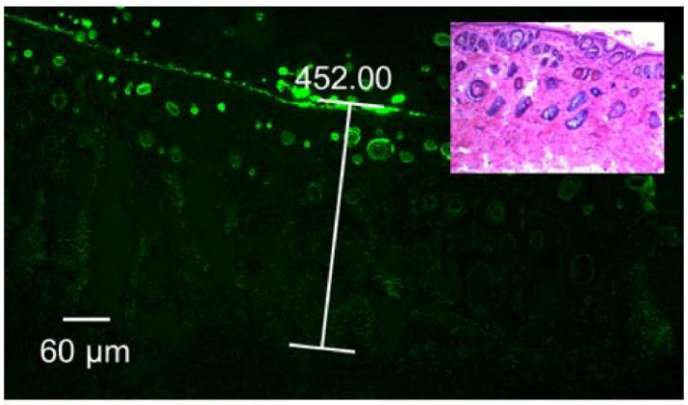

(a)

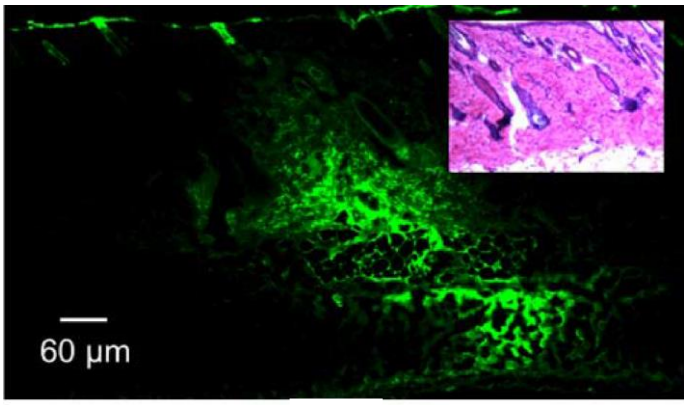

(b)

Fig. 3.13. FITC staining of guinea pig dorsal skin treated with (a) 1.19 J/pulse and (b) 1.57 J/pulse

The jet produced with 1.19 J of laser pulse showed smaller volume than the case of 1.57 J. The jet energy is mostly dissipated at the upper layer of skin. However, increased jet energy reaches deeper layers of skin with higher energy. The jet energy is converted to deformation of the skin barrier or

propagation of the stress wave depending on the skin properties. The jet achieves farther delivery of drugs when more energy is converted to deformation energy than to stress wave.

Gel models are used for visualization and mimicking of the skin elasticity to evaluate jet injection. Jet injection consists of three events: jet impingement, absorbed into the skin, and dispersion under skin [Fig. 3.14(a)]. Jet impact creates a hole on the gel with an estimated impact pressure or water hammer pressure from Eq. (3.7), where the impact pressure depends on the sound velocity a as well as the jet velocity u_{jet}. Then at a lower jet pressure proportional to the square of the velocity, the ejected dose is delivered into the gel making a path of jet stream. A thin cylindrical jet of 150 μm generated from an injector causes virtually zero splash-back at the contact surface as seen in Fig. 3.14(a), allowing smooth penetration. In gel models, the dense structure with no porosity forces the jet to agglomerate and causes bounce of the drug in the gel:

$$P = \rho_0 u_{jet} a \tag{3.7}$$

This is the pressure needed to overcome the ultimate strength of a target for the surface erosion. For a typical skin strength of 20 MPa, Eq. (3.7) suggests a minimum jet velocity of 13 m⁄s for water density 1000 kg/m3 and sound speed of 1500 m/s in water.

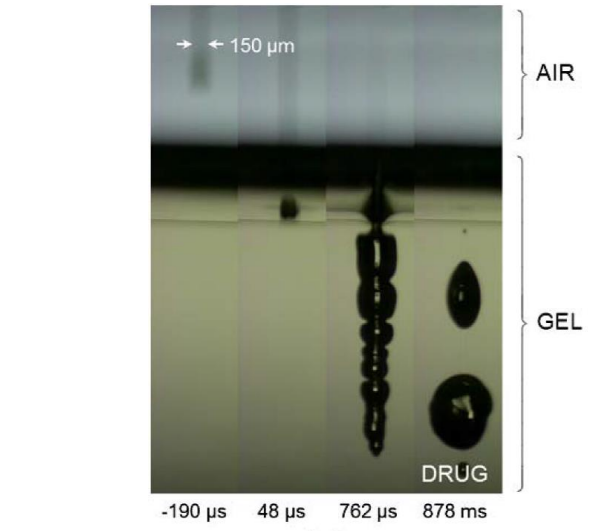

(a)

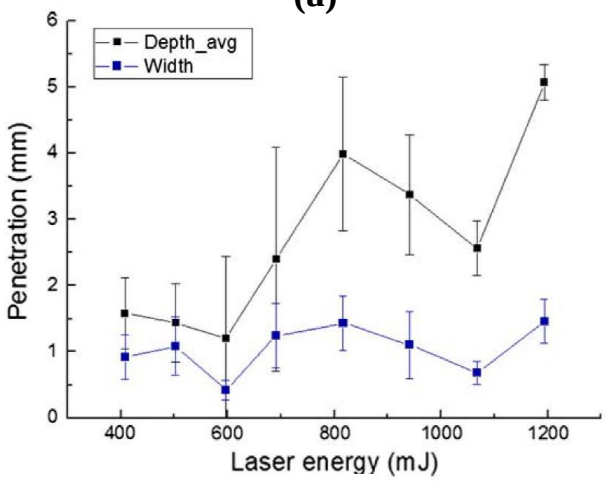

(b)

Fig. 3.14. (a) Microjet injection shown with no splash-back, 150 µm diameter, and gel penetration of drug at 408 mJ. (b) penetration depth and width for varied laser energy.

The penetrated depth and injected volume are evaluated with varying laser energy on a gel model [Fig. 3.14(b)]. The penetrated depth increases as the

laser energy is intensified up to 800 mJ. At 600 mJ, the injection efficiency is reduced due to the recovery response of the gel. Above 800 mJ, increased jet velocity shortens the jet length according to the jet breakup. The spray characteristic and instability of the weakening jet beyond a high critical Weber number may be responsible for this observation.

The jet velocity may be analytically determined. We consider a 408 mJ (low-energy) case for illustration purposes. We used the empirical data for temporal development of the bubble radius and the Rayleigh–Plesset approximation [12] to estimate the pressure and temperature gradients on the driving liquid wall for jet ejection. For vapor bubbles, the thermal effects play a dominant role and the effect of liquid inertia can be neglected. The Plesset model considers the evaporation and the heat conduction. The temporal evolution of bubble radius *R* can be approximated by the following equation [20].

$$R = R^* t^{1/2} \tag{3.8}$$

where R^* is defined as

$$R^* = 2\left(\frac{3}{D\pi}\right)^{\frac{1}{2}} \frac{k_l}{L\rho_v(T_b)}(T_w - T_b) \tag{3.9}$$

Here L is the latent heat, $\rho_v(T_b)$ is the equilibrium vapor density corresponding to the boiling temperature T_b, T_w is the temperature on the bubble wall, and *D* and k_1 are the water thermal diffusivity and conductivity,

respectively.

Solid circles in Fig. 3.15(a) illustrate the empirical $R(t)$ Our empirical data obtained from the images of Fig. 3.15(b) implies that $R^* = 0.125\text{m/s}^{1/2}$. The dependence of Eq. (3.8) for this value of R^* is illustrated with the solid curve. A good agreement between asymptotical behavior and the empirical data is observed. Equations (3.7) and (3.8) suggest that the "superheat" $T_w - T_b$ should be nearly constant, and by substituting values of the dimensionless radius, D, ρ_v, T_b and k_1 for water, we estimate $T_w \approx 14/°\text{C}$.

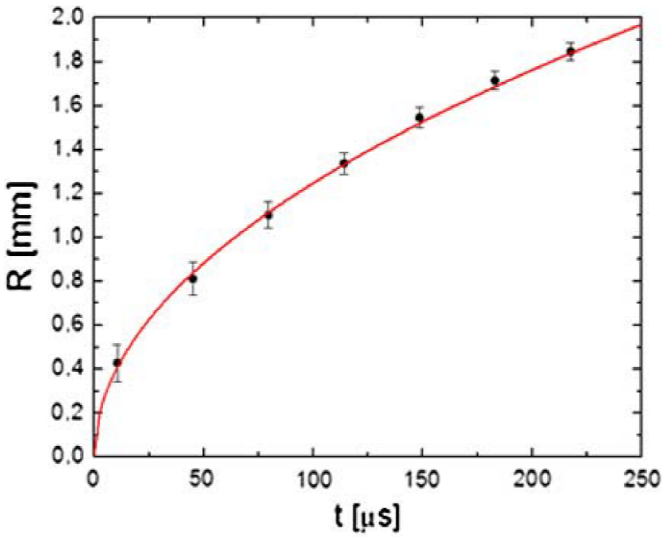

(a)

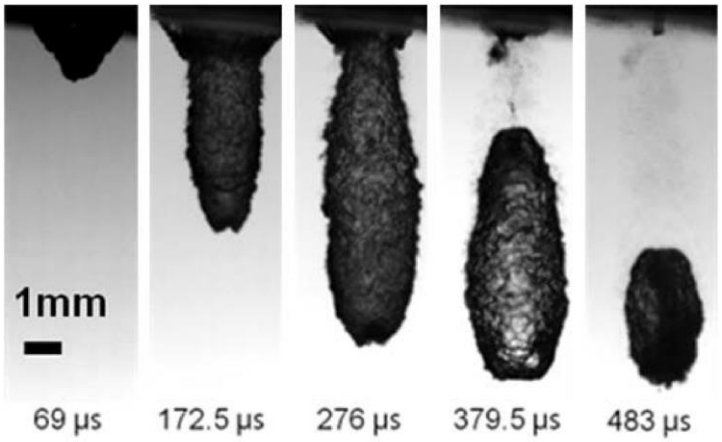

(b)

Fig. 3.15. (a) Laser-induced vapor bubble: (a) radius of expanding bubble wall (data: symbol; theory: curve) and (b) images of 408 mJ beam-initiated bubbles in water.

Equation (3.9) can be rewritten in terms of the pressure difference [6],

$$R^* \approx 10^{-6}(P_w - P_\infty) \tag{3.10}$$

where P_w is the pressure exerted on the bubble wall by vapor, P_∞ is the liquid pressure far from the bubble wall, and the constant 10^{-6} m/s$^{3/2}$ corresponds to the water heated to 100 °C. Substituting our value of R^* in Eq. (3.10), we estimate $P_w - P_\infty \approx 125$ kPa and thus $P_w \approx 225$ kPa.

Suppose that the chamber is closed and the volume of the liquid is comparable with the actual volume of the bubble in the driving chamber of

the injector. Then P_∞ in Eq. (3.10) should decrease, taking into account the compression of the liquid inside of the chamber. This is done by the Tait equation of state,

$$P_\infty = (B + P_0)\left(1 - \frac{V}{V_c}\right)^{-7} - B \tag{3.11}$$

where B = 314 MPa, P_0 = 100 kPa, the actual chamber volume V_C = 352 × 10^{-9} m^3, and the volume of the bubble V = $4/3\pi R^3$.

From Eq. (3.11), the pressure on the chamber wall increases with the radius of the bubble. The bubble grows until the pressure in the liquid compensates the pressure on the bubble wall. Assuming that the bubble has the same initial value of $P_W \approx 225$ kPa, the maximum pressure on the chamber wall should be reasonably close to P_w. The rise of the pressure inside of the chamber pushes the liquid out of the chamber. The resulting jet velocity U_J can be estimated with the help of the Bernoulli equation,

$$U_J = \sqrt{\frac{2\Delta P}{\rho_0}} \tag{3.12}$$

Where ΔP is approximately 225 kPa at the exit nozzle. For the given chamber and laser parameters, the jet velocity (without the elastic membrane) is $U_J \approx$ 21.2m/s, which is close to the experimentally obtained jet speed at 408 mJ

/pulse of Fig. 3.12(b).

3.4 Pulsed and Repetitive Microjet Generation

3.4.1 Background and Motivation

There have been calls for a new drug delivery system to overcome common issues such as needle phobia and contamination from reuse of needles [1-3]. One possible remedy is a system based on the microjet [4-6, 23, 26, 27] whereby the generation of needle-free injection relies on the bubble dynamics within the injector [8, 9]. Both jet characteristics and bubble behavior determined by the laser beam properties such as wavelength and pulse duration have been studied [27]. For general use of a laser induced microjet injector as a clinical device, the delivery of drug into the human tissue must be assured by a zero side effect associated with any type of drug damage done by strong thermal and inertial effects of the laser ablation based mechanism for ejecting a microjet [5].

In order to address these potential concerns addressed by the medical practitioners, the injector design is evolved around the use of two separate chambers that independently contain driving water (in the upper chamber) and drug (in the lower reservoir), separated by a thermally resistant silicon rubber membrane. The laser ablation occurs within the upper driving chamber only, while the drug solution beneath the membrane is protected from the laser ablation. The strong bubble generation in the driving chamber

gives rise to an elastic deformation of the membrane which then causes an instantaneous ejection of the drug solution from a drug reservoir through a narrow micro nozzle.

The MRTD (Maximum Recommended Therapeutic Dose) from the FDA ranges from 0.00001(Epoprostenol) to 1000 (Glycerol) mg/kg-bw/day [28]. These optimal amounts imply that the dose controllability is critical for a practical drug delivery system. Two ways to optimize dose controllability are a direct control of each ejected volume, and a control of the number of repetition with a fixed injection volume. Our system is geared toward the second way, in order to avoid pain or bruising due to an excessive amount of drug being transferred to the sensitive skin layer [3, 29, 30].

In this paper, we provide how the injection volume responds to the system parameters in order to achieve a practical dose (1 cc) of drug delivery possible for a general clinical use of the present system. Then a description of the repetitive microjet generation using a step motor that provides a continuous refill of the targeted dose to the injector is provided. In addition, any potential thermal issues associated with the laser ablation based drug delivery is analyzed via chemical analysis. Any damage done to drugs is estimated by monitoring the increase-rate in the amount of Laminin and Elastin from each corresponding growth factor (EGF) and hormones (HGH) injected. The level of EGF and HGH is shown to remain unchanged before and after the multiple injections, indicating that potential drug damage can be neglected in the present drug delivery system.

3.4.2 Experimental Approach

Microjet is generated by expansion of the vapor bubbles induced by the focused laser beam as illustrated by Fig. 3.16(a) [27]. The jet characteristics are obtained from the high speed camera images taken at 42,001 fps (Fig. 3.16(b)). Er:YAG laser is used to generate vapor bubbles, and the wavelength and pulse duration of the beam are 2940nm and 250μs, respectively. The laser is operated at 10 Hz with 408 mJ energy in all tested cases.

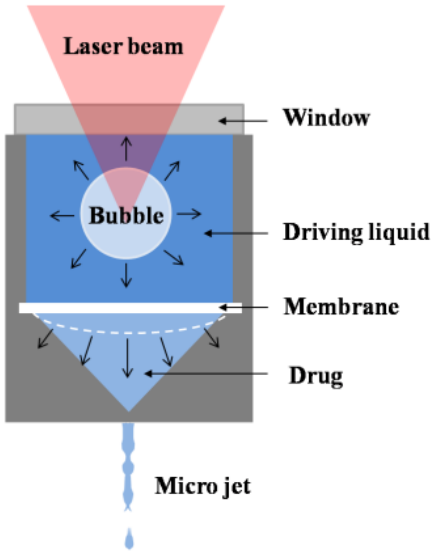

(a)

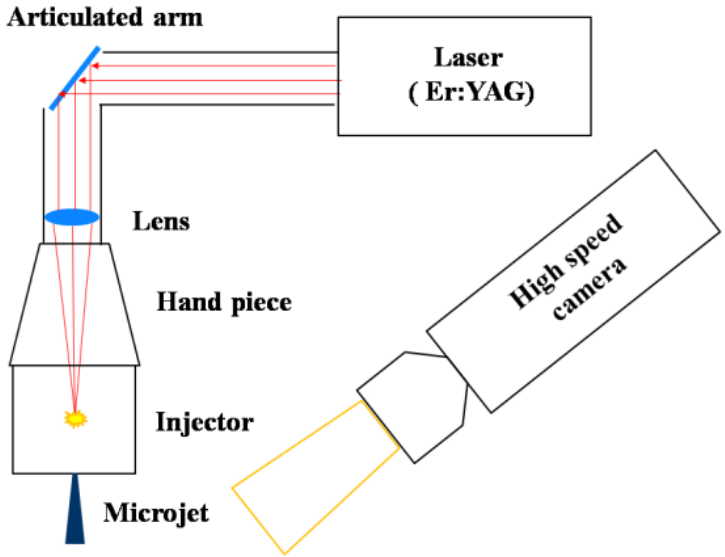

(b)

Fig. 3.16. (a) Mechanism of microjet generation, (b) a schematic of experiment

The experimental objectives are twofold: one is an enhancement of the jet volume with a multiple jet generation capability, and the other is a safety assurance of the drug being injected by a laser ablation means. The parametric study is carried out to establish a relationship between the jet characteristics and the injector parameters. The injector is a pressurized device whose performance depends on its driving chamber height. The jet generation is directly related to the geometry of a drug reservoir as shown in Fig. 3.17 (a). The jet volume and velocity are affected by reservoir diameter, reservoir angle, and cylinder height. The experiment conditions are tabulated in Table 3.2.

For repetitive jet generation, a linear stepping motor (model name: 25BYZ-B04) is used to provide a continuous refill of the drug reservoir. Fig. 3.17(b) is a schematic of the drug refill system that consists of 6 components: control box, articulated laser arm, stepping motor, hand piece, syringe, and injector. Approximately 1 cc dose of drug is contained in a syringe which is then fed to the drug reservoir. The laser beam is focused into a water chamber through a convex lens positioned inside the articulated arm, and injector is connected through a hand piece. After the jet ejection, the step motor refills the drug by controlling the pulse signal as shown in Fig. 3.17(c).

Channel 1 shows the trigger signal of the laser, and Channel 2 shows the control signal of the stepping motor as shown in Fig. 3.17(c). Motor moves 5.2 μm forward and amount of the transferred drug is 0.46 μL by a single signal pulse of stepping motor. The number of signal pulse can be adjusted by a controller to achieve a desired amount of the drug refill. These two signals are synchronized for a repetitive refill process. A control box has the PCB panel which controls the signal of a step motor to a specified amount of drug being refilled.

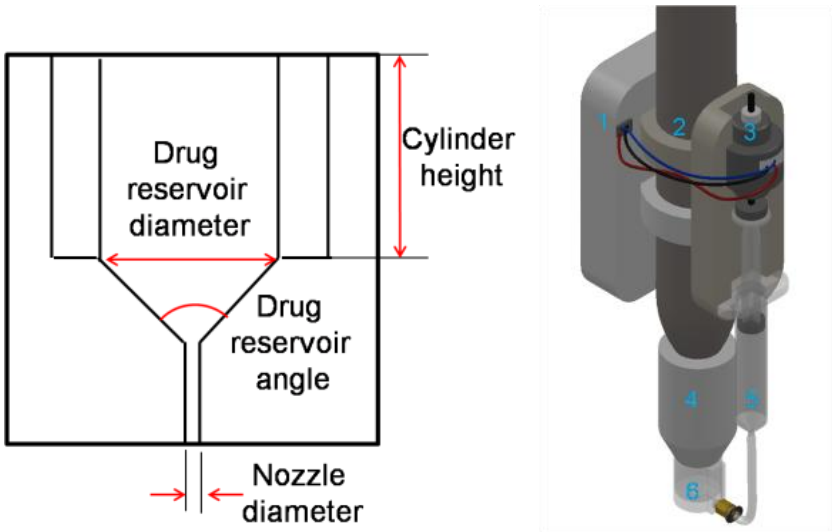

(a) **(b)**

(c)

Fig. 3.17. (a) 2D schematic of injector, (b) 3D schematic of drug refill system, and (c) typical signal of laser and motor

Table 3.2. Parameters of the microjet injector

Injector parameter	Value
Drug reservoir diameter	4, 7, 11 mm
Drug reservoir angle	30, 60, 90, 120, 150°
Cylinder height	3, 5mm
Confinement	Sapphire window

EGF and HGH which are the hormones used to assess any thermal damage done to the drug being injected. The molecular weights of EGF and HGH are 6kD and 22kD, respectively. Keratinocyte and Fibroblast are cultured in plate, and these hormones are then diluted in each cell. After 24 hours, RNA is extracted to investigate the gene expression for each cell (Real time PCR). The level of gene expression for Laminin in Keratinocyte and that of Elastin in Fibroblast per concentration is analyzed, and activity of growth factor and hormone are checked after and before each injection.

3.4.3 Results and Discussion

Ten experiments are conducted to investigate the effect of injector parameters on the jet characteristics. The experimental results are summarized in Table 3.3. Comparing Cases 2, 6 and 10, an optimal diameter of the drug reservoir is determined to be 7 mm. The effect of diameter is related to the bubble behavior. The microjet is generated by deformation of the membrane, which is strongly related to the size of the bubble. The area

under pressure is determined by the cross sectional area of the bubble. If the cross section of a drug reservoir is smaller than the area under pressure, there must be a pressure loss and the ejected volume of the jet may become smaller. In the opposite case, pressure is not enough to expand the membrane and thus volume of jet being ejected may be decreased. These relations imply that an optimal value of a reservoir diameter exists, which is determined to be about 7 mm in the present experiment.

Comparing the following cases of each group, one can understand the effect of the cylinder height on the resulting microjet: Group 1 (Case 1, Case 2), Group 2 (Case 5, Case 6), and Group 3 (Case 9, Case 10). In each group, enhanced jet volume is achieved by smaller cylinder height as shown in Fig. 3.18(a). The pressure inside the smaller driving chamber is higher than that of a larger volume when microjet is ejected. The size of a generated bubble is the same for all cases because of the same laser energy (408 mJ) used, but a higher chamber pressure was resulted in a smaller chamber volume.

The effect of the drug reservoir angle on the jet characteristics is shown from Case 3, Case 4, Case 5, Case 7, and Case 8. How the drug reservoir angle affects the jet can be found from Fig. 3.18(b), as an optimal value of the angle can estimated to exist between 60 and 90 degrees. The angle is proportional to a distance between the membrane and nozzle with a fixed diameter of the drug reservoir. The membrane cannot stretch up to a maximum length when a distance is too short. Thus a maximum volume of the ejected jet can be obtained at a specified distance according to an optimal angle.

Table 3.3. Experiment results for enhancement of the ejected jet volume

Case	Drug reservoir diameter	Drug reservoir angle (deg)	Drug Reservoir Volume (μL)	Cylinder Height (mm)	Nozzle diameter (μm)	Jet Velocity (m/s)	Jet Volume (nL)
1	4	90	14.7	3	150	43.9±1.7	640±50
2	4	90	14.7	5	150	44.6±1.8	468±30
3	7	30	167.6	5	150	23.1±1.0	452±37
4	7	60	77.8	5	150	33.7±2.6	832±19
5	7	90	44.9	3	150	50.6±1.6	2100±28
6	7	90	44.9	5	150	50.2±1.5	1738±12
7	7	120	25.9	5	150	29.1±3.0	584±11
8	7	150	12	5	150	23.0±4.0	358±14
9	11	90	110.9	3	150	33.8±1.9	1073±16
10	11	90	110.9	5	150	29.5±1.8	738±12

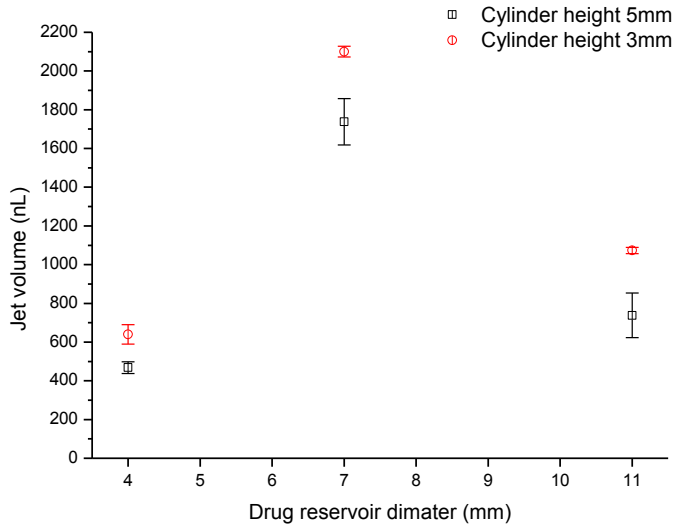

(a)

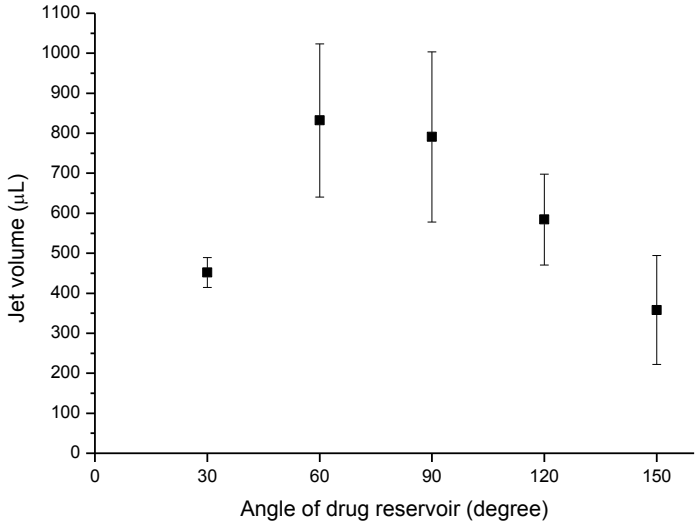

(b)

Fig. 3.18. Resultant jet volume due to (a) drug reservoir diameter and cylinder height, (b) angle of drug reservoir

Fig. 3.19 corresponds to the repetitive microjet generation without a refill pump. Atomization starts from a third ejection while the jet volume is decreased as the number of injections increased. These phenomena are the result of air inflow through the nozzle. Microjet is generated by deformation of the membrane as the membrane restores its initial position due to elastic force. During this process, pressure inside of reservoir is lower allowing air to enter from outside. Consequently a membrane squeezes out both drug and air bubbles. When air bubbles form within a jet, rapid atomization occurs as the ejecting jet is very unstable.

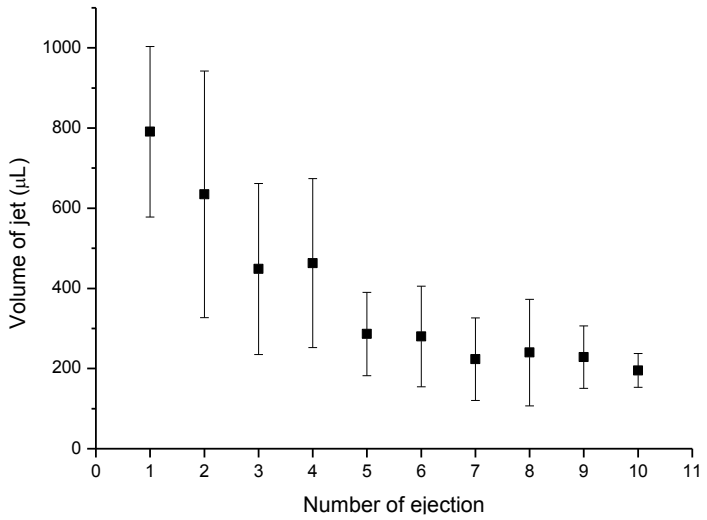

(a)

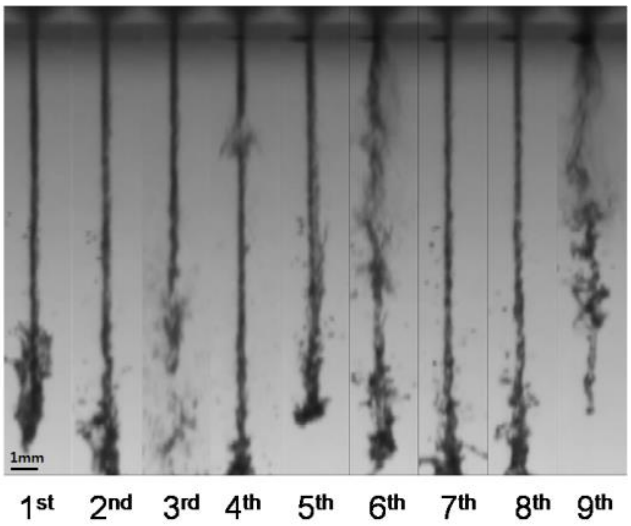

(b)

Fig. 3.19. Repetitive microjet jets without the refill pump: (a) jet volume and (b) images of repetitive microjet

For repetitive jet generation, air inflow is minimized in order to reduce level of atomization. One controls the flow rate of drug using a motor-driven pump. A motor moves 41.7 μm in each step, and one step angle is controlled by 8 clock signal. As a result, a motor moves 5.2 μm forward for each pulse signal. Fig. 3.20 shows a trigger signal of the laser (ch1) and a signal of the motor (ch2). There exist two critical flow rates that define the three distinct regions of the jet. If the flow rate at which drug chamber is being refilled by the motor is greater than the rate of ejection of microjet, it defines the first critical flow rate. This is where the nozzle tip droplet gradually grows. If the flow rate is further increased, the droplet is detached with an increased

ejection of the jet volume. This is denoted the second critical flow rate.

Below figure 3.20 shows motor signal of each critical flow rate and each number of pulse is three and fifteen respectively in one cycle. Laser is operated at 10Hz, which means that signal has 10 cycles in one second. In first critical flow rate, the motor moves 15.6 μm forward during 0.1 second, pushing in the syringe plunger of 10.6 mm in diameter. Thus a total volume of a refilled liquid is 1.38μL in each cycle. An averaged ejected jet volume is 832 nL and this value is smaller than first critical flow rate. If flow rate is increased then jet characteristic is changed by reaching second critical flow rate. At this point, the motor moves 78 μm and the volume of the transferred liquid is 6.88 μL per cycle.

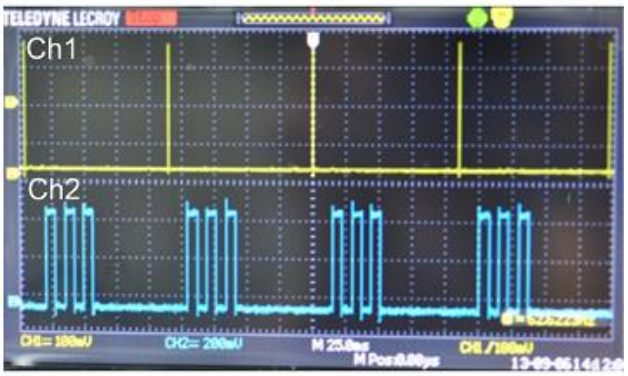

(a)

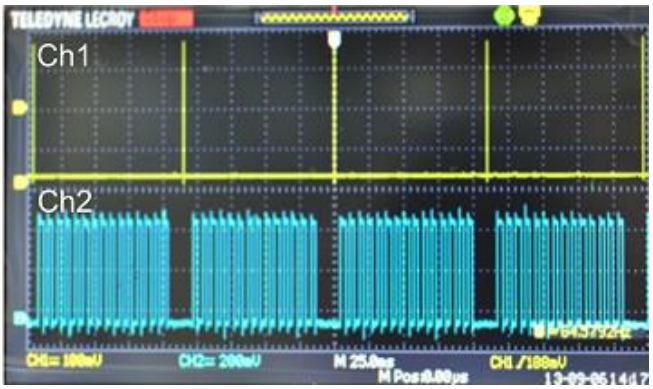

(b)

Fig. 3.20. Motor signals for (a) first critical flow rate (13.8 μL/s) and (b) second critical flow rate (68.8 μL/s)

The jet characteristics can be casted into three distinct cases. Case I is where the flow rate is less than the first critical flow rate. Case II is where the flow rate is between the first and the second critical flow rates. Case III is where the flow rate is greater than the second flow rate. In Case I, the flow rate is relatively low thus the air inflow is still allowed. Small sized droplets occur at the nozzle tip which is shown by the line (denoted 1) in Fig. 3.21. In this case, droplet size remains the same while jet breaks up into smaller droplets. In Case II, the shape of a jet head is more stable than the first case as shown in fig. 3.21(a) and (b), because the rate of air inflow is slowed down by the increment of the mass flow. But the bigger sized droplets are located at the nozzle tip and the size increases by the greater flow rate. When the surface tension between droplet and nozzle tip no longer sustain the weight of droplet, droplet is detached from the injector. Jet passes through the droplet, which makes jet diameter thicker as shown in Fig. 3.21(b). For

Case III, droplet at the nozzle tip is minimized such that inertia of an ejecting jet is greater than surface tension between nozzle tip and droplet. Therefore ejected jet is not easily disturbed by the presence of the droplet, which makes a narrower microjet.

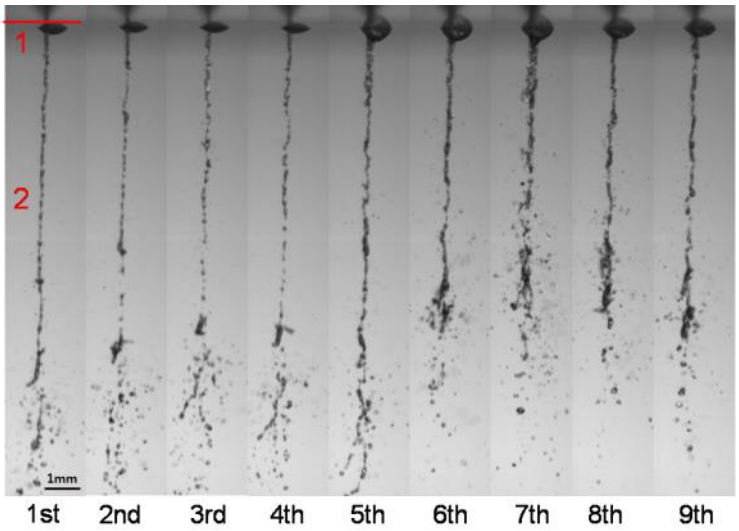

(a) Low flow rate

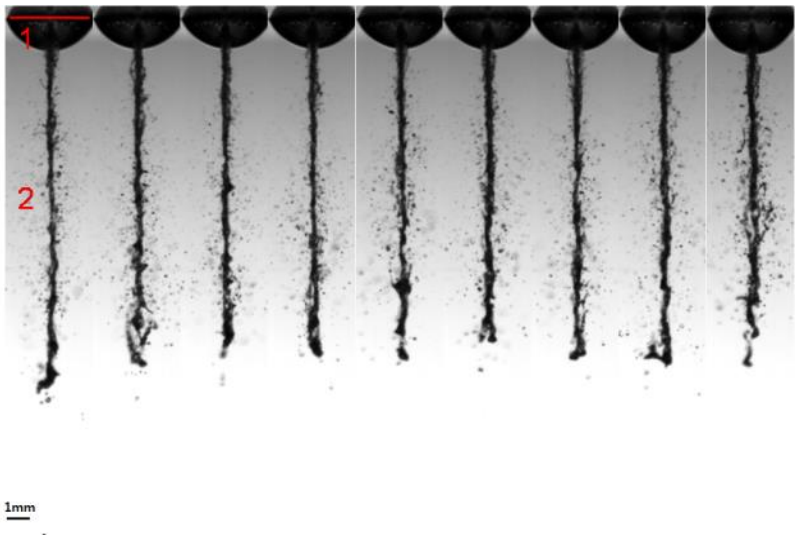

(b) Intermediate flow rate

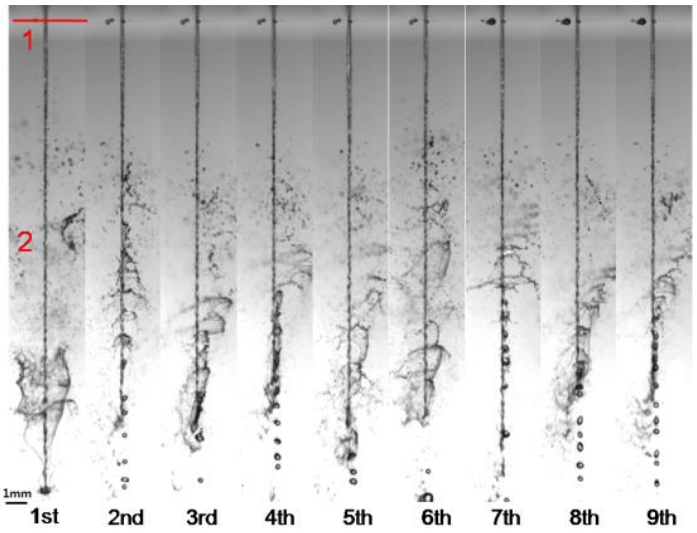

(c) High flow rate

Fig. 3.21. Images of ejected jet according to the flow rates (a) Case I, (b) Case II, and (c) Case III

Fig. 3.22 shows three cases of the repetitive microjets with respect to each flow rate. The jet volume in Case I is similar to that of Case III while a relatively smaller volume of jet is observed in Case II because droplet formed at the nozzle tip affects jet characteristics in an adverse way as described earlier. The delivered amount of jet on average is from 962 nL to 1415 nL per pulse. If the ejection is continuous for about 15 minutes, and the laser is operated at 10 Hz, then total ejection volume would reach 865.8 μL to 1.273.5 mL. This means that the injector can deliver a targeted dose of 1 cc which would fulfill most of the clinical requirement for the various drugs.

Droplet causes deceleration of a jet as follows: viscous force causes jet deceleration if jet is inside the droplet. Then the jet bursts out through the droplet, and the jet velocity is decreased. These effects play a key role when the droplet reaches a certain size. The level of deceleration of a jet is determined by the size of a droplet. As a result, jet velocity is fastest in the order of Case III > Case I > Case II.

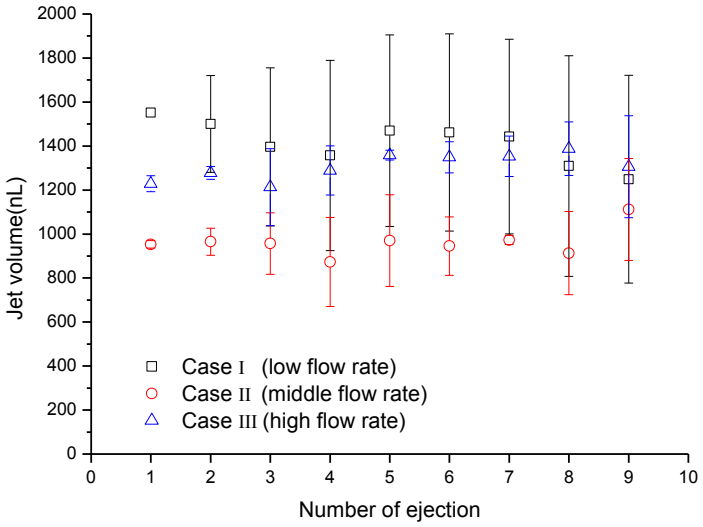

(a)

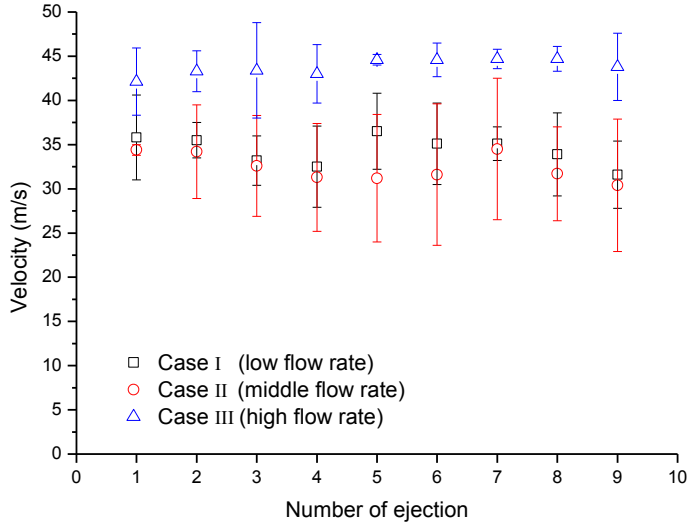

(b)

Fig. 3.22. Relationships between (a) ejected volume of jet and flow rate of drug refill and (b) between jet velocity and flow rate

Er:YAG laser whose wavelength is 2940 nm shows its highest absorption coefficient in the water. Thermal effects such as conduction or diffusion are dominant. This is a potential drawback of a drug delivery system if not properly treated. The amount of accumulated heat energy can be calculated as below equation.

$$Q = m \cdot C_w \cdot \Delta T \tag{3.13}$$

Where Q is the accumulated heat energy through the laser beam, m is the mass of the working fluid (water), C_w is the specific heat capacity and ΔT is the temperature difference from laser heating. In this case, mass of water is 0.42g and specific heat capacity has the value of 4.19 J/g·C. The temperature change of the water inside the chamber was measured using thermocouple as shown in Fig. 3.23 to consider heat accumulation effect.

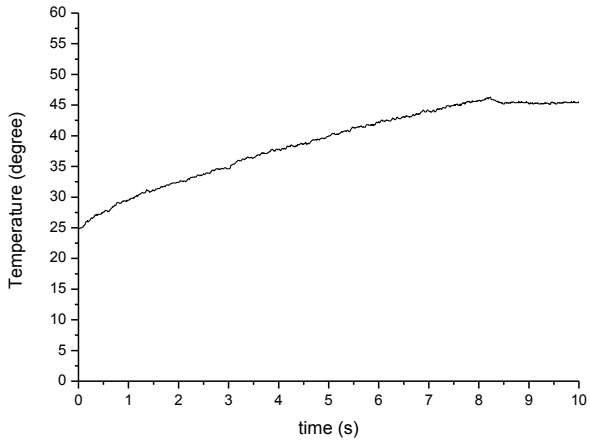

Fig. 3.23. The temperature change of the working fluid inside the chamber

Growth hormones namely EGF (Epidermal Growth Factor) and HGH (Human Growth Hormone) are used to investigate a potential thermal damage done to drugs due to the repetitive laser ablation. Fig. 3.24 shows the rate of increase in the gene expression. EC represents an amount of Laminin in cell which is not treated with EGF. The value of EC is set to one as a reference value. HC denotes an amount of Elastin in cell which is not treated with HGH. Likewise, the value of HC is set to one. E10 and E100 mean the concentrations of Laminin in cell treated with EGF as 10 ng/mL and 100 ng/mL, respectively. Similarly Elastin concentration in cell treated with HGH is denoted H10 and H100. Four cases (E100 408mJ, E10 408mJ, H100 408mJ and H10 408mJ) are considered: growth factor or hormones are contained in a drug reservoir and discharged using a 408 mJ Er:YAG laser. Jet containing growth factor is injected into cell and the amount of each Laminin and Elastin is analyzed. Other cases considered (E100 816mJ, E10 816mJ, H100 816mJ, and H10 816mJ) are done in a similar manner except the laser energy being 816 mJ. Rate for jet generation (E100 408mJ, E10 408mJ, E100 816mJ, E10 816mJ, H100 408mJ, H10 408mJ, H100 816mJ, H10 816mJ) are marked the same as of the regular syringe injection (E100, E10, H100, H10), shown in Fig. 3.24. Here, one confirms that there is no thermal damage associated with injection via the present laser induced microjet injector.

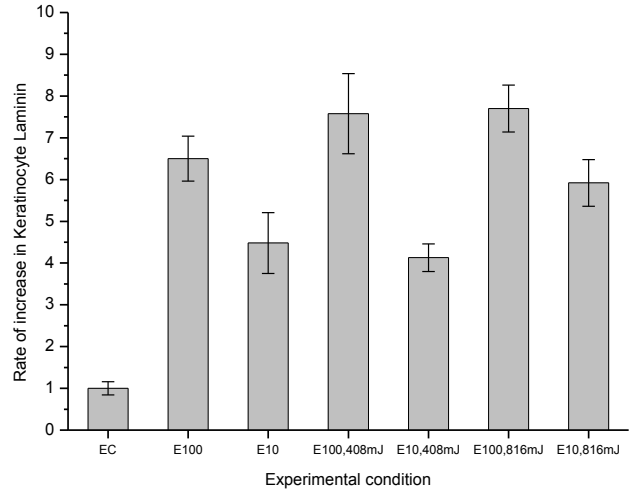

(a)

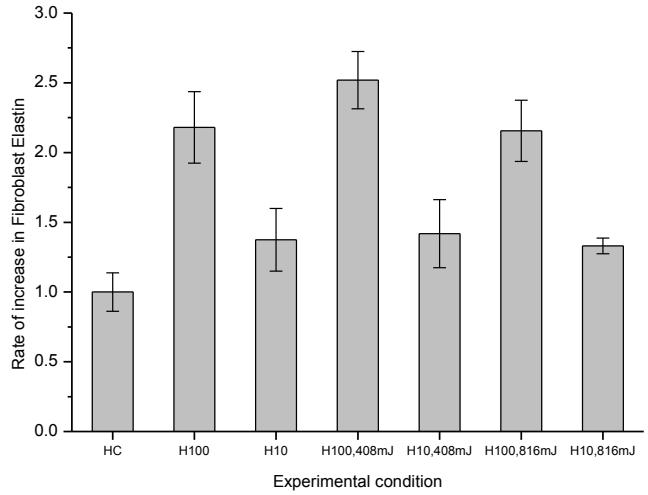

(b)

Fig. 3.24. Rate of increase in (a) Epidermal Growth Factor and (b) Human Growth Hormone. EC and HC are comparison group. Numbers (100, 10) indicate concentration in ng/mL. Laser energies (408mJ, 816mJ) are also shown.

3.5 Optimization of Confined Vapor Bubble for Efficient Microjet Generation

3.5.1 Background and Motivation

In current study, bubble and membrane behavior is reported in detail to analyze process of efficient microjet generation. The relation between motion of bubble and deformation of elastic boundary has been studied by several researchers [31-36]. Gibson and Blake (1982) analyze bubble behavior near deformable surface as some of the earliest works. After that, cavitation bubble near elastic boundary is well described by Blake (1987) and Tomita (2003). Bubble splitting generated by the membrane deformation is observed by both researchers. The response of thin membrane to bubble oscillation is described by Turangan (2006) and Hajizadeh (2012). Research for bubble generated by electric spark near elastic boundary has been done and mushroom shape of the bubble is perceived by Turangan (2006). They also found that bubble characteristics are dominated by distance between bubble and membrane and bubble near a thin membrane in viscous liquids is investigated by Hajizadeh (2012). They analyzed collapse stage of bubble motion such as bubble splitting and jetting phenomena in viscous liquids. Bubble characteristics near flexible surface such as gelatin have been investigated by Kodama and Tomita (2000).

Meanwhile, bubble characteristics in confined geometry such as capillary tube or micro channel have been investigated by several groups [37-40]. H. Yuan (1999) analyzes vapor bubble motion in small tube. In this paper,

growth of bubble volume related with initial bubble size (or size of heater), initial liquid superheats and channel aspect ratios are studied. Numerical calculation of confined bubble in narrow tube filled with viscous fluid is done by E. Ory (2000). They suggest possibility of actuators using vapor bubble, which can pump liquid from one end to other. The vapor bubble induced by super heat in confined geometry is well described by D. B. R. Kenning (2006). The bubble motion controlled by three parameters such as initial superheat, tube diameter and film thickness between wall and bubble is analyzed through the study. Finally, Liaofei Yin (2014) observes phenomena of bubble confinement in micro channel. Bubble growth rate affected by mass flux, heat flux and inlet sub cooling is investigated with high speed CCD camera.

In this way, many studies have been focused on only cavitation bubble near flexible boundary or confined bubble characteristics, respectively. But both membrane response and bubble behavior in confined geometry should be considered together to understand microjet injector system. Chamber height and initial beam spot size are core factors which control characteristics of bubble and membrane. The vapor bubble in free expansion condition is investigated to figure out pulse duration and beam spot size effect on bubble motion. Laser induced bubble in confined geometry is analyzed to describe actual bubble and membrane motion inside of microjet injector. Membrane reaction time is comparable to growth time of bubble and response of membrane is fast enough to follow bubble motion. Finally, jet velocity affected by membrane deflection is considered to assure effective

transdermal drug delivery.

3.5.2 Experimental Approach

The characteristics of laser used in this experiment are following: Er:YAG laser whose wavelength is 2940 nm, pulse duration is 150 μs and utilized energy is 1059 mJ and 1225mJ. The mechanism of microjet ejection is shown as below Fig. 3.25 (a). The laser beam is focused into chamber covered with coated sapphire window through the lens of 100mm focal length. Then, explosive bubble expansion is induced by laser which has high absorption coefficient in water [10]. Membrane is deformed by bubble expansion which is main power source of actuator. Finally, drug is accelerated by membrane deformation and passing through the nozzle whose diameter is 150μm.

In this study, it is found that both bubble and membrane motions are dominated by two parameters such as beam spot size and chamber height. Here, beam spot size is controlled by distance between lens and injector. Initial irradiance is related with beam spot size and bubble size and life time is determined by initial irradiance. Experiments were performed with 45, 65 and 85mm stand-off distance and 8, 11, 13 and 15 mm chamber height.

The characteristics of unconfined bubble are analyzed using following experimental set up (Fig. 3.25 (b)). Same 100mm focal length lens and coated sapphire window are used in all experiments. The laser beam is

focused into the glass chamber filled with water and bubble expansion is started from the window because of high absorption coefficient of Er:YAG laser. Initial irradiance effect on bubble behavior is studied using images of the high speed camera which are taken by 31,007 fps and 40,000 fps, respectively.

For confined bubble case, lens and window are same as unconfined case and membrane composed of the silicon rubber is inserted between two acrylic cylinders as shown in Fig. 3.25 (c). Confined bubble characteristics such as equivalent radius and growth rate of bubble are analyzed. Microjet is captured by the high speed camera at 49,026fps to evaluate injector performance. In summary, detailed experimental condition is given by below Table 3.4.

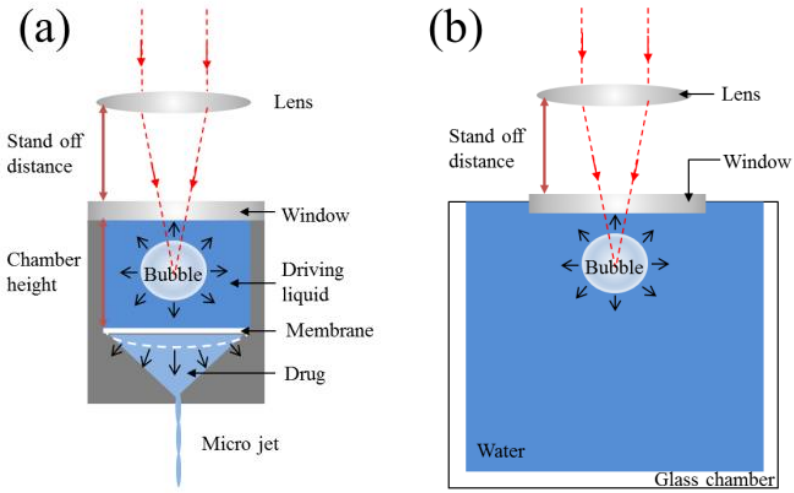

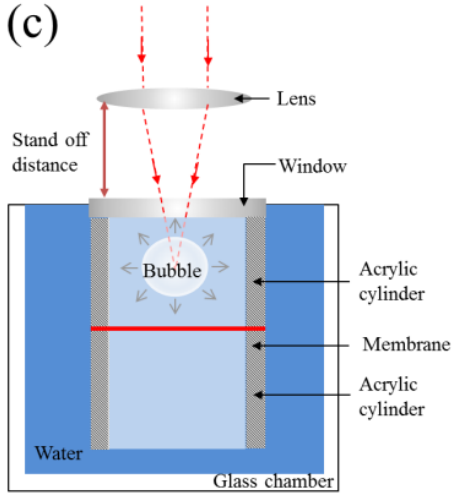

Fig. 3.25. (a) Mechanism of microjet generation, (b) experimental condition of unconfined bubble and (c) confined bubble

Table 3.4. Experimental condition for each case

Case	Energy (mJ)	Pulse duration (μs)	Stand-off distance (mm)	Initial irradiance (MW/cm^2)	Cylinder Height (mm)	Frame rate bubble/ jet (fps)
1	1225	150	45	0.205	Unconfined	31,007/none
2	1225	150	45	0.205	8	31,007/49,026
3	1225	150	45	0.205	11	31,007/49,026
4	1225	150	45	0.205	13	31,007/49,026
5	1225	150	45	0.205	15	31,007/49,026
6	1059	150	65	0.614	Unconfined	40,000/none
7	1059	200	65	0.460	Unconfined	40,000/none
8	1059	250	65	0.368	Unconfined	40,000/none

9	1059	300	65	0.307	Unconfined	40,000/none
10	1225	150	65	0.710	Unconfined	31,007/none
11	1225	150	65	0.710	8	34,000/49,026
12	1225	150	65	0.710	11	34,000/49,026
13	1225	150	65	0.710	13	34,000/49,026
14	1225	150	65	0.710	15	34,000/49,026
15	1225	150	85	40.619	Unconfined	31,007/none
16	1225	150	85	40.619	8	31,007/49,026
17	1225	150	85	40.619	11	31,007/49,026
18	1225	150	85	40.619	13	31,007/49,026
19	1225	150	85	40.619	15	31,007/49,026

3.5.3 Results and Discussion

More elongated shape of bubble is observed with increasing stand-off distance as shown in Fig. 3.26 and this can be recognized by aspect ratio in Table 3.5. This phenomenon is related with absorption coefficient in water. If laser beam penetrates water easily, then bubble expansion is started from focal point of beam. As a result, bubble shape is not affected the distance between lens and water surface. However, if laser beam has high absorption coefficient in water like our case, then bubble is generated from interface between water and window. In this case, beam spot size is varying depending on stand-off distance between lens and water surface. Spot size becomes smaller as stand-off distance becomes longer because of geometrical shape of focused laser beam. The laser energy used in this study

is almost same so higher irradiance is achieved with longer stand-off distance case. Penetration depth that determines bubble length is deepened by higher initial irradiance considering Eq. 3.14 so-called beer's law [41].

$$d = \frac{1}{\mu_a} \ln\left(\frac{H_0}{H_{th}}\right) \tag{3.14}$$

where d is penetration depth of laser beam, μ_a is the absorption coefficient, H_0 is the incident irradiance and H_{th} is the threshold irradiance. Bubble width is determined by initial spot size of beam. In case of shorter stand-off distance, relatively larger width of bubble is obtained and smaller width of bubble is observed for larger stand-off distance case. As a result, if stand-off distance becomes longer then bubble length becomes longer with narrow bubble width such as pear like shape. On the contrary, half spherical like shape is observed for shorter stand-off distance case through the opposite mechanism.

Meanwhile, the phenomenon of bubble departure is observed at 85mm stand-off distance case. This can be explained by the relation between surface tension force and contact diameter [42]. The surface tension force is given by

$$F_s = \pi d_b \sigma \sin\theta \tag{3.14}$$

where d_b is the contact diameter, σ is the surface tension coefficient and θ is the contact angle respectively. The contact diameter of bubble becomes smaller with increasing stand-off distance as shown in Fig. 3.26. At that time, the surface tension force is relatively weak comparing other cases. If the surface tension is not enough to detach each surface of the bubble and window, then bubble surface is apart from window so-called bubble departure phenomena.

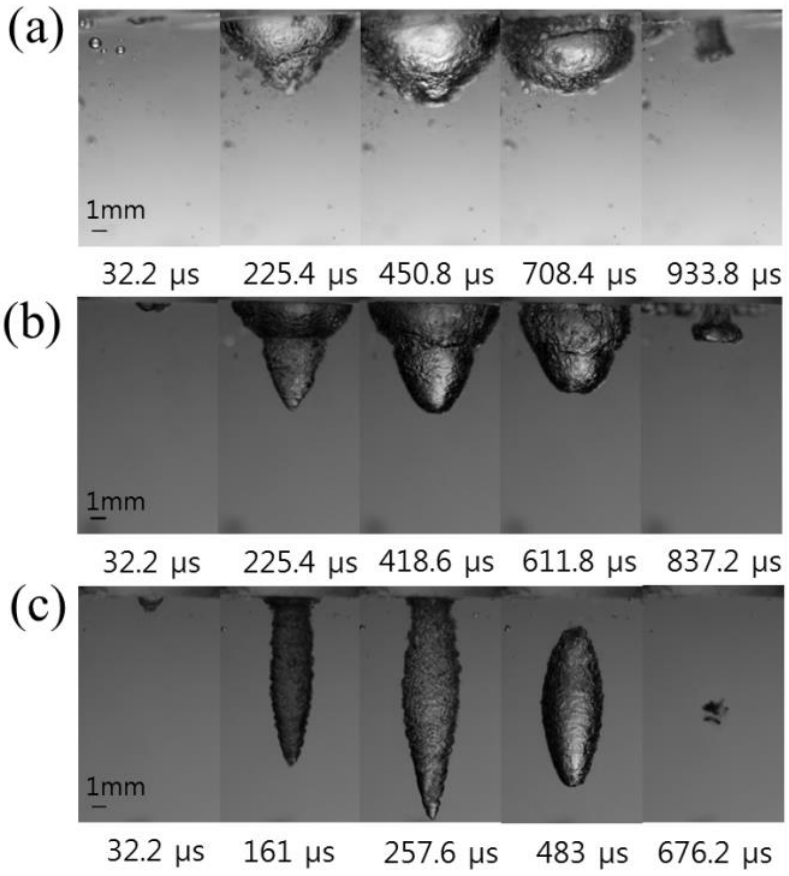

Fig. 3.26. Shape of unconfined bubble generated by laser depending on

stand-off distance: (a) 45mm stand-off distance case, (b) 65mm stand-off distance case and (c) 85mm stand-off distance case

The evolution of equivalent radius is given by below graph (Fig. 3.27) and the maximum bubble radius and growth time are given by below table 3.5. Here growth time means elapsed time until the bubble reaches its maximum diameter. Both maximum bubble radius and growth time becomes decreasing as increasing of initial irradiance. Because relatively larger size of bubble is obtained through the larger beam spot size which is related with stand-off distance and this large bubble is more easily sustainable because both growth time and collapse time are rely on bubble size. A similar phenomenon is observed by J. P. Padilla-Martinez et al (2014) [43].

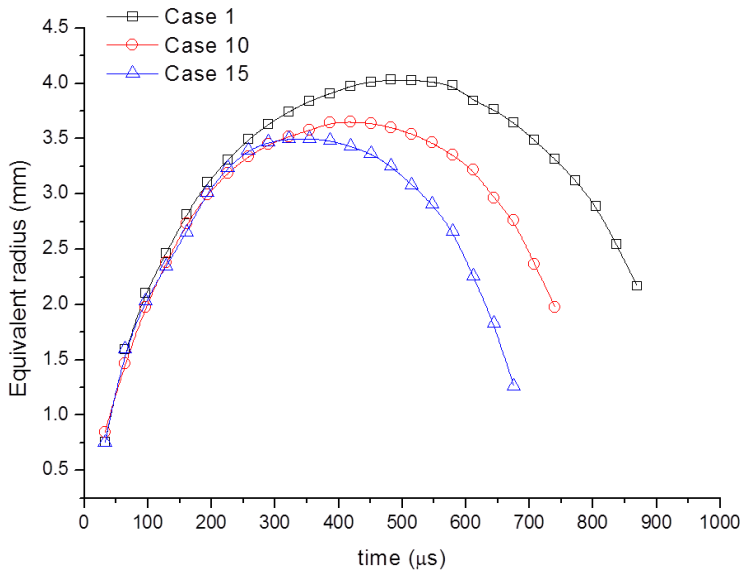

Fig. 3.27. Evolution of equivalent radius with respect to time for

unconfined bubble according to stand-off distance and each case of average error is following: Case 1: ±9.18% , Case 10: ±10.56% ,Case 15: ±12.26%

Table 3.5. Unconfined bubble characteristics depending on stand-off distance

Case	Stand-off distance (mm)	Initial irradiance (MW/cm^2)	Aspect ratio max diameter/ max height	Maximum bubble radius (mm)	Growth time (μs)
1	45	0.205	1.68	4.03	450.8
10	65	0.710	1.05	3.60	386.4
15	85	40.619	0.36	3.50	332.0

The characteristics of unconfined bubble are analyzed in the previous section. In this part, characteristics of confined bubble and membrane are investigated using images of the high speed camera. Below Fig. 3.28 shows the sequential images of bubble and membrane and dashed line represents interface between membrane and water. The vapor bubble is generated by focused laser beam and then silicon membrane is stretched by volume change caused by bubble growth. After that, membrane is contracted to reach its original position while bubble collapse take place inside of injector.

For 45mm and 65mm stand-off distance case, bubble expansion occurs dramatically toward downward direction, because bubble width is enough large to contact wall surface so radial direction of the bubble expansion is restricted by the chamber wall. Similar phenomena were explained by Liaofei Yin (2014) [40]. They also observed fast growth of bubble when

bubble size is large enough to contact wall and it is modified as more elongated shape. Similar phenomenon was observed in our research, which is the longest length of bubble is generated at 45mm stand-off distance case because of relatively larger initial beam spot size comparing other cases.

Meanwhile, elastic response of membrane motion was also captured as shown in Fig. 3.28. Membrane deformation is depending on bubble expansion and response time of membrane is fast enough to follow that of bubble. This relation can be inferred from similar scales of response time both bubble and membrane, which is tabulated below Table 3.6. It is investigated that membrane is most stretched with 45mm stand-off distance. It is obvious results because there is a strong correlation between membrane deformation and bubble expansion.

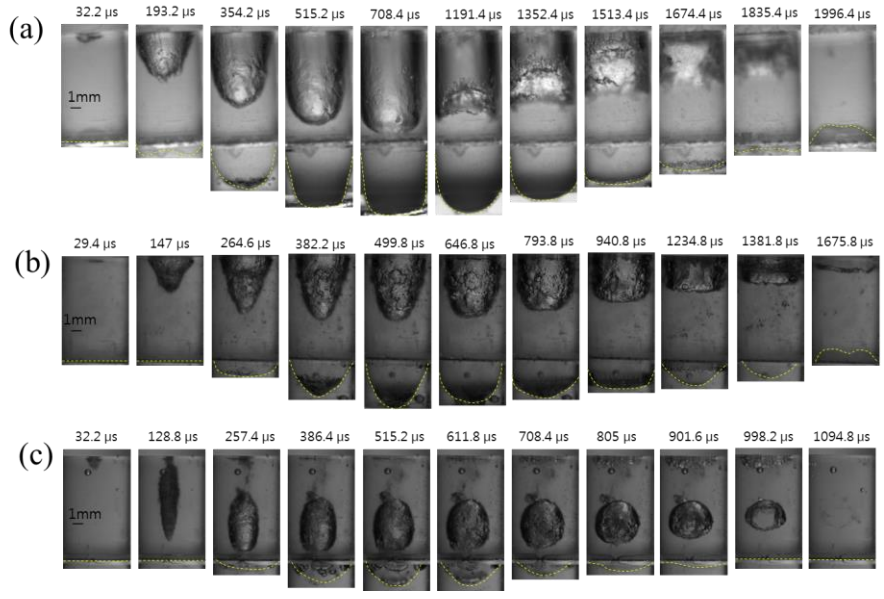

Fig. 3.28. Sequential images of bubble and membrane (dashed line) : (a)

45mm stand-off distance case, (b) 65mm stand-off distance case and (c) 85mm stand-off distance case and all case, cylinder height is 11mm

Table 3.6. Both growth time of confined bubble and membrane determined by combination of stand-off distance and cylinder height

Case	Stand-off distance (mm)	Cylinder height (mm)	Initial irradiance (MW/cm^2)	Growth time of bubble (μs)	Growth time of membrane (μs)
2	45	8	0.205	682.6 ± 84.2	537.7 ± 50.5
3	45	11	0.205	898.0 ± 69.1	873.0 ± 98.5
4	45	13	0.205	837.2 ± 133.2	801.8 ± 85.1
5	45	15	0.205	714.8 ± 60.3	598.9 ± 55.1
11	65	8	0.710	372.4 ± 48.8	467.1 ± 72.7
12	65	11	0.710	444.7 ± 61.7	532.9 ± 89.5
13	65	13	0.710	491.0 ± 86.6	541.0 ± 84.5
14	65	15	0.710	517.4 ± 69.6	535.1 ± 51.5
16	85	8	40.619	407.9 ± 66.4	375.7 ± 73.8
17	85	11	40.619	428.3 ± 45.7	389.6 ± 38.6
18	85	13	40.619	397.1 ± 32.2	357.8 ± 33.9
19	85	15	40.619	354.2 ± 85.9	334.9 ± 37.8

Confined bubble characteristics depending on beam spot size and cylinder height are examined through this study. Life time of confined bubble is much longer than that of unconfined one, which is shown as Fig. 3.29 (a) and (b). Chamber wall impedes bubble expansion in radial direction leading to more sustainable bubble. In each graph, unconfined case is denoted by Case 1 and other cases show confined case. This similar phenomenon is also observed

by A. Hajizadeh Aghdam (2015) [44]. They measured bubble life time in tube is 7 times longer than one in the free expansion condition. For our case, beam spot diameter and cylinder height are core parameters to control bubble characteristic such as life time and growth rate.

Fig. 3.29 (a) represents beam spot size effect on bubble life time. The order of spot size is Case 3 > Case 12 > Case 17 and the order of life time is same as that of spot size because, larger bubble is generated by with relatively large spot size of beam, which leads to longer bubble life time. Meanwhile, effect of cylinder height is verified as shown in Fig. 3.29 (b). Cylinder height increases from Case 2 to Case 5 as ascending order but life time of bubble is largest at Case 3, which implies that optimal value of cylinder height exists. If cylinder height is too short, then length of bubble expansion is restricted. Opposite case, pressure wave generated by bubble expansion will decay dramatically and consequently, membrane deformation becomes smaller comparing optimal case. Small distortion of membrane reduces amount of pumped liquid, which affects size of cavity or bubble size.

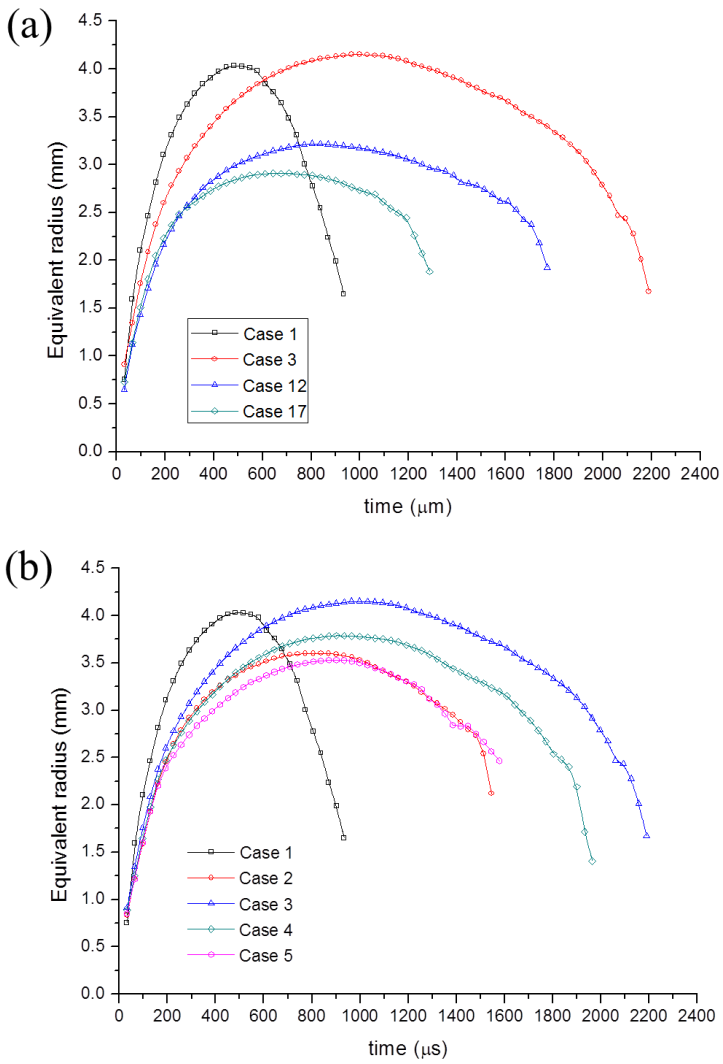

Fig. 3.29. Equivalent radius with respect to time and Case 1 represents unconfined case and other cases have confined geometry. (a) Confined cases have same cylinder height as 11mm but beam spot size is different and (b) confined cases have same beam spot size but have different cylinder height. Each case of average error is following: Case 1: ±9.1% , Case 2: ±9.0% ,Case 3: ±5.6% , Case 4: ±7.5% , Case 5: ±11.6% , Case 12: ±8.1% ,

Case 17: ±9.2%

Growth rate of each case of confined bubble are described as below Fig. 3.30. Same stand-off distance cases share geometrical figure in graph. For example, 45mm case corresponds to rectangular shape, 65mm case matches circle and 85mm case is represented by triangle shape. Because expansion of the confined bubble is constrained by the chamber wall, growth rate of unconfined case is larger than that of confined case regardless of stand-off distance, which can be confirmed by table 5 and Fig. 3.30. For 45mm and 65mm stand-off cases, confined bubble is more elongated comparing unconfined bubble, which is inferred from aspect ratio given by table 3.7. In this case, radial direction of bubble expansion is limited by chamber wall and this momentum is supplied downward direction additionally resulting longish bubble shape. However, in case of 85mm case, aspect ratio of confined case is larger than that of unconfined case, which shows different tendency comparing other two cases. Initial beam diameter is too small to be restricted by chamber wall so there is little delay effect due to chamber wall.

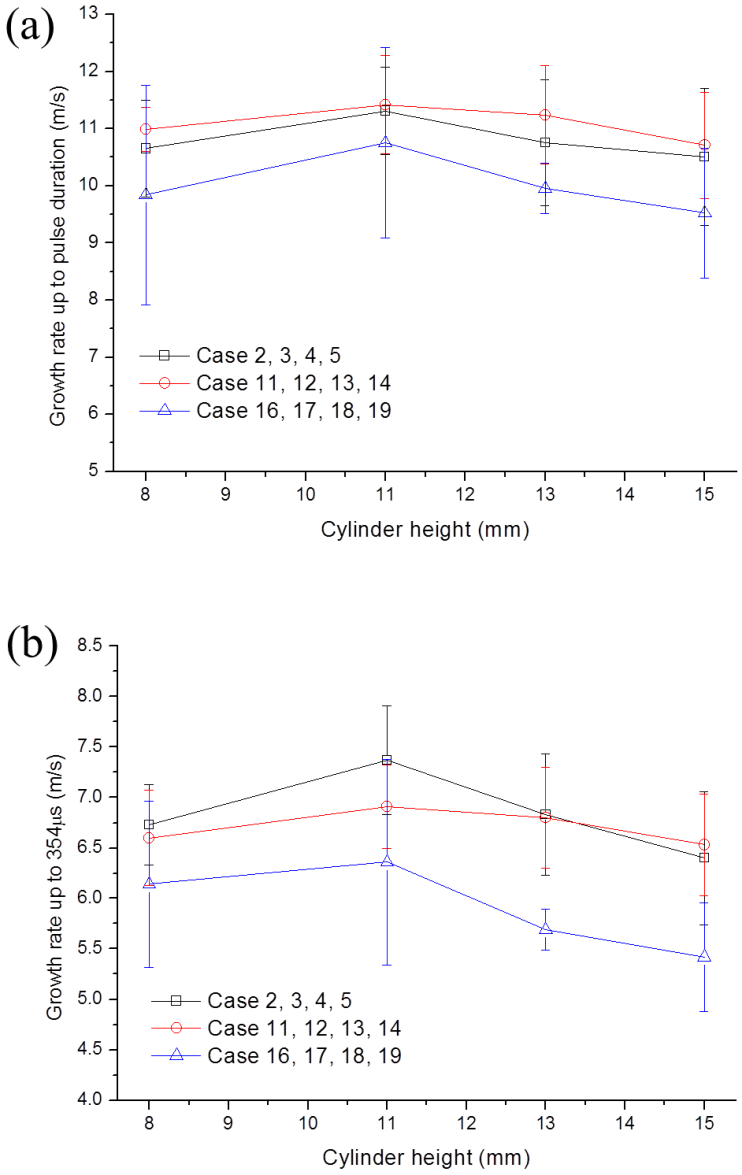

Fig. 3.30. Growth rate of confined bubble up to (a) pulse duration and (b) 354μs

Table 3.7. Both unconfined and confined bubble characteristics depending on stand-off distance and cylinder height, respectively

Case	Stand-off distance (mm)	Cylinder height (mm)	Initial irradiance (MW/cm^2)	Equivalent radius (mm)	Aspect ratio max diameter/ max height
1	45	Unconfined	0.205	3.86 ± 0.15	1.68
2	45	8	0.205	3.60 ± 0.26	0.98
3	45	11	0.205	4.10 ± 0.18	0.67
4	45	13	0.205	3.79 ± 0.26	0.80
5	45	15	0.205	3.53 ± 0.28	0.91
10	65	Unconfined	0.710	3.61 ± 0.21	1.05
11	65	8	0.710	2.87 ± 0.20	0.71
12	65	11	0.710	3.27 ± 0.14	0.69
13	65	13	0.710	3.23 ± 0.15	0.76
14	65	15	0.710	3.17 ± 0.28	0.88
15	85	Unconfined	40.619	3.51 ± 0.22	0.42
16	85	8	40.619	3.01 ± 0.14	0.71
17	85	11	40.619	2.92 ± 0.22	0.65
18	85	13	40.619	2.87 ± 0.14	0.67
19	85	15	40.619	2.51 ± 0.19	0.66

The microjet is discharged through the nozzle whose diameter is 150μm and jet velocity is calculated from jet head. It is measured to find optimal combination of parameters such as stand-off distance and cylinder height. The maximum jet speed was observed between 11mm and 13mm chamber height regardless of stand-off distance, which implies that optimal chamber height exists. If chamber height is short, then there is no enough space for

bubble expansion. However for relatively long chamber height case, volume of liquid slug between bubble and membrane is too large, which decrease pumping efficiency. Similar pumping mechanism is suggested by G. R. Wang (2004) [45]. They found that pumping efficiency is maximized when bubble located at left end of tube, which means that there should be enough space for bubble expansion for efficient pressurization.

Meanwhile, volume growth rate of bubble and membrane is obtained using high speed camera. The trend of growth rate of membrane volume is proportional to that of bubble volume, which is shown as Fig. 3.31 (a) and (b). Similar trend is observed for jet velocity case depicted as Fig. 3.31 (a). It is concluded that membrane motion controlled by bubble expansion is core factor to determine jet velocity.

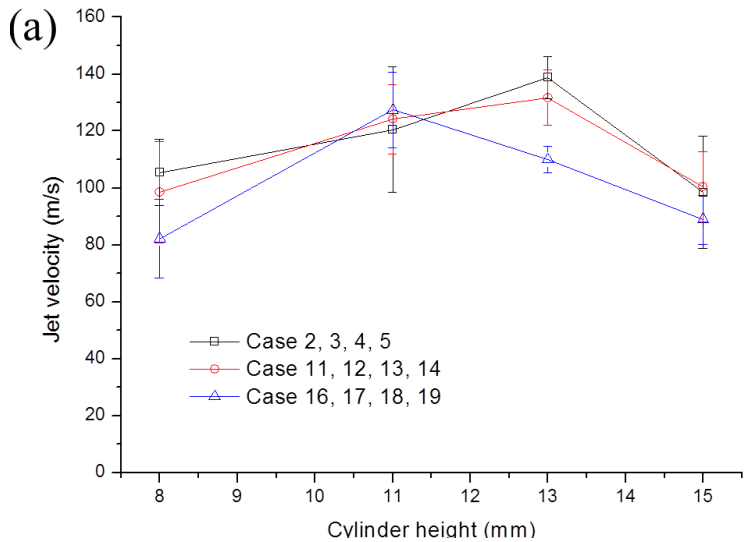

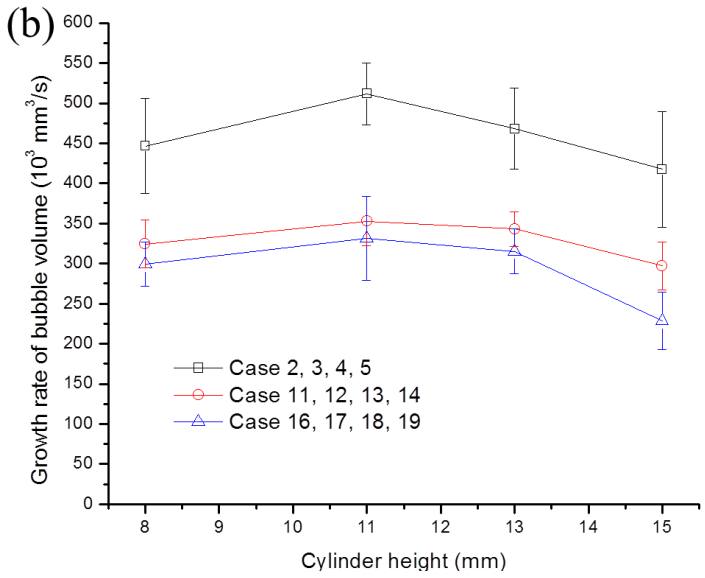

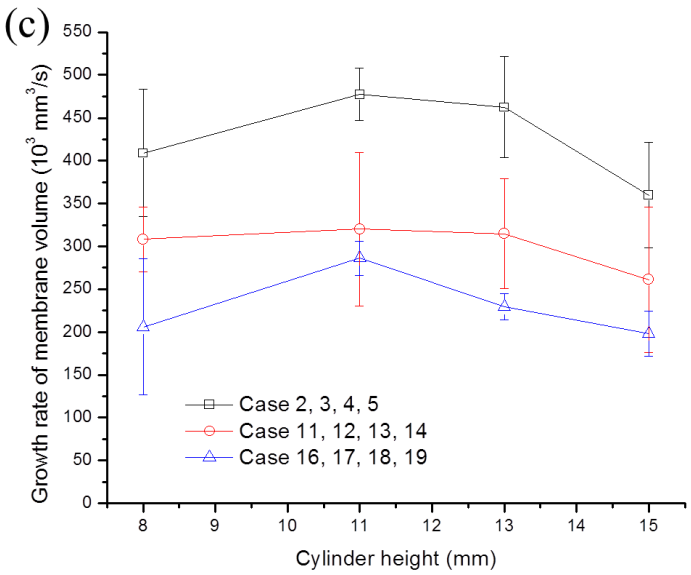

Fig. 3.31. (a) Jet velocity, (b) growth rate of bubble volume and (c) growth rate of membrane volume of each case depending on stand-off distance and cylinder height

Chapter 4. Drug Delivery System Using Laser-generated Microjet and Additional Functions

4.1 Pre-ablation and Microjet Injection

4.1.1 Background and Motivation

Drug delivery system based on the microjet has been studied by various researchers [3, 4, 23, 46]. Several different mechanisms of generating the microjet range from spring, compressed gas, piezoelectric transducer, linear Lorentz force piston, electronic driven bubble, and laser-induced wave or bubble. The introduction of these devices was principally motivated by overcoming needle phobia and contamination from reuse of conventional needle-based system [1-3]. In the spring or gas-powered devices, it is difficult to control drug dose or jet speed with its piston unit, whereas in the piezoelectric transducer, rather precise control of drug dose was deemed possible. The Lorentz force driven injector has shown quite reliable performance in comparison to aforementioned devices. A vapor bubble driven injector for the microjet generation has been proposed in our earlier works [5, 47], where the vapor bubbles is induced by the short pulsed (150 μs) Er:YAG laser beam (2.9 μm) having the best absorptivity in water.

The mechanism of the microjet ejection is as follows: Er:YAG laser beam is focused inside a driving chamber that is filled with de-gassed water. An

explosive growth of vapor bubble in this chamber gives rise to a sudden deformation of the elastic membrane that separates the drug solution from the driving water. The elastic expansion of the membrane pushes the drug solution and drug liquid is ejected through the nozzle of 150 μm diameter. The microjet jet is accelerated to above 100 m/s, which is sufficient for skin penetration and effective delivery of the drug dose. In order to enhance drug delivery efficiency, 20% of the beam is used making a micro hole in the targeted porcine skin before the microjet arrives at the same spot for easier penetration of the porcine skin.

The skin ablation tests using the Er:YAG laser were reported in the literature. The ablation rate of normal spiking mode of Er:YAG was considered, and the effect of different pulse durations such as normal-spiking (200 μs) and Q-switched mode (90 ns) was reported by Walsh *et al*. [48, 49]. Thermal damage was investigated by varying the laser fluence from 0.5 to 81 J/cm^2. Hibst and Kaufmann [50] studied the optimization of Er:YAG laser parameters for skin ablation and suggested that the crater depth is proportional to laser fluence. Hohenleutner [51] reported on the effective conditions of thermal ablation and concluded that thermal damage zone does not increase with the spot size or by the repetition of laser pulses; only the superficial skin is ablated by the Er:YAG laser.

A review of these previous studies on skin ablation using Er:YAG laser suggests that Er:YAG laser can be an effective means of ablating the superficial skin layer with minimal thermal damage whereby subsequent microjet injections can be significantly enhanced. In the present study, a

combined scheme of skin ablation and microjet injection is used. The drug injection is synchronized by the skin ablation prior to microjet ejection with a time delay between the two processes. A series of high speed camera images are used to investigate the detailed response and responsible mechanism of the laser-based microjet device which makes good use of the elastic membrane and the explosive growth of a large-sized vapor bubble. The rate of expansion for both bubble and membrane is similar, suggesting that the system is optimally designed for efficient transdermal delivery of drug. The confocal microscopy is used to quantify the depth of drug penetration into a porcine skin treated by FITC staining using the present delivery scheme. Furthermore, the penetration process inside of the gel is analyzed by using the high speed camera images.

4.1.2 Experimental Approach

The microjet is generated by a focused Er:YAG laser beam which has a high absorption coefficient in water [10]. The laser used in this study is a custom made, built from a standard Er:YAG laser (B&B system, Anybeam) for dental procedures. The generated beam from the unit passes through the articulated arm consisting of mirrors until focused by a lens of 100 mm focal length. The specification of laser used in this study is as follows: wavelength is 2940 nm and pulse duration is 150 μs. Bubble is confined by 11 mm height chamber and stand-off distance between center of lens and injector top surface is 45 mm. In this experiment two kinds of experiments are

conducted. In first case, the laser beam whose energy is 1085 mJ is focused into a chamber of injector through the coated sapphire window. Explosive bubble growth occurs as a result of laser beam focusing. The elastic membrane starts to deform due to sudden pressure rise caused by the bubble expansion. Then the microjet is discharged from the nozzle of 150 μm diameter by the deformation of the membrane. This is referred to as the Microjet Only (w/o Ablation) case.

The second case is represented in Fig. 4.1 that illustrates the use of a beam splitter in the Pre-ablation Microjet (w/Ablation) case. The concept of the combined pre-ablation and microjet ejection is developed in order to increase the efficiency of drug delivery. The laser beam labeled 1 passes through a beam splitter with an 80% transmittance and a 20% reflectance. The transmitted energy of 860 mJ is focused into the driving water in the upper chamber through the sapphire window. The generation of a microjet is identical to the Microjet Only case. Now the reflected laser beam denoted 2' is reflected by a mirror and then focused into a porcine skin through a lens whose focal length is 100 mm. The expected ablation hole depth and diameter may be inferred from the reference works [48-51] on skin ablation with Er:YAG laser, which is shown as below Table 4.1. The penetration depth is within 500 μm, and the hole diameter is expected to be larger than the microjet diameter (150 μm). In the present experiment, the laser energy is adjusted to satisfy the target depth and diameter, and such the laser fluence of 87 J/cm^2 is used for the present experiment. As for the optimum angle of the ablation beam, we find the angle to be 60 degrees from the skin surface.

A micro hole is created by the pre-ablation scheme, and the hole position is optically aligned with the drug jet impact position. The resulting microjet velocity reached about 69~105 m/s.

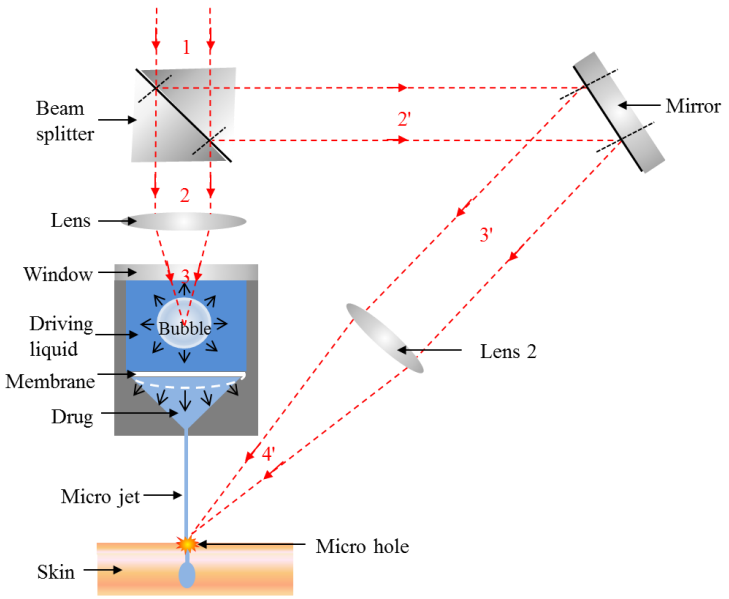

Fig. 4.1. Schematic of drug delivery with pre-ablation followed by a microjet injection using a beam splitter

Table 4.1. Depth and diameter of the ablation hole on the target skin at given laser fluence

	Pulse duration	Target	Fluence (J/cm^2)	Depth (μm)	Diameter (μm)
Ablation + Microjet (Our study)	150 μs	Porcine skin	87	417	679
Walsh *et. al* (1989), Ref. 10	200 μs	Guinea pig skin	50	250	1100
	200 μs	Guinea pig skin	80	400	1100
Walsh *et. al* (1989), Ref. 11	90 ns	Guinea pig skin	25		5-10
	200 μs	Guinea pig skin	25		10-50
Hibst *et. al* (1991), Ref. 12	250 μs	Porcine skin	60	320	900
	250 μs	Porcine skin	80	400	900
Hohenleutner *et. al* (1997), Ref. 13	250 μs	Human skin	4	11.2	25-100
	250 μs	Human skin	7	15.6	25-100

Bubble behavior, membrane response, and microjet ejection are monitored by the high speed camera images (KOMI, Phantom V711). The detailed characteristics of bubble, membrane, and microjet are also obtained from the images. The process of a large bubble generation in the driving chamber reveals that its height reaches 11 mm as it is recorded at the rate of 31007 fps. The deflection of the elastic membrane that separates drug from water within the injector is also captured by the high speed camera. The resulting microjet

ejections are taken at 49026 fps.

Both penetration experiments using Polyacrylamide gel (PAAG) and porcine skin were performed to quantify the depth, width and injected volume. Black ink is injected into 10%, 20% and 30% weight ratio of PAAG, and the injected volume is captured by Nikon camera. Each component of PAAG is similar to those used in [52]. The process of penetration is also taken by a high speed camera at 40,000 fps to obtain the instantaneous images of the microjet injections, with and without ablation. The penetration experiment on the abdominal porcine skin is also performed. For visualization of the penetration depth within the skin, the injecting liquid is prepared by dissolving 1 g/L of fluorescein isothiocyanate (FITC) in Dulbecco's phosphate-buffered saline (DPBS). Multiple planar images at specific depths are obtained using a confocal microscopy (Zeiss, LSM710). The laser conditions were as follows: 1085 mJ for Microjet Only and 1035 mJ for Pre-ablation Microjet with 10 Hz for porcine skin and gel.

4.1.3 Results and Discussion

The typical bubble and membrane motions of Microjet Only case imaged within a transparent injector are carefully studied. Fig. 4.2 shows sequential images of a stretched bubble and the membrane expansion. The laser beam is focused inside the upper chamber separated from a lower drug by a membrane (dashed line). The expansion and collapse of the bubble take place inside the driving water chamber surrounded by an upper window,

acrylic cylinder wall and a silicon rubber membrane at the bottom. One observes rapid growth of a vapor bubble fully expanded within the upper chamber. As a result, membrane is stretched several millimeters long as shown in the figure. There is a short time elapse between the bubble and the membrane expansion. The maximum stretch by the membrane is attained when a bubble reached its maximum volume, which is shown at 708.4 μs. Consequently, membrane contracts to return to its un-stretched position as the bubble collapse takes place.

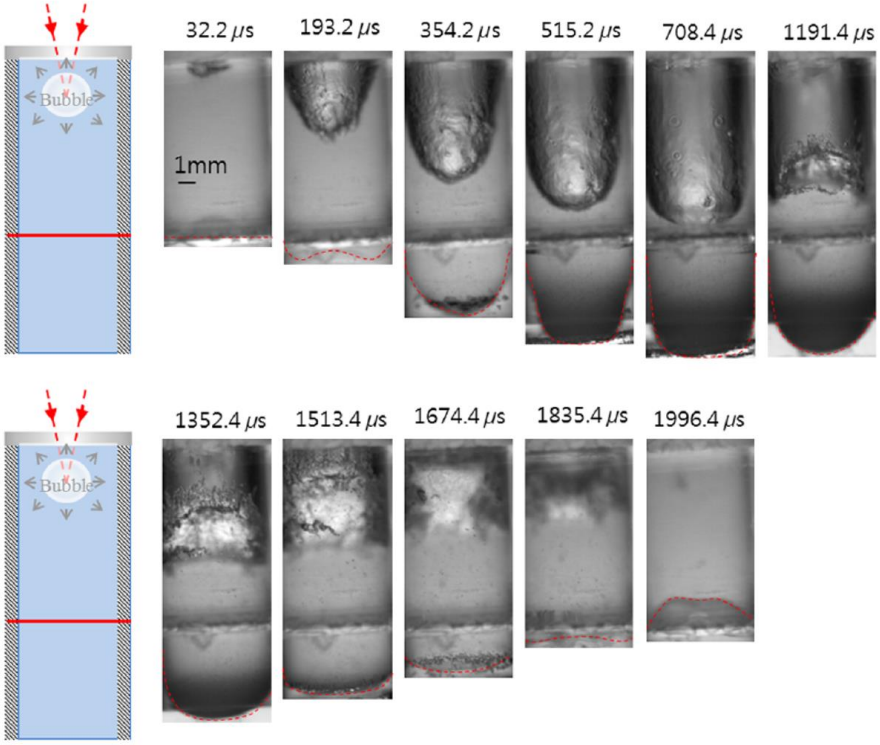

Fig. 4.2. Sequential images of bubble (upper chamber) and a membrane (dashed line) that separates upper water and lower drug

The dynamics of a membrane is strongly dependent on the bubble expansion. Shown in Fig. 4.3(a), the growth rate of a bubble and that of a membrane are quite similar. Here, error bar obtained from 10 times repetitive experiments for both bubble and membrane. Also the rates of decay for both bubble and membrane are also comparable, suggesting that the dynamic response of the confined bubble in the upper chamber and the stretch of the elastic membrane for drug ejection is related to each other.

The membrane deflection is dominated by the pressure loading such that the nonlinear Föppl membrane theory applies [53]. For thin membrane, the pressure is proportional to the cube of midpoint deflection of the membrane, which can be estimated by using Eq. (4.1).

$$P = \frac{Eh}{a^4}\left(\frac{w_0}{g(v)}\right)^3 \tag{4.1}$$

$$g(v) \approx 0.7179 - 0.1706v - 0.1495v^2 \tag{4.2}$$

Here E=1 MPa is Young's modulus of the membrane, h=0.1 mm is the membrane thickness, a=7 mm is the diameter of membrane, w_0 is the midpoint deflection of the membrane obtained from the high speed camera images, υ=0.47 is Poisson's ratio and g(υ) is calculated as a function of the Poisson's ratio [53]. The stretched lengths of bubble and membrane are obtained from the high speed camera images and presented in Fig. 4.3(a). The pressure estimation based on this equation is illustrated in Fig. 4.3(b). The

pressure starts to increase rapidly once the bubble expansion begins. There is a time delay between the on-set of bubble expansion and that of pressure rise. A single cycle of growth and collapse is less than 2000 μs, and during that time, the pressure eventually reaches its equilibrium.

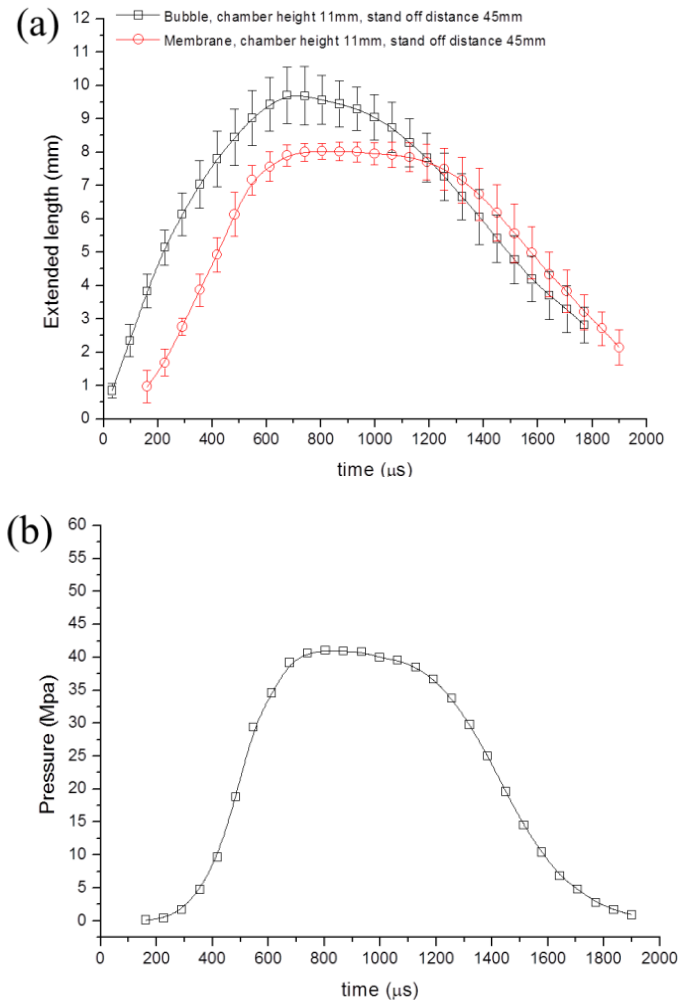

Fig. 4.3. (a) Extended lengths of bubble and membrane taken from high speed camera images and (b) calculated pressure incurred on thin membrane

The microjet as it is discharged from a nozzle of 150 μm diameter is illustrated in Fig. 4.4. The jet velocity in Microjet Only case is 120.5 m/s ± 22.0 m/s, while in Pre-ablation Microjet case, it is 87.1 m/s ± 18.2 m/s. A relatively slower jet velocity is observed when the laser energy is split 1:4

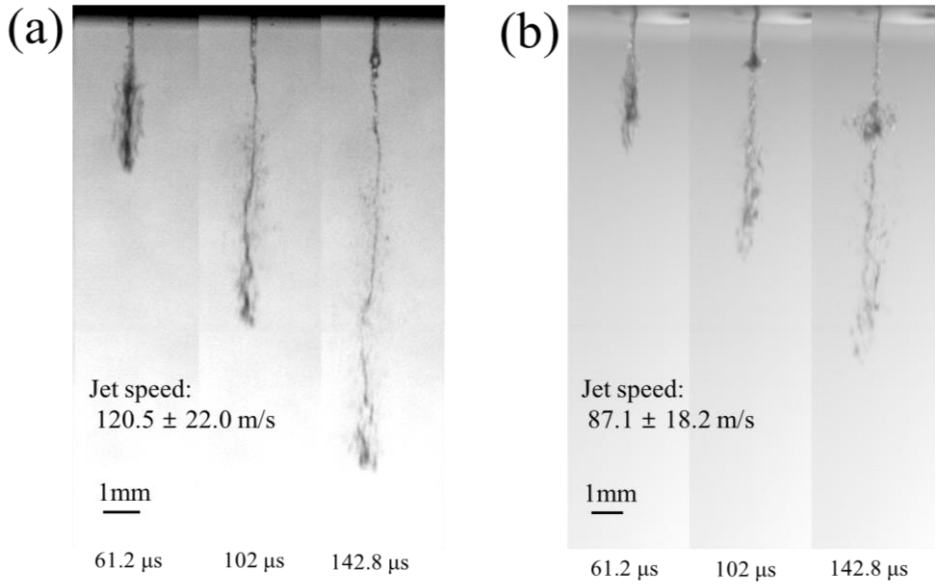

Fig. 4.4. Sequential images of microjet ejection for (a) Microjet Only and (b) Pre-ablation Microjet case

A test of three different gel strength (PAAG 10%, 20%, 30%) is performed as the range of Young's modulus of each PAAG varies from 0.06 MPa to 0.38 MPa, which are applicable soft tissue phantom [52]. The penetration depth and the injected volume are obtained from the images from gel tests, and they are illustrated in Fig. 4.5 and Table 4.2. Each error bar is measured through the repetitive injection of 10 times. For Microjet Only case, the penetration

depth per energy decreased with the gel strength while the effect of gel strength is not significant in Pre-ablation Microjet case. This trend is more visible in Fig. 4.5(b) where the injected volumes for the ablation case are nearly constant regardless of the gel strength. Thus the present combined scheme is an effective means of drug delivery for the target of varying skin strength.

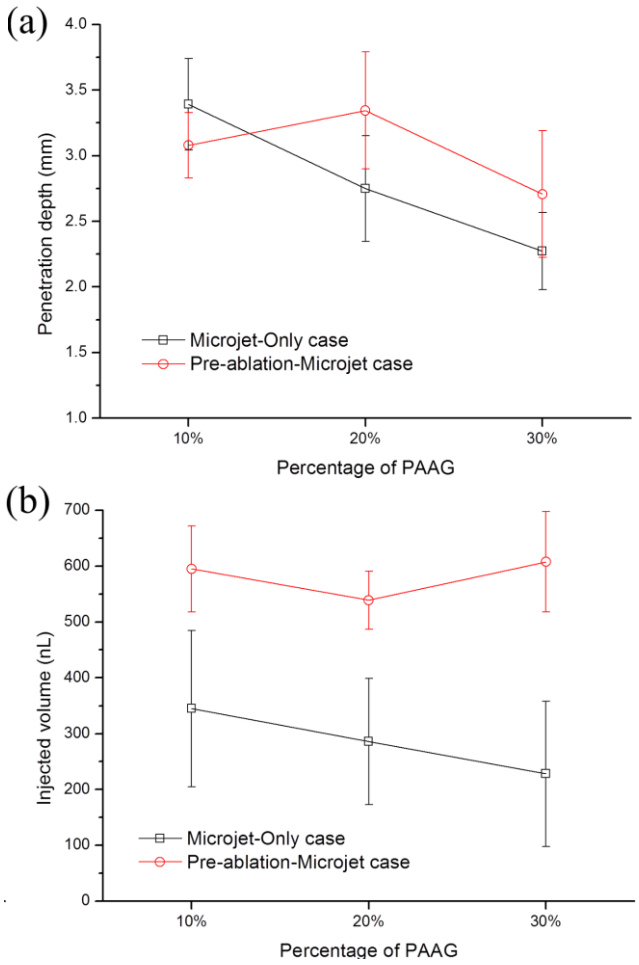

Fig. 4.5. Penetration parameters ((a) depth, (b) injected volume) for each case

Table 4.2. Efficiency parameters (Penetration depth and Injected volume) of microjet injection are less sensitive to gel strength w/ Ablation than w/o Ablation

	Penetration depth per energy (mm/J)	Injected volume per energy (μL/J)	Penetration depth per energy (mm/J)	Injected volume per energy (μL/J)
	w/o Ablation	w/o Ablation	w/ Ablation	w/ Ablation
10% PAAG	3.124	0.318	2.974	0.575
20% PAAG	2.534	0.264	3.231	0.521
30% PAAG	2.095	0.220	2.615	0.587

The high speed camera images show that for Micorjet Only case, the volume of injected ink has its maximum size at about 100 μs as shown in Fig. 4.6, which can be regarded as equilibrium point between expansive force occurred by jet and restoring force of gel. In Pre-ablation Microjet case shown in Fig. 4.7, laser ablation creates a hole before the microjet is injected. The jet speed in this case is 87.1 m/s, as such the growth rate of the injected volume in the gel is slower than Microjet Only case.

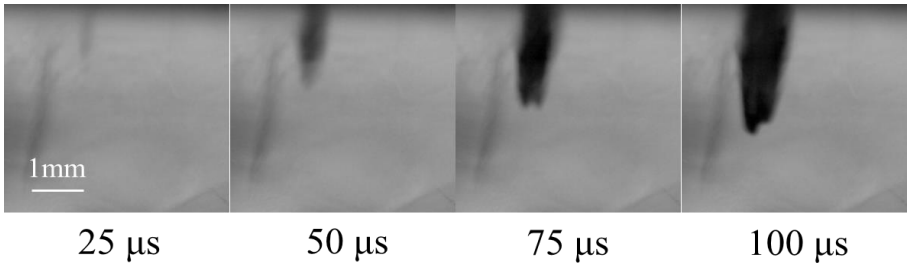

Fig. 4.6. Microjet Only case: sequential images of penetration of 10% PAAG

with black ink

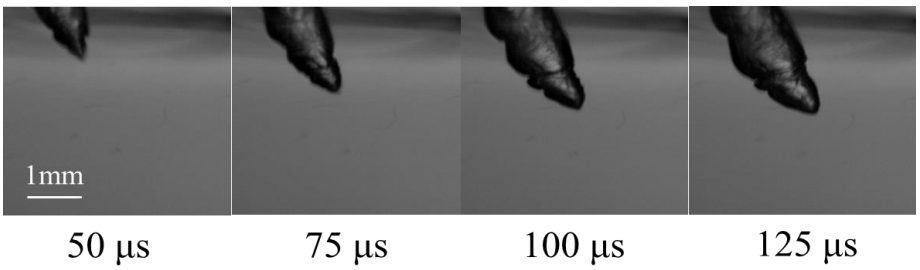

Fig. 4.7. Pre-ablation Microjet case: sequential images of penetration of 10% PAAG with black ink

The penetration experiment with abdominal porcine skin is also conducted to compare drug transfer efficiency and FITC (1 g/L) is dissolved in DPBS and injected into the skin to understand the depth of penetration and distribution of the delivered dose in the porcine epidermis (~ .5 mm below the outer layer). The number of penetration experiments was 5. Fig. 4.8 shows the confocal microscopic images taken for Microjet Only case and Fig. 4.9 shows those of Pre-ablation Microjet case. Each is a planar image taken at every 20 μm depth. The merged images of confocal microscopy for both cases are also provided in Fig. 4.10. In Fig. 4.8, a single hole in the center is seen with well spread of FITC stained tissue. The size of the hole becomes narrower with increasing penetration depth and the maximum depth of reach by the staining solution is about 350 μm ± 71 μm as shown in below Table 4.3. For Pre-ablation Microjet case in Fig. 4.9, a hole created by a direct laser ablation is perceived. The staining agent penetrates right through this

pre-ablated spot (a microhole). The penetration depth in this case is larger and it is 417 μm ± 108 μm, suggesting that pre-ablation is quite useful. Even though the jet velocity is slower, a better drug delivery is attained by the combined pre-ablation and microjet injection that ensured a cleaner, deeper and softer drug passage (see Table 4.3).

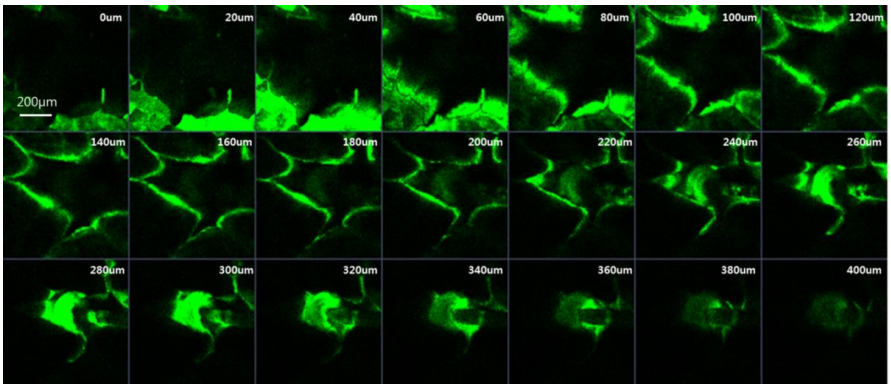

Fig. 4.8. Confocal microscopy image of penetration of porcine abdominal skin with FITC (Microjet Only)

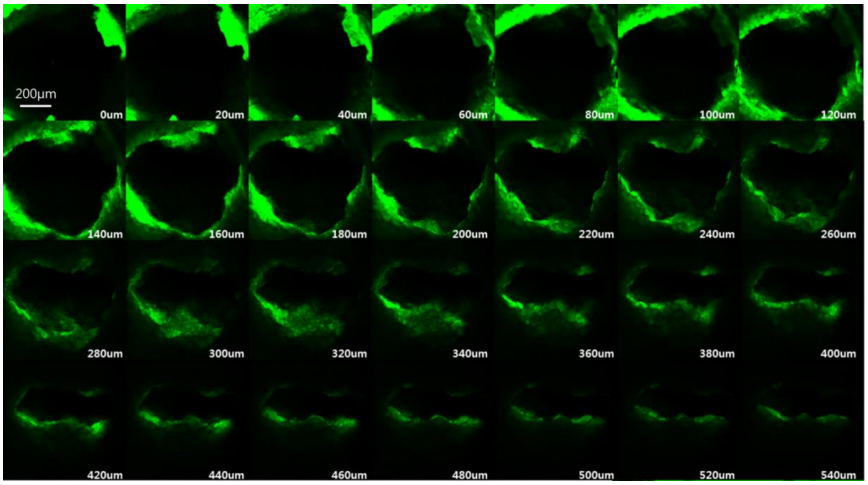

Fig. 4.9. Confocal microscopy image of penetration of porcine abdominal skin with FITC (Pre-ablation Microjet)

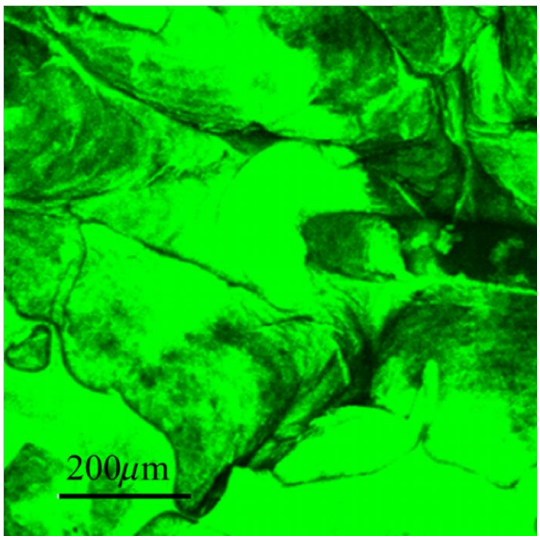

(a)

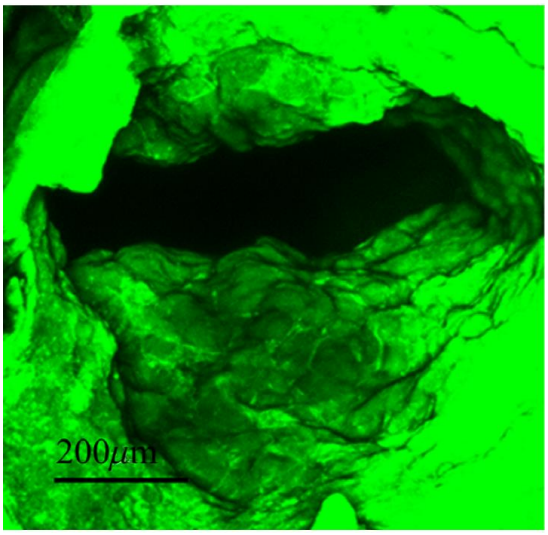

(b)

Fig. 4.10. Merged confocal microscopy image of (a) Microjet Only case and (b) Pre-ablation Microjet case

Table 4.3. Porcine skin test result on Microjet injection w/ and w/o ablation

	Penetration depth (μm)	Hole width (horizontal) (μm)	Hole width (vertical) (μm)
w/ Ablation	417 ± 108	679 ± 26	513 ± 129
w/o Ablation	350 ± 71	614 ± 191	723 ± 42

The confocal images obtained from the repetitive experiments (5 times) are used to quantify depth and width generated by the skin ablation. The width is measured at center of both horizontal and vertical axis. The value of averaged maximum width of horizontal and vertical axes is 679 μm ± 26 μm and 513 μm ± 129 μm, respectively. The shape of the hole is estimated from variation in the averaged width with respect to the depth as shown in Fig. 4.11.

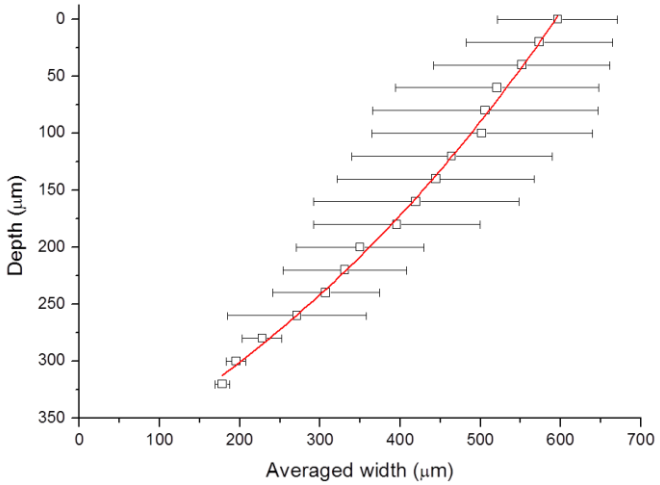

Fig. 4.11 Variation of skin penetration depth with varying hole width

4.2 Synchronization of Skin Ablation and Microjet Injection

4.2.1 Background and Motivation

The on-going efforts to apply microjets for transdermal drug delivery are focused on overcoming known drawbacks of conventional needle injection, such as needle phobia and contamination due to needle uses [5, 27, 47, 54]. The stratum corneum, the outer most layer of skin, is a tough barrier that prevents permeation of foreign substances into the immune system [55]. Overcoming this barrier in order to deliver drugs through percutaneous injection is a major challenge. One possible way of overcoming the barrier is via a pulsed mid-infrared laser that selectively removes or lifts the stratum corneum [56]. The Er:YAG laser is a candidate that has high absorption coefficient in water as human skin is comprised mostly of water, 70% [10]. For this reason, the use Er:YAG laser in the superficial ablation of human skin has been reported in the literature [50, 56, 57].

The Er:YAG laser is also useful for generating a vapor bubble because of its high absorptivity in water. An explosive expansion of vapor bubble is a driving mechanism of the fast and narrow microjet ejection [5, 27, 47, 54]. As the laser beam of 2.9 um is focused inside a chamber filled with water, the vapor bubble starts to grow from the point of irradiation that gives rise to the expansion of the membrane between water and drug. As a result, drug is ejected through a nozzle as a microjet of 150 um diameter [54].

In this paper, we discuss a novel design of such system that makes use of

the combined strategy of pre-ablation of the target skin before the microjet injection is applied for enhanced delivery efficiency. In an effort to make the integrated system compact, a L-shape injector is designed and compared with previous inventions. The bubble motions and subsequent microjet ejections are analyzed via the high speed camera images and the theories. The porcine skin penetration results support the enhancement achieved by the presented combined system for the trans-dermal drug delivery with a microjet injector.

4.2.2 Experimental Approach

Figure 4.12(a) illustrates microjet injection only, and the combined injection system using pre-ablation of skin is shown in Fig. 4.12(b) [54]. This second system was improved by the use of an L-shape chamber and a parabolic mirror shown in Fig 4.12(c). The enhancements expected from the design change are related to simplifications of the experimental set-up and reductions in stand-off distance, likely to be miniaturized even further. In the previous system (Fig. 4.12(b)), there are four optical components (one beam splitter, one mirror, and two lenses) required, whereas three optical components (one beam splitter, one parabolic mirror, and one lens) are used in Fig. 4.12(c). The stand-off distance between the lens and injector is shorter because of the almost horizontal direction of the ablation beam. Too far of a stand-off distance may incur the jet atomization which affects the

efficiency of microjet penetration into the skin.

The experimental set up of the newly designed system is as follows. The Er:YAG laser is used as a beam source; it is set at a 2940nm wavelength and 150μs pulse duration. 80% of the source energy (929.9mJ ± 6.0mJ) is reflected and the residual energy (224.2mJ ± 2.4mJ) is transmitted by the beam splitter. The reflected beam is directed into the water through the lens (focal length, 100mm) and a sapphire window. The optimal distance between the lens and the injector is 50mm; that distance ensures proper beam spot size for efficient expansion of the vapor bubble. The transmitted beam is focused onto a target skin surface via the parabolic mirror (focal length: 101.6mm). The transmitted beam is nearly horizontal and it passes through the gap between the injector and the skin.

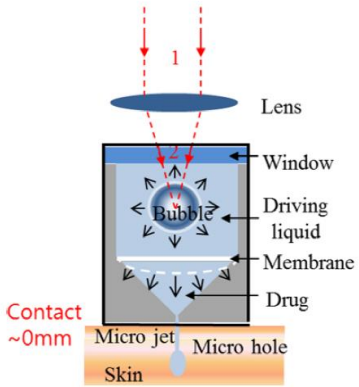

(a)

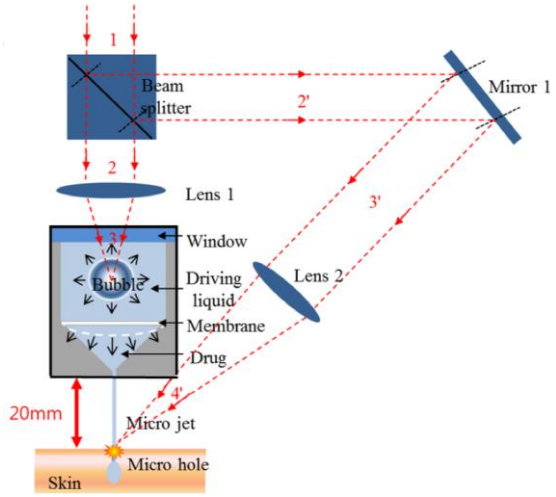

(b)

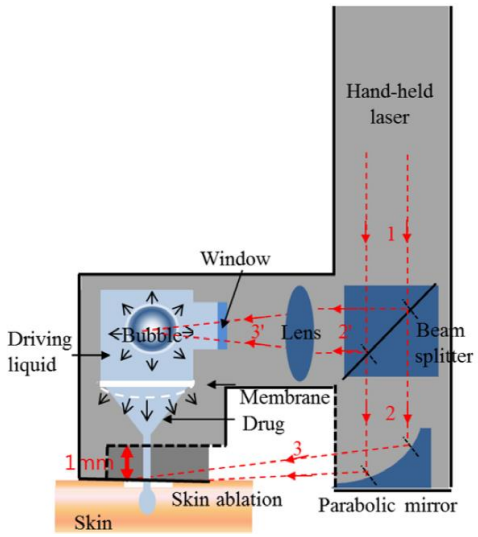

(c)

Fig. 4.12 Schematic of (a) microjet injector, (b) (former system) combined ablation and microjet injector, and (c) (new) L-shape injector and ablation system

The distribution of a single energy source is made based on the minimum energy necessary for localized skin ablation and to supply most of the energy for generation of effective microjet. The threshold intensity for skin ablation is 0.6 J/cm^2 ~ 1.6 J/cm^2 [51]. The capacity of the pre-ablation beam of our system is 2.2 J/cm^2, which is slightly higher than the threshold ablation decided by the size of the ablated area with minimal energy. Beam spot size is important to control the fluence because targeted superficial tissue surface can be eliminated with minimal damage through the proper condition.

The stand-off distance is kept near zero or injector touching the target when delivery is done via method of Fig. 4.12(a). For the combined method of Fig. 4.12(b), the stand-off distance was required to be 20mm because of the angle between ablation beam and skin was 60 degrees. It was shown that such relatively large gap between nozzle and skin had adverse effect on the skin penetration considering the characteristics of microjet atomization illustrated by the jet images in Fig. 4.13. In the figure, the injector nozzle diameter is 150μm, nozzle angle is 30 degrees, and black ink is loaded in the drug chamber. It is quite evident that the breakup of the microjet occurs farther down the jetting axis. It is also suggested that the shorter distance to the skin would allow a focused and intensified jet to penetrate the skin as atomization process can be disregarded if that distance is minimized. Therefore, the stand-off distance used in the new design is 1mm. This off-set distance is kept constant by utilizing a ring perforated on one side for incoming beam, attached to the nozzle tip as shown in Fig. 4.12(c).

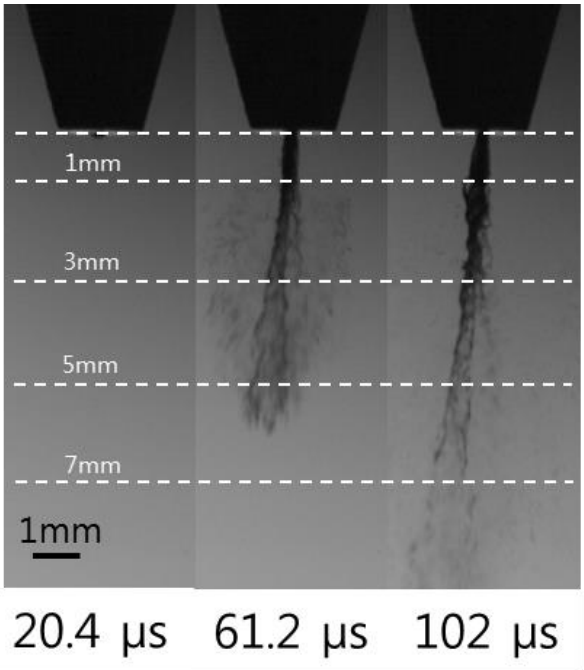

Fig. 4.13 Typical sequential images of microjet ejection

4.2.3 Results and Discussion

The motion of vapor bubbles in cylindrical chamber and L-shape chamber is recorded with a high-speed camera in an effort to visualize pumping actuation of the elastic membrane. The growth of the bubbles in both type of chamber geometries are shown in Figs. 4.14 and 4.15, for the same incident laser energy 954.7mJ in the upper water chamber. In either case, the laser beam is absorbed and dynamic response of an elastic membrane is shown fast enough to assure effective microjet ejection.

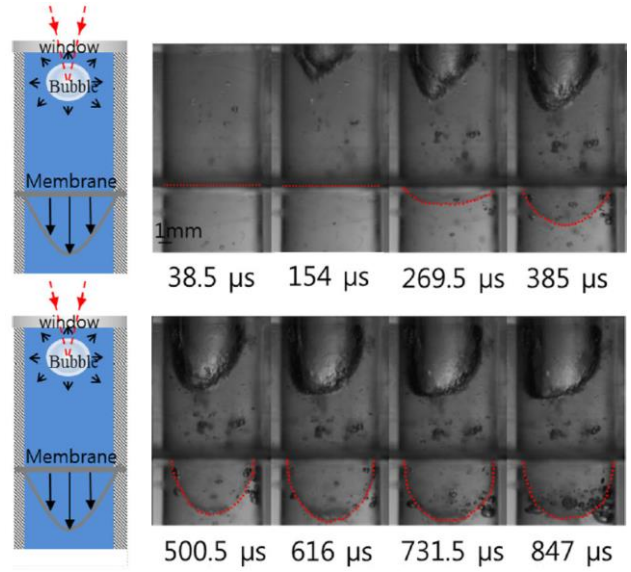

Fig. 4.14 Sequential images of vapor bubble and membrane motion in a cylindrical chamber

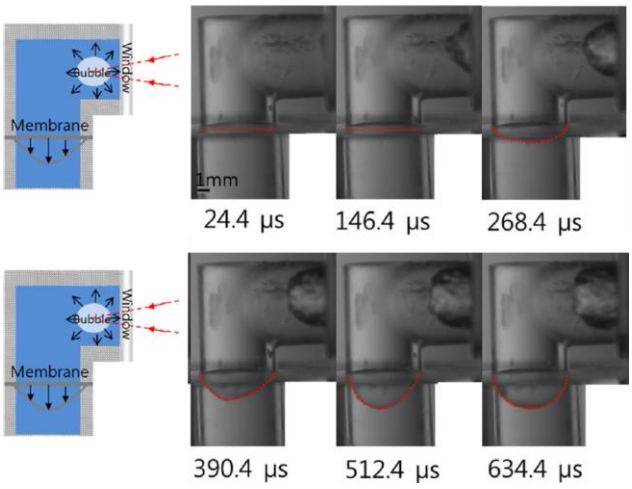

Fig. 4.15 Sequential images of vapor bubble formation and membrane motion in an L-shape chamber

The motion of the bubbles is analyzed though the graphs in Fig. 4.16, showing the radius and rate of volume change. The radius is calculated from the measured volume assuming that the bubble is spherical. From equations (4.3) to (4.5), it is clear that jet velocity is related to the rate of volume change. The flow rate, Q is given by equation (4.3) where V_j is jet velocity, R_n is nozzle radius and $\dot{V}_{l,p}$ is the rate of flow of the liquid. The flow rate of a pumped liquid is proportional to the change in volume of the membrane ($\dot{V}_m$), and is relative to that of the bubble ($\dot{V}_b$); see equation (4.4). The rate of bubble volume change is crucial in deciding the jet velocity which, in principle, sets the criterion for penetration ability as shown in equation (4.5).

$$Q = V_j \times \pi R_n^2 = \dot{V}_{l,p} \tag{4.3}$$

$$\dot{V}_{l,p} \propto \dot{V}_m \quad \text{and} \quad \dot{V}_m \propto \dot{V}_b \tag{4.4}$$

$$V_j \propto \dot{V}_b \tag{4.5}$$

In the figure, the average errors are given as follows: for radius, cylinder is 6.3% and L- shape is 3.4%, while for rate of volume change, cylindrical is 23% and L-shape is 18%. Regardless of chamber shape, the bubble continues to grow up to 200μs. Afterwards, L-shape chamber allows slower

bubble expansion. This suggests that the expansion of the bubble is controlled by laser pulse energy until 200μs. Beyond this point, the expansion within L-shape chamber is limited by the chamber wall as shown in Fig. 4.16.

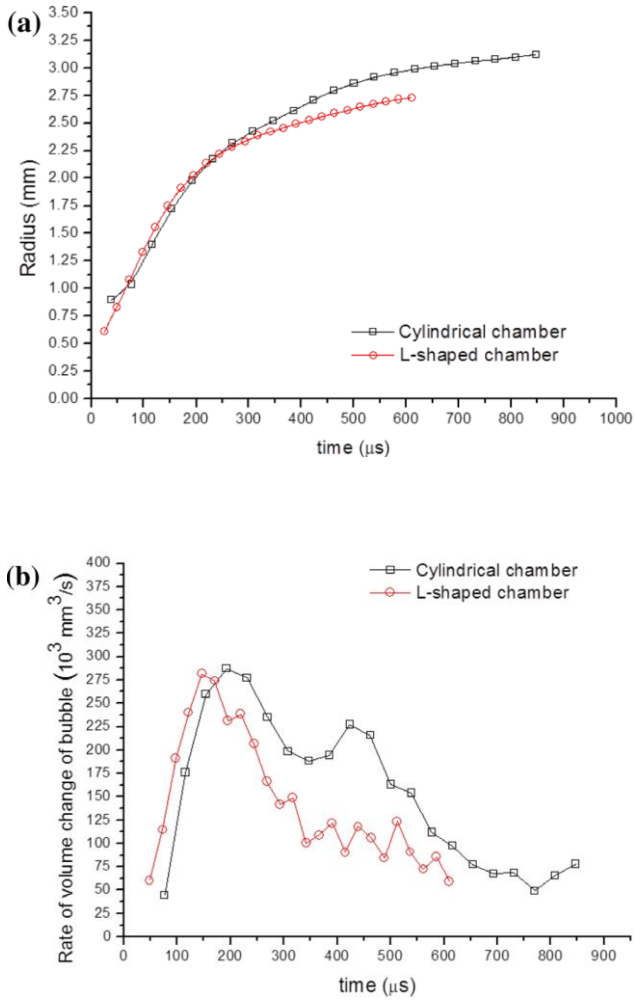

Fig. 4.16 Evolution of (a) radius and (b) rate of volume change of bubble with respect to time for cylindrical and L-shape chambers

The microjet of combined system penetrates relatively weak tissue structures because stratum corneum layer is effectively lifted before the injection follows. Nevertheless, the microjet characteristics such as atomization and jet velocity must be controlled as to ensure the maximum penetration efficiency. Figure 4.17 shows the velocity with the average errors 12%. The jet velocity of cylindrical chamber case is faster than that of the L-shape chamber because of the bubble motion as explained previously. However, the velocity of an L-shape chamber case is still fast enough to penetrate the skin and carries the substantial advantage from the compact design. In actual operation of the combined system, about 80% of the source energy is used for the microjet generation. Thus a relatively slower jet velocity is used for penetration, as shown from the volume-energy correlation in equation below [58]:

$$E_B = \frac{4}{3}\pi R_{\max}^3 P_\infty \sim E_L \tag{4.6}$$

Here, E_B is bubble potential energy, E_L is supplied laser energy, R_{max} is the maximum bubble radius, and P_∞ is the ambient pressure. The penetration depth is shown to be deeper than the microjet only case. One explanation for such observation is that when no ablation is used, most of the impact energy of the microjet is used toward overcoming the stratum corneum layer whereas in the combined case, the resulting microjet only targets the relatively softer tissue underneath the 'lifted' outer layer of skin.

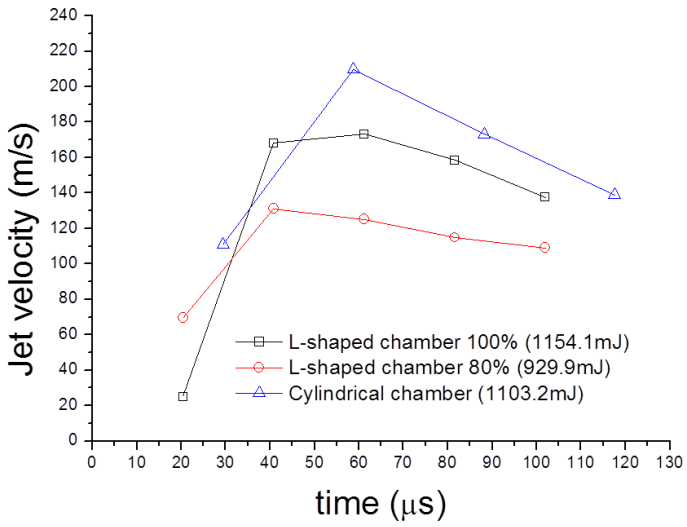

Fig. 4.17 Microjet velocity for L-shape chamber 80%, 100% energy, and cylindrical chamber

Synchronization is necessary to avoid potential adverse interaction between skin ablation and microjet injection. A cycle of pre-ablation of skin and subsequent microjet ejection is shown in Fig. 4.18(a). Some nano second time delays between the reflected beam and the transmitted beam exist caused by optical path differences as shown in Fig. 4.18(b). This delay can be ignored considering the order of each sequence.

The time delay in microjet generation should be larger than the laser pulse duration in order to minimize adverse interaction or collision between the beam and the jet. 150μs is for the pulse duration, and 167μs for time delay of microjet generation. The time delay for microjet generation is measured with the high-speed camera that records the delay between laser irradiation and

microjet ejection. The subsequent laser pulse cannot affect microjet ejection process because the laser is operated at 10Hz, which can be seen on the sequence diagram, Fig. 4.18(a). One finds that there is no negative effect from the combined approach because of the precisely controlled synchronization of pre-ablation and microjet generation.

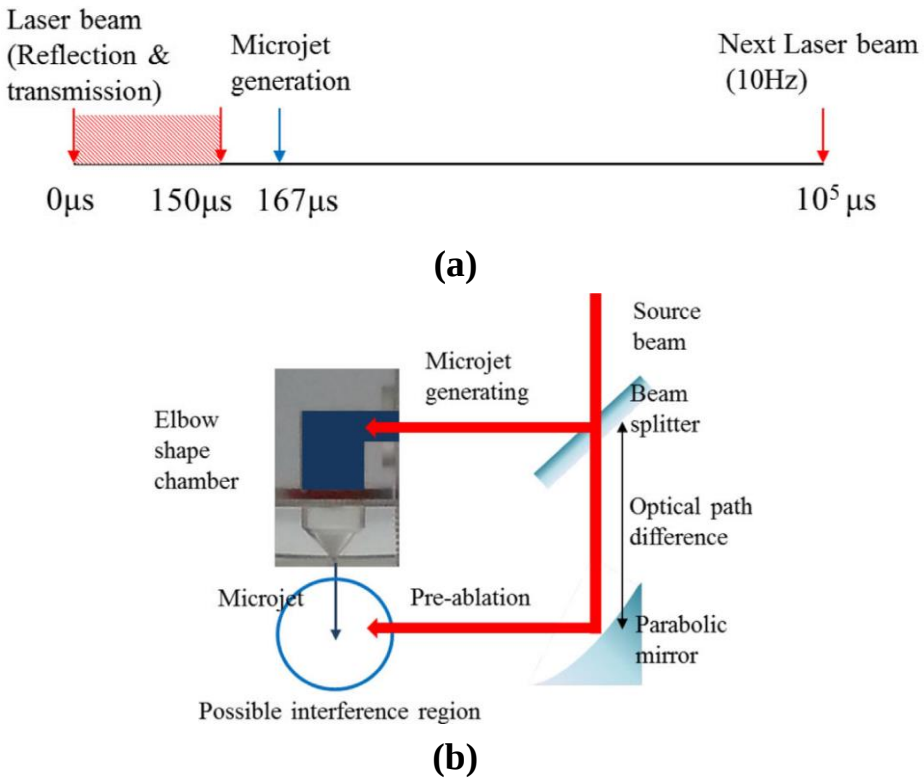

Fig. 4.18 Combined ablation and microjet injection system: (a) sequence diagram, and (b) overall schematic

The process of combined skin ablation and microjet injection is captured in Fig. 4.19 to demonstrate the suggested synchronization. First, the pre-

ablation beam irradiates the surface of 10% PAAG (Poly acrylamide gel), and bright light represents the interaction between the beam and the gel surface. Then, the microjet is ejected from the nozzle and no interaction or collision between the beam and the jet is observed. This is as intended.

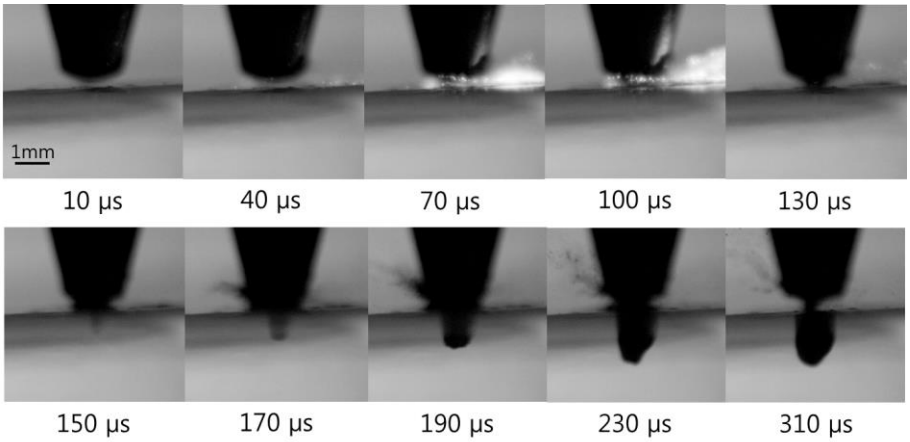

Fig. 4.19 Sequential images of pre-ablation and microjet injection into 10% PAAG

The Er:YAG laser in dentistry has a 250μs - 300μs pulse duration, which is not suitable for our system since the laser beam for ablation would still be present when the microjet ejection must occur – adverse interaction. To address this issue, a laser with a shorter pulse has been developed. Such shorter pulse (150 instead of 250μs) is suitable for both synchronization as well as strong microjet generation. Pulse duration effect on bubble expansion was investigated with the laser pulses ranging from 150μs to 300μs; each bubble was captured by the high speed camera as shown in Fig. 4.20.

Several researchers have investigated the effect of pulse duration on bubble formation using lasers in the mid infrared wavelength range, from 2μm to 3μm [59-61]. They observed that shorter pulses induced rapid bubble expansion; a similar trend was also observed in this study. Bubble pressure is proportional to growth rate [62]. Therefore, relatively short laser pulse can ensure faster microjet.

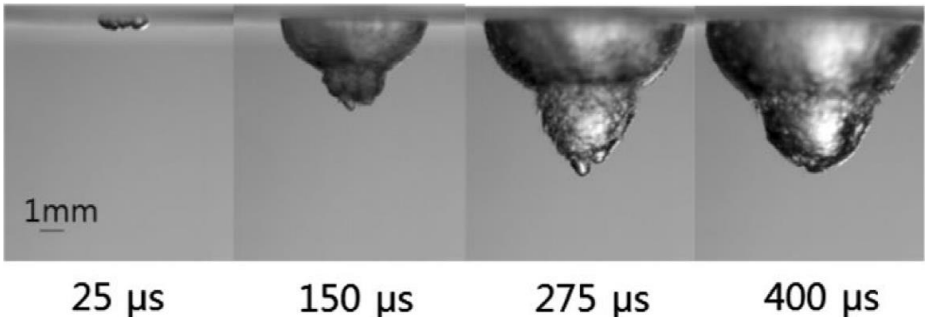

(a)

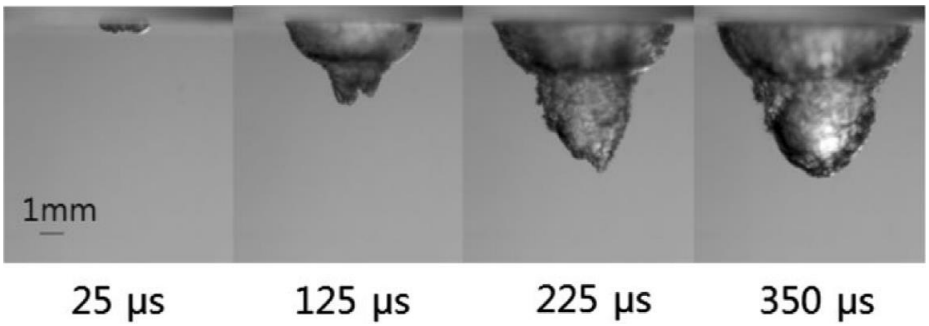

(b)

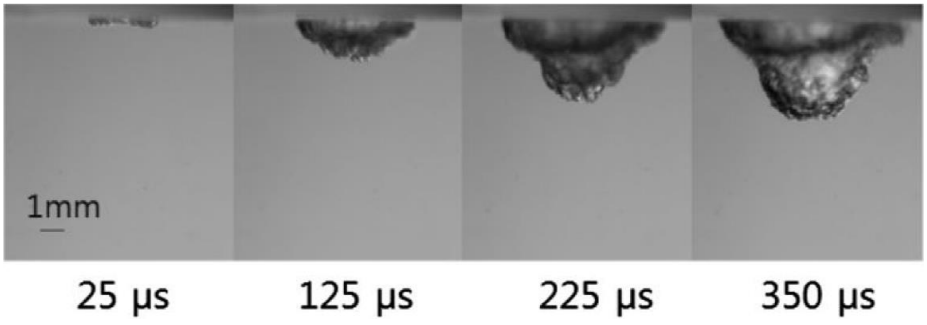

(c)

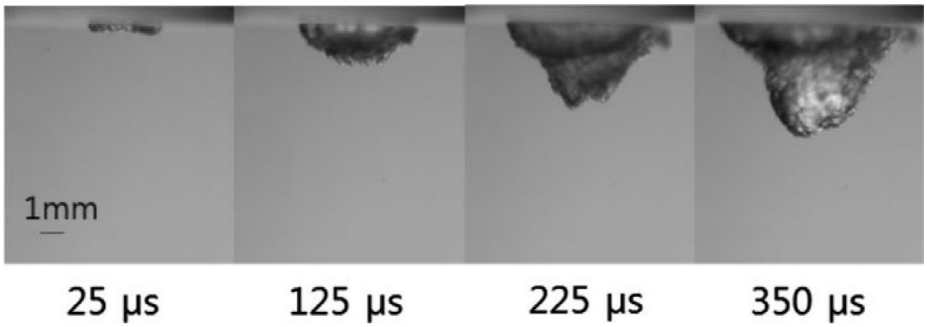

(d)

Fig. 4.20 Sequential images of bubbles generated by different pulse durations: (a) 150μs, (b) 200μs, (c) 250μs, (d) 300μs

The change in the bubble radius with respect to pulse duration is shown in Fig. 4.21. The maximum equivalent radius and growth rate are calculated in Table 1. Here, the aspect ratio is defined as diameter divided by height. If the bubble is elongated in the longitudinal direction, then the aspect ratio becomes smaller. The short pulse duration beams generate not only elongated bubbles but also bubbles that are larger and expand more rapidly. The growth rate is defined by the bubble radius at the end of the pulse. In

summary, a short-pulse Er:YAG laser is optimized for use in the synchronized skin ablation prior to efficient microjet injection for the trans-dermal drug delivery.

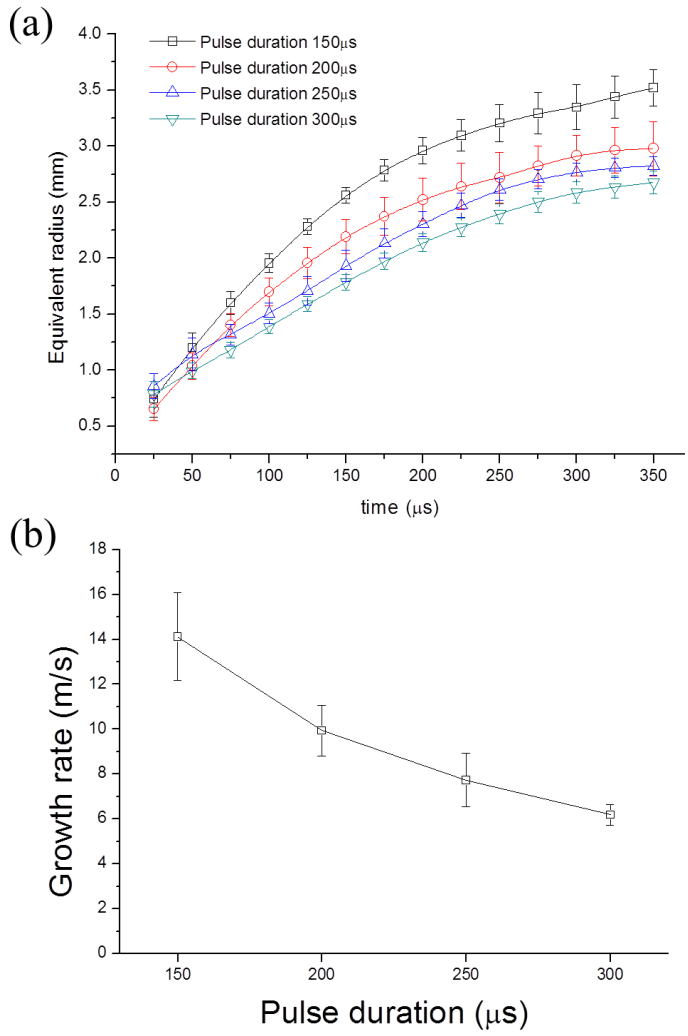

Fig. 4.21 (a) Equivalent radius with respect to time affected by laser pulse duration and (b) variation in growth rate depending on pulse duration

Table 4.4. Bubble characteristics determined by the pulse duration

Pulse duration (μs)	Initial irradiance (MW/cm^2)	Equivalent radius (mm)	Aspect ratio max diameter/ max height
150	0.614	3.46 ± 0.27	1.28
200	0.460	2.95 ± 0.21	1.22
250	0.368	2.82 ± 0.08	1.48
300	0.307	2.66 ± 0.10	1.59

Penetration experiments are carried out in order to compare drug transfer ability using the porcine skin. A single spot was repeatedly injected and penetration results were taken by the camera and microscopy. The injection is repeated 20-30 times at 10Hz. Top view images of the penetration results are presented in Fig. 4.22, showing much similarity.

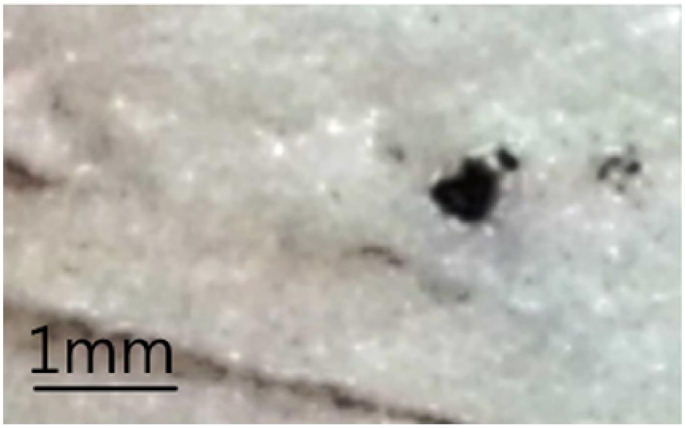

(a)

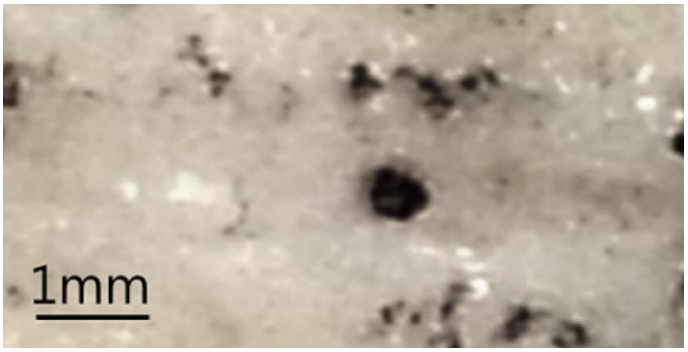

(b)

Fig. 4.22 Top view images of repetitive injection (single spot) in a porcine skin with black ink for (a) microjet only and (b) combined ablation and microjet

On the other hand, the side view images show difference between the two cases. For preparation of the post-processing images, the tissue samples were excised and fixed in a 10% formaldehyde solution. Then, the tissue specimens were embedded in paraffin and sliced into thin sections in a direction perpendicular to the skin surface and in the center of the point of injection. Finally, the sections were stained with H&E (hematoxylin-eosin) dye. Figure 4.23(a) shows the control group (untreated skin), 12(b) shows microjet only, and 4.23(c) shows combined ablation and microjet. For case (b), there is a small surface pit created by the jet impact and the penetration depth is 400 ± 28μm. Meanwhile, in the case (c) of combined ablation and microjet, a crater due to skin ablation has 184 ± 59μm depth, while the penetration depth is 613 ± 149μm. Clearly, the penetration depth of the

combined case is deeper, and thus the process of penetration is significantly enhanced via the combined strategy.

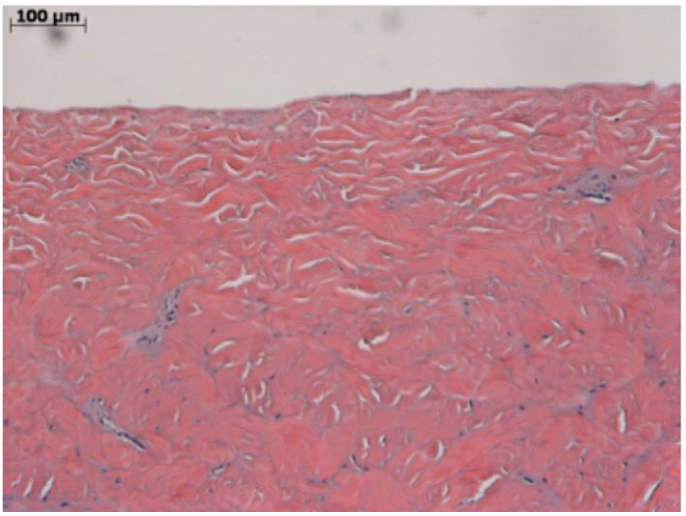

(a)

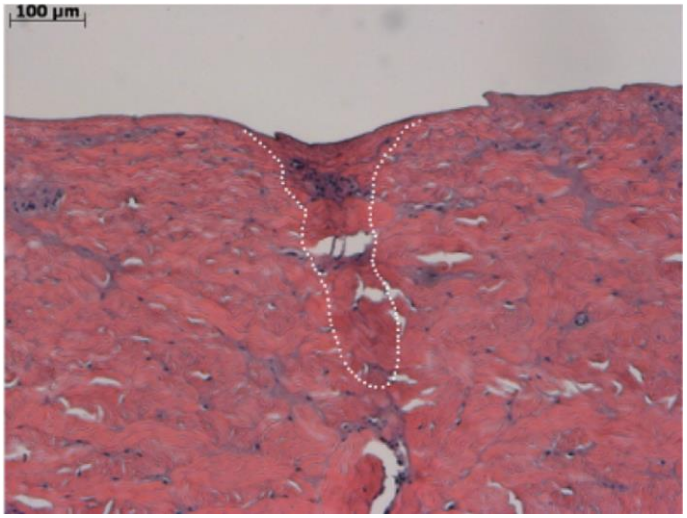

(b)

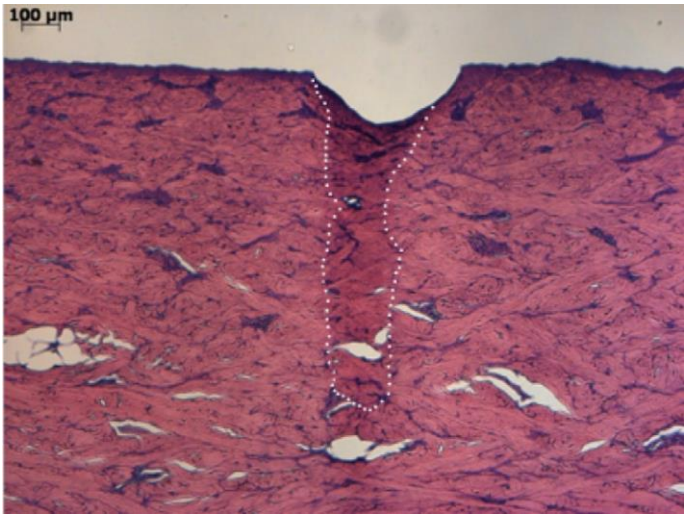

(c)

Fig. 4.23 Side view images of porcine skin for (a) No penetration, (b) microjet only, and (c) combined ablation and microjet

The porcine skin has a similar morphology and barrier as human skin and the thickness of the stratum corneum is about 20-30µm [56, 63]. The pre-ablated skin depth of 184µm is enough to eliminate the hardest layer, which was accomplished by the multiple pulses. The ablation rate per pulse can be estimated using equation (4.7), where t is removal thickness, F_0 is surface fluence and H_{abl} is heat of ablation [48].

$$t = F_0 / H_{abl} \tag{4.7}$$

The calculated removal thickness is 12.6µm using a heat ablation value of

1.75 kJ/cm^3, which is 70% that of water. Considering the number of repetitions, ablation measured depth per pulse (6.1μm -9.2μm) is less than the calculated value because ablation efficiency decreases when multiple pulses are applied [51].

The last penetration experiments consist of repetitive injections along a line instead of a dot. The number of repetitions for each dot was 10-20 but a long series of dots makes up a line on the skin. Penetration results are shown in Fig. 4.24 and the same methodology was used to obtain sectioned images. Here, penetration depth of combined ablation and microjet is also deeper than that when only a microjet was used, as shown in Fig. 4.24.

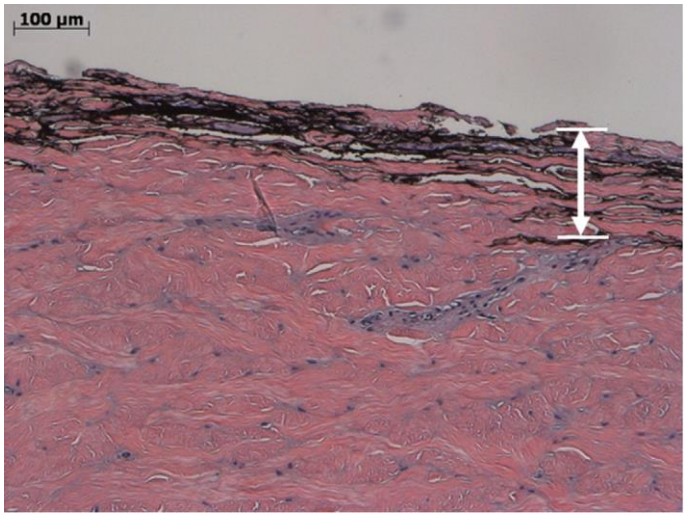

(a)

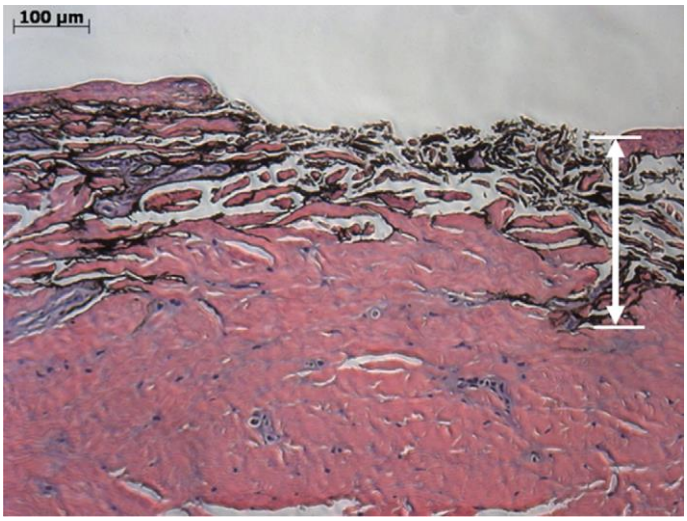

(b)

Fig. 4.24 Side view images of repetitive injection along a line of the porcine skin with black ink for (a) microjet only and (b) combined ablation and microjet

4.3 Deep Tissue Penetration Using Combined Pre-ablation and Microjet Injection Technique

4.3.1 Background and Motivation

Needle-free injection offers significant advantages when applied to macromolecule delivery including vaccines, insulin, local anesthetics, and growth hormones [64, 65]. The system is also known to overcome already acknowledged drawbacks to needle use such as site lesions, pain associated with the invasive procedure, disposal of medical waste, and safety issues

associated with reuse.

Previous efforts to develop needle free techniques include the application of a needless injector for insulin delivery through subcutaneous injections [66-69] requiring drug penetration depths of a few millimeters. Rapid insulin absorption is ensured with such non-invasive procedures, leading to efficient control of glucose level. However, there still remain many unresolved issues such as the potential for cross-contamination from the jet splash back, poor reliability regarding the delivered dose, and significantly painstaking procedures associated with the injection [16, 30, 70]. As an alternative, the use of microjets generated with Er:YAG lasers to deliver small doses per pulse at 10Hz with controlled penetration depths have been reported to be quite competitive with previously attempted methods [5, 27, 47].

Meanwhile, the SC or the topmost hard layer of the skin is the main obstacle to cutaneous injection. Especially, high-molecular-weight substances show low permeation into the skin. One possible way of overcoming the SC layer is skin ablation with mid infrared range lasers such as Er:YAG [48, 50, 51, 71]. For example, drug permeation can be enhanced by utilizing the laser, and the drug can be topically applied to the ablated skin surface [71-76].

Among the available options, fractional lasers allow efficient drug insertion through grid-patterned microholes. High-molecular-weight substances can be delivered into the deeper layer while skin damage is minimized by controlling the laser fluence, pulse number and exposure time. With fractional lasers, ablated holes surrounded by tissue are created, and full epidermal wounds are avoided with a suggested minimum healing time. The efficiency of drug

permeation can be increased further by using a rotation of the fractional laser because the density of microholes per unit area is significantly increased [76].

In this study, we successfully enhanced the injection depth via the combination of pre-ablation and microjet injection. First, skin is ablated with the Er:YAG laser and then, the microjet is injected through the pre-ablation site. In this manner, energetic microjets easily pierce the relatively weak strength layer. Here, three kinds of pre-ablation types are considered: bulk, fractional, and fractional–rotation. The pros and cons of each pre-ablation type are investigated to determine the optimal conditions for injection. Meanwhile, the parameters relative to microjet generation are fixed with reference to our previous optimal results: 150μs pulse duration, 1 J energy, 10Hz operated Er:YAG laser, 30° nozzle angle, and 150μm nozzle diameter.

4.3.2 Experimental Approach

The detailed mechanism is given in Figure 4.25(a). The outermost layer of the skin is subjected to elimination using the three types of pre-ablation. The mechanism for fast microjet generation is based on the laser-driven bubble expansion within a driving chamber separated by an elastic membrane between the drug and water. Two separate processes of pre-ablation and microjet generation are integrated into a single unit as shown in Figure 4.25(b). Each process shares a single laser source. In stage one, the laser beam passes through the ablation unit to pre-ablate the skin, and then the microjet

injector is connected to the laser. In the second stage, after eliminating the SC layer via pre-ablation, the ejected microjet penetrates the target skin with ease. A more elaborate discussion on the interaction between bubble and microjet can be found in the authors' earlier works [5, 27, 47]. The specification of the laser source used in the present study is as follows: Er:YAG (2940 nm, 150μs pulse duration, 1 J energy, and 10Hz operation frequency).

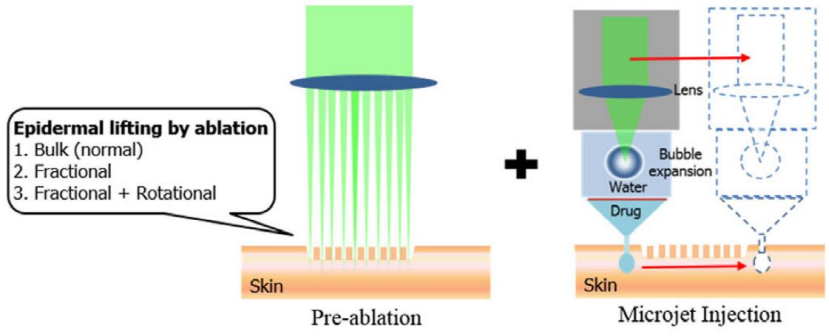

(a)

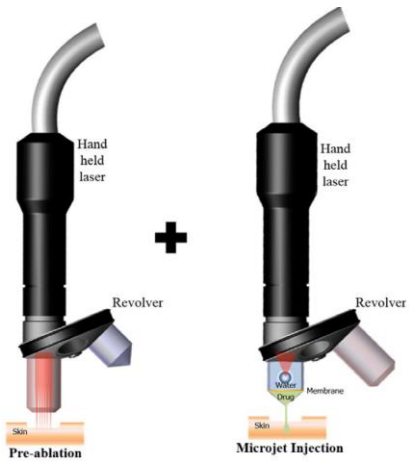

(b)

Fig. 4.25 (a) Two stage procedure of pre-ablation followed by microjet injection, and (b) a compact combined system using a dual function revolver.

The ablation parameters of the mid-infrared-range laser are shown in Table 4.5. The optimal fluence of pre-ablation is determined to be 8 J/cm^2, based on previous studies. The goal of pre-ablation is the elimination of the SC, which is a barrier against substance permeation from the outside of the skin. This process can enhance microjet permeation into the skin. In this study, pig skin is selected for quantification of the injection depth based on the two stage procedure, namely pre-ablation and microjet injection into the treatment site.

Table 4.5. Ablation data for the mid-infrared-range beam: pulse duration, energy, ablation rate and ablated diameter

	Laser	Pulse duration	Target	Energy	Ablation rate	Ablated diameter
Our system (bulk)	Er:YAG	150 μs	Pig skin	8 J/cm^2	13 – 15.6 μm (per pulse)	4029 μm
Our system (fractional)	Er:YAG	150 μs	Pig skin	8 J/cm^2	6.7 – 11.4 μm (per pulse)	244 μm
Hibst [50]	Er:YAG	250 μs	Pig skin	10 - 73 J/cm^2	18 – 414 μm (per pulse)	900 μm
Walsh [48]	Er:YAG	250 μs	Guinea Pig skin	5.4 - 72.5 J/cm^2	8.4 - 400 μm (per pulse)	1100 μm
Hohenleutner [51]	Er:YAG	250 μs	Human Skin	1.6 - 7 J/cm^2	1.75 – 15.3 μm (per pulse)	3000 μm
Khatri [71]	Er:YAG	250, 350, 700 μs	Human Skin	5 J/cm^2	3.3 – 6.7 μm (per pulse)	5000 μm
Lee [72]	Er:YAG	100 μs	Nude mice	2.5 – 5 J/cm^2	10 - 20 μm (per pulse)	120 μm
Nelson	Er:YSGG	250 μs	Pig skin	1 J/cm^2	2.2 μm	2000 μm

[73]					(per pulse)	
Hædersdal [74]	Fractional CO^2	3 ms	Pig skin	130 J/cm^2	1850 μm (total)	300 μm
Genina [75]	Fractional Er:YAG	200 μs	Human Skin	0.5 – 3 J	150 – 300 μm (total)	160 μm
Dierckx [71]	Fractional Er:YAG	250 μs	Pig skin	60 J/cm^2	170 μm (per pulse)	50 μm

Three kinds of pre-ablation are devised, consisting of (a) bulk ablation; (b) fractional ablation; and (c) fractional–rotational ablation. A top view image of ablation patterns is shown in Figure 4.26. The number of laser pulses are 12, 18, and 24, and this value is the same for all of the three ablation types compared. The idea behind the (c) fractional–rotational case is a subtle enhancement of the concept suggested by Lee et al.[76], and the fractional laser is rotated by 11.25° at each pulse for optimal elimination of the topmost layer. The ablation efficiency is quantified by the ablation depth and the mass removal. The ablation depth is measured from the cross sectional images of pre-ablation skin, while the mass removal is quantified by the weight change of the sampled skin due to a pre-ablation procedure.

Meanwhile, the microjet dispersion pattern of the inner skin can be confirmed by using a tissue marking dye (blue color, Polysciences, Inc.). The injector liquid is mixed with dye and ejected in the form of a microjet. Here, the average jet velocity is about 130 m/s, which is enough to penetrate the toughest outermost layer of porcine skin. Then the stained skin is carefully sectioned with a razor blade. The cross sectional view of a skin is imaged with

a Nikon camera.

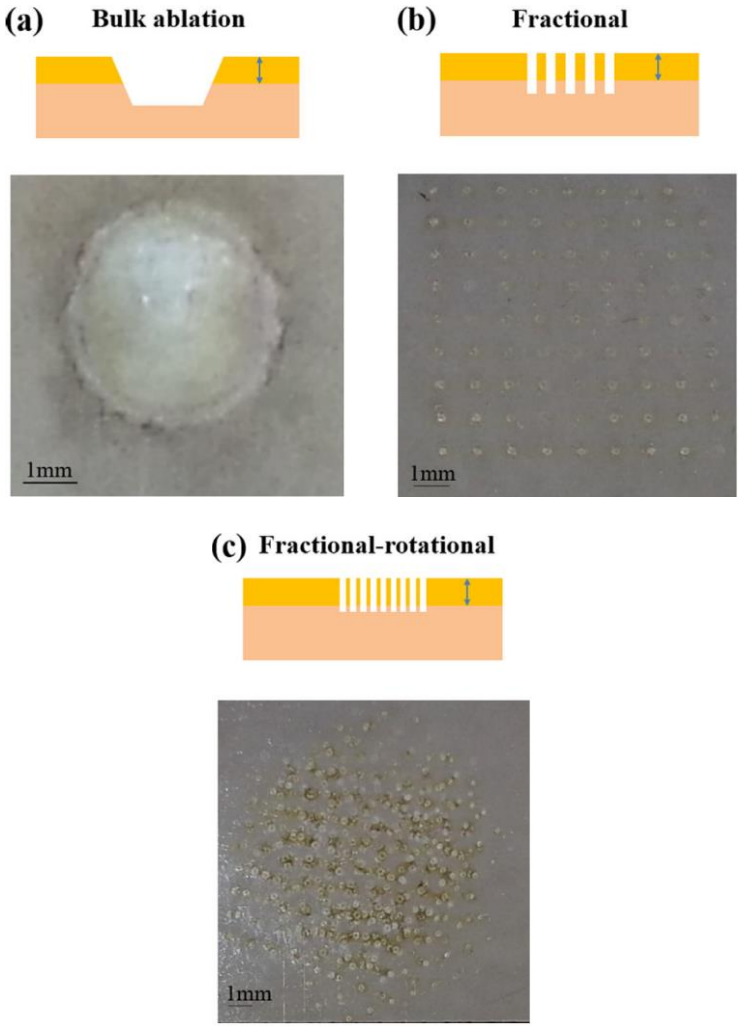

Fig. 4.26 Top view of burn pattern for each ablation type: (a) Type 1 bulk ablation, (b) Type 2 fractional ablation, and (c) Type 3 fractional–rotational ablation

The benefits of a pre-ablation procedure prior to actual microjet injection to the penetration outcome is examined by comparing the depth of ablation via three types of pre-ablation and the depth of penetration via microjet injections. There are three types of pre-ablation schemes that are considered, namely bulk ablation, fractional ablation, and combined fractional–rotational ablation, all of which are commonly practiced by dermatologists. A typical cross sectional view of a pre-ablated pig skin is shown in Figure 4.27 with 12, 18, and 24 laser pulses.

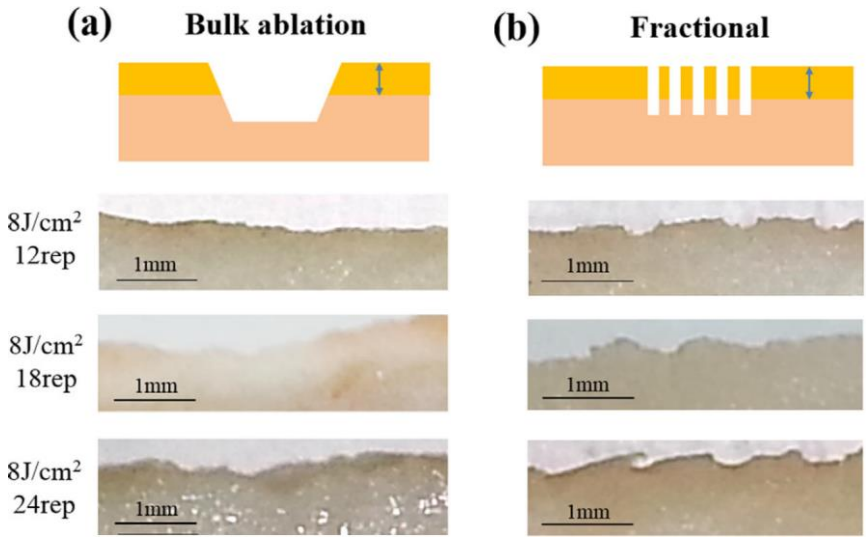

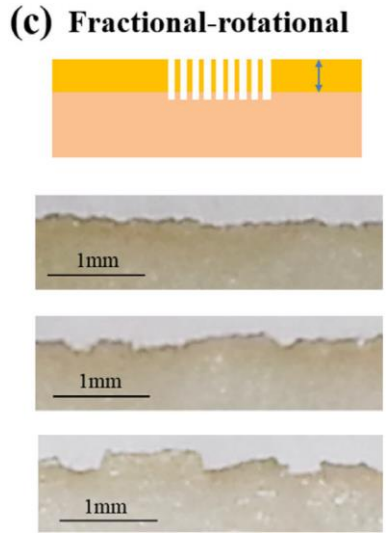

Fig. 4.27 Cross sectional view of pre-ablation by type, shown with increasing pulse repetition: (a) Type 1 bulk ablation, (b) Type 2 fractional ablation, and (c) Type 3 fractional–rotational ablation

4.3.3 Results and Discussion

The benefits of a pre-ablation procedure prior to actual microjet injection to the penetration outcome is examined by comparing the depth of ablation via three types of pre-ablation and the depth of penetration via microjet injections. There are three types of pre-ablation schemes that are considered, namely bulk ablation, fractional ablation, and combined fractional–rotational ablation, all of which are commonly practiced by dermatologists. A typical cross sectional view of a pre-ablated pig skin is shown in Figure 4.27 with 12, 18,

and 24 laser pulses.

For bulk ablation, the ablated area is relatively large in comparison to the nozzle diameter. This suggests that there is no alignment issue associated with missing a target, as high drug delivery efficiency is achievable for every single injection administered. However, recovery will be quite slow since the damaged area is extended for the bulk target. Using a different style, the outermost skin layer can be eliminated with minimal skin damage with the application of fractional ablation. Here, numerous micro-holes can efficiently assist drug transport, but they pose an alignment issue regarding hitting the ablated hole with the microjet from a nozzle. Nevertheless, healing time is minimized because full epidermal wounds are avoided by the generation of many micro-holes as opposed to bulk ablation of the target site. As for the third type of pre-ablation, fractional–rotational ablation incorporates the benefits of these two methods, which include both short healing time and a highly effective procedure. As the number of micro holes in the unit area for fractional–rotational ablation is higher than for fractional ablation, the penetration depth for the fractional–rotational type is also shallower due to the rotational effect of the beam. This is a favorable condition for increasing the precision to align the impact position of the microjet as well as for ensuring fast recovery of the ablative wounds in comparison to the bulk type method described above.

The efficiency of each ablation type is evaluated using the ablation depth and removed mass with the same laser fluence of 8 J/cm2. Ablation depths are shown in Figures 4.28 and 4.29. The result from a type 1 ablation (bulk) is the

highest among the types shown in Figure 4.29(a) and (b). However, the total ablation depth is proportional to the laser pulse repetition for all types. In particular, ablation depth per pulse decreases with an increasing number of repetitions because of thermal coagulation. Although the three ablation types showed different ablation efficiency, all three procedures are effective in the elimination of the top most layer of a porcine skin.

Another parameter that can be used as a measure of pre-ablating the skin is the total mass of removal as shown in Figure 4.29(a) and (b). The mass removed per pulse decreased with the increase in the number of repetitions, showing a similar trend as the ablation depth. Interestingly, the mass removed from type 3 (fraction-rotational) ablation is larger than type 1 and type 2, due to the effect of thermal coagulation. The Er:YAG laser is an efficient tool for skin ablation due to its absorptivity in water. Repetitive laser pulses in the same spot accelerate dehydration of the skin, which results in the reduction of ablation efficiency. However, in type 3 (fractional–rotational) ablation, the targeted spot is naturally varied due to rotation and the thermal coagulation effect is minimized, which results in the most effective skin ablation among all the skin ablation types studied.

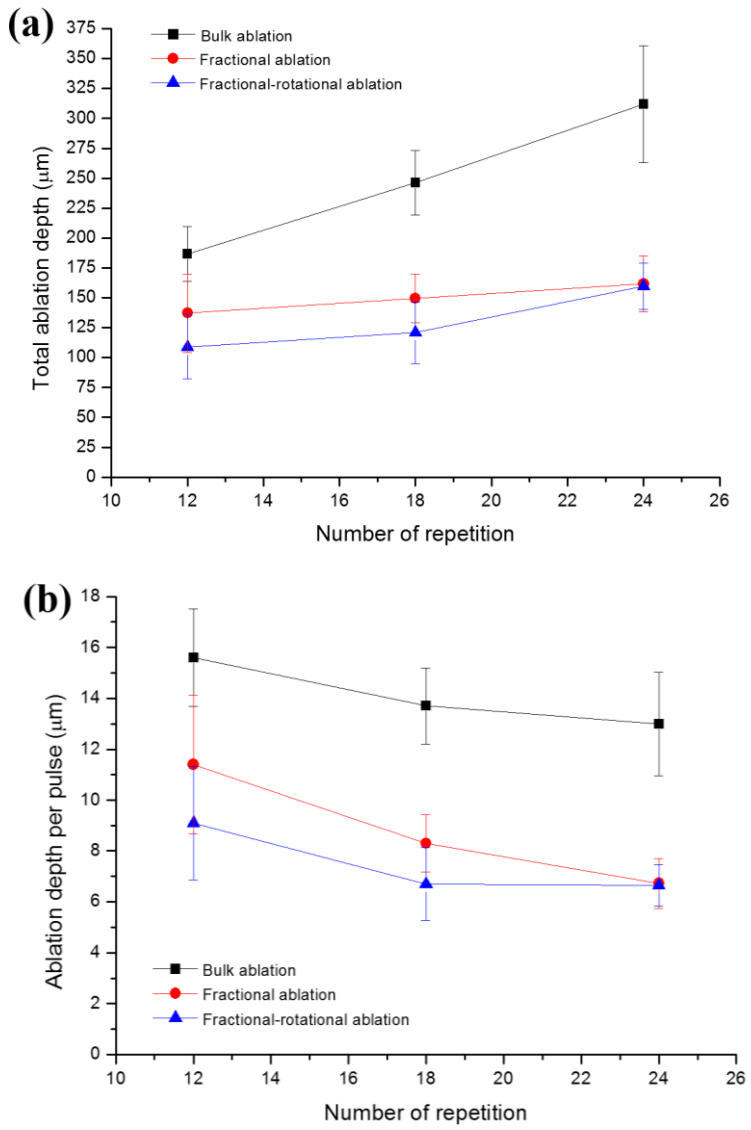

Fig. 4.28 Ablation efficiency compared for each pre-ablation type based on (a) total ablation depth and (b) ablation depth per pulse. The fluence is the same at 8 J/cm2 for all cases.

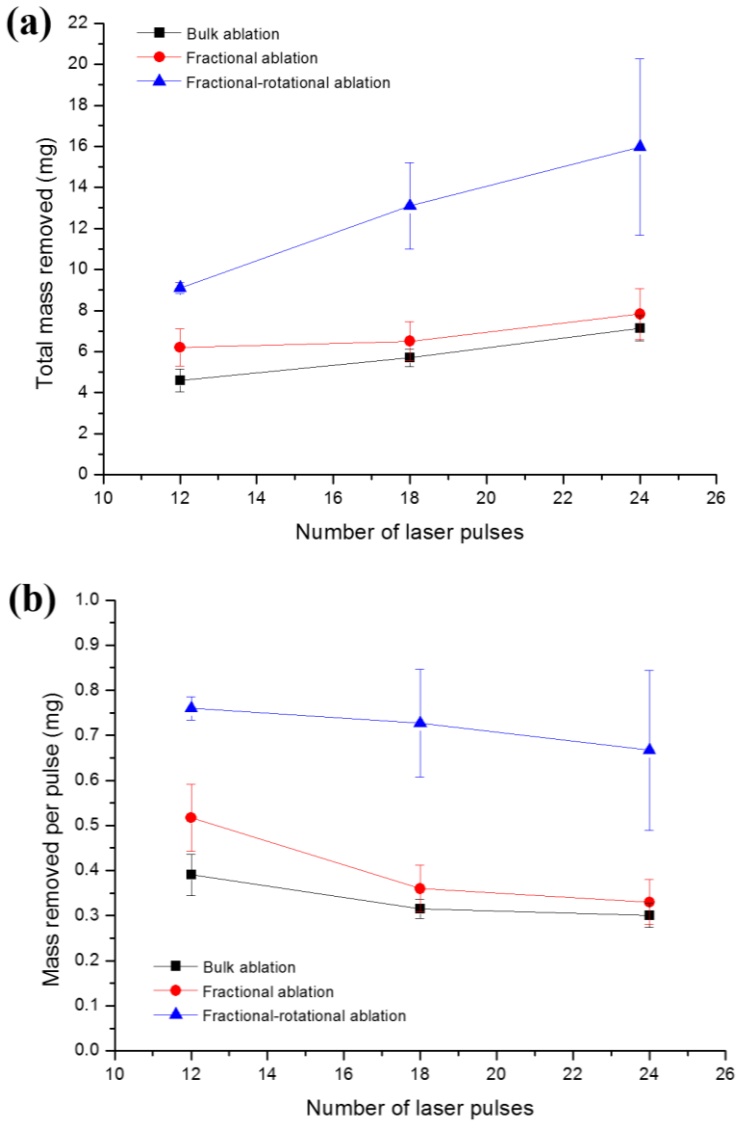

Fig. 4.29 Ablation efficiency compared for each pre-ablation type by (a) total mass removed and (b) mass removed per pulse. The fluence is the same at 8 J/cm2 for all cases.

The injection time is one key factor in drug delivery. In Figure 4.30 showing the microjet only result, the penetration depth of injection is illustrated by tracing the tissue marking dye in blue. It is clear that the depth becomes deeper with increasing injection time, and the amount of delivered doses also increases with the number of injections.

The cross sectional view of the porcine skin test in Figure 4.30 is further analyzed as shown in Figure 4.31. First, pre-ablation is responsible for enhancing the penetration depth. The penetration depth of bulk ablation (12 pulses) and microjet is increased by 12 ~ 14 % and that of bulk ablation (18 pulses) and microjet is increased by 11 ~ 42 % when compared to the microjet only case. These results indicate that the number of ablation pulses does not have a huge impact on penetration depth once the toughest outermost skin layer is removed.

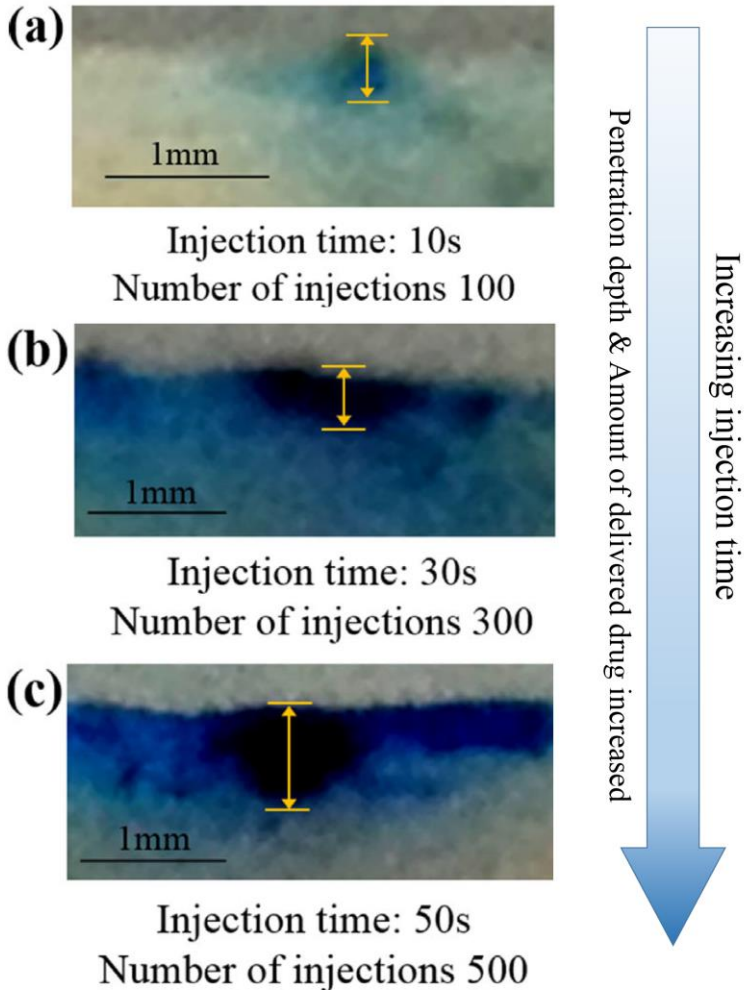

Fig. 4.30 Cross sectional view of a single spot with indicated number of injections (or time) for blue dye: (a) 100 injections, (b) 300 injections, and (c) 500 injections

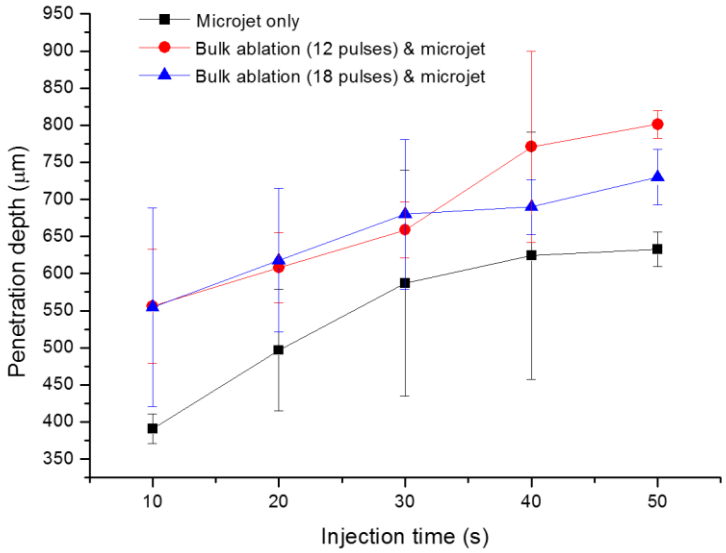

Fig. 4.31 Penetration depth per injection time compared for microjet only, bulk ablation and microjet, fractional ablation and microjet, and fractional–rotational ablation and microjet. For all pre-ablation types, 18 reps of laser pulses and 8 J/cm2 are used.

A comparison of all possible combinations of microjet injection is given in Figure 4.32. The four combinations are (a) microjet only; (b) bulk ablation and microjet injection; (c) fractional ablation and microjet injection; and (d) fractional–rotational ablation and microjet injection. The dispersion of marking dye (blue) as well as some ablative surface patterns are visible in the figure. The quantification of the total penetration depth is shown in Figure 4.33. Here, total penetration depth includes both SC ablation and microjet injection depths. Accordingly, the depth increases with injection time for all cases. In particular, the depth of penetration attained via fractional pre-

ablation increased by 8 ~ 11 % and that of fractional–rotational pre-ablation increased by 13 ~ 33 %, when compared with the no pre-ablation or microjet only case.

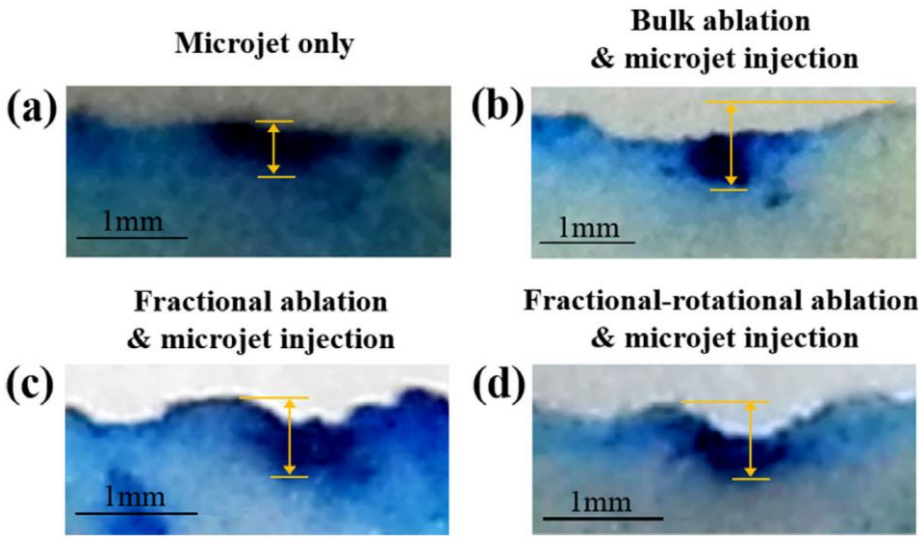

Fig. 4.32 Cross sectional view of a single spot with 300 injections and 18 pre-ablation pulses for (a) microjet only, (b) bulk ablation and microjet, (c) fractional ablation and microjet, and (d) fractional–rotational ablation and microjet.

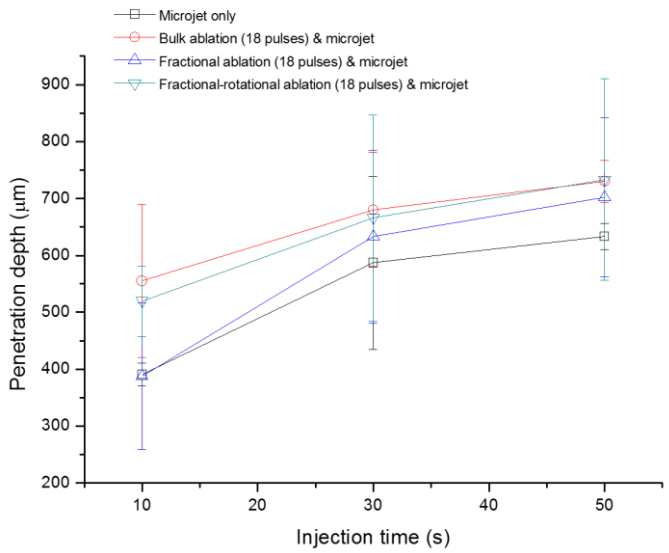

Fig. 4.33 Penetration depth per injection time compared for microjet only, bulk ablation and microjet, fractional ablation and microjet, and fractional–rotational ablation and microjet. For all pre-ablation types, 18 reps of laser pulses and 8 J/cm2 are used.

The penetration depth underneath ablated SC is also measured in order to verify the pre-ablation effect. The penetration depths for each case are (a) 443 ± 104 μm; (b) 625 ± 98 μm; (c) 523 ± 95 μm; and (d) 595 ± 141 μm for (a) microjet only; (b) bulk ablation and microjet; (c) fractional ablation and microjet; and (d) fractional–rotational ablation and microjet, respectively. A noticeable point is that the fraction-rotational pre-ablation and microjet result is comparable to the bulk ablation and microjet result. This is quite beneficial since any healing time associated with ablation is significantly reduced by

avoiding hard-core bulk ablation.

As for the non-single spot test, 500 microjet injections are administered at each spot and a total of 10 spots are considered to verify the possibility of controlling the dosage. The between-the-spot distance is set at 200 μm. Here, higher density of micro-holes can enhance the chance of microjet hitting the holes. Shown in Figure 4.34, the depth of penetration is deeper for cases with a pre-ablation scheme. Presumably, the most effective combination, bulk pre-ablation and microjet, may well be superseded by the less invasive fractional–rotational ablation followed by the microjet injection. fractional–rotational ablation and microjet injection is more efficient since number of micro-holes in a unit area is increased in comparison to fractional ablation and microjet case. Here, the density of micro-holes is 1.27 number/mm^2 for fractional ablation and 4.84number/mm^2 for fractional–rotational ablation. Consequently, the penetration depths measured underneath the ablated SC are 581μm (fractional ablation and microjet case) and 691μm (fractional–rotational ablation and microjet case). Table 4.6 shows the increased chance of microjet hitting the ablated micro-holes from approximately 4% to 20%.

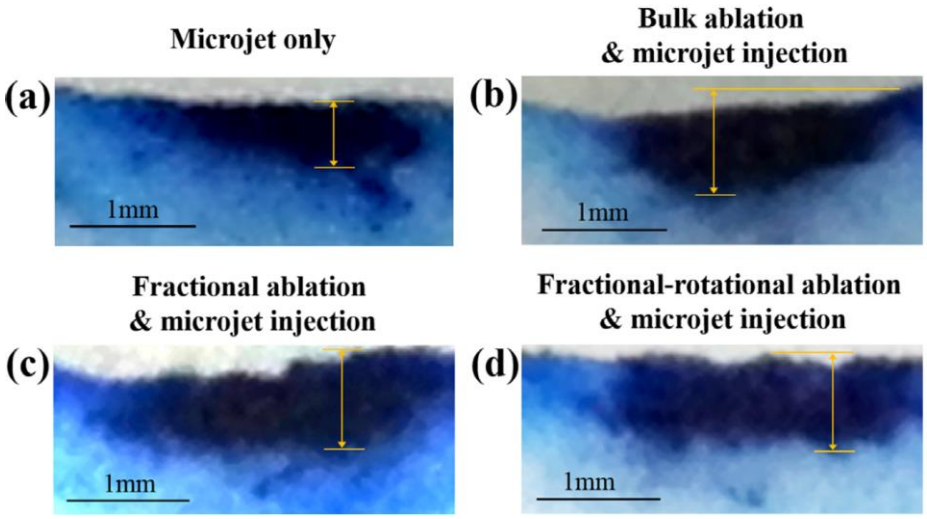

Fig. 4.34 Cross sectional view of the multi-spots (10 spots) at 500 injections per spot and 18 pre-ablation pulses for (a) microjet only, (b) bulk ablation and microjet, (c) fractional ablation and microjet, and (d) fractional–rotational ablation and microjet.

Table 4.6. Relation between density of micro-holes and drug delivery efficiency

Ablation type	**Density of micro-holes (number/mm^2)**	**% Ratio of ablated holes to target area**	**Penetration depth(μm)**
Fractional	1.27	3.97	581
Fractional-rotational	4.84	19.35	691

Chapter 5. Conclusions

Experimental analysis were carried out to analyze interaction between laser and matters. For example, laser ablation in liquid is related with laser driven bubble and efficient laser assisted drug delivery is possible by understanding skin ablation phenomena. Liquid jet impact into skin was also investigated to figure out microjet penetration process. A diagnostic using a high speed camera was conducted to investigate the performance of microjet injector. The capability of present delivery system is also evaluated by the animal skin test. The specific findings and conclusions are summarized as follows.

(1) The impact of wavelength and pulse duration on the bubble dynamics and the performance of the laser-induced microjet injector was investigated. For Nd:YAG laser, the pulse duration is very short (nanoseconds) relative to the bubble lifetime making the behavior of the bubble close to that of cavitation bubble, while in Er:YAG case, the high absorption in the water and long pulse duration in few microseconds change the initial behavior of the bubble making it resembling a vapor bubble. The contraction and subsequent rebound are typical for cavitation bubbles in both cases.

The results show that the laser-induced microjet injector generates velocity which is sufficient for the drug delivery. We estimate the typical velocity within 30–80 m/s range and the breakup length to be larger than 1 mm. The range of the breakup length defines the maximal

standoff distance if a biomedical injector is to be applied properly. The present study makes important contribution to understanding of the jet-driving mechanism of the laser-induced microjet devices which has been tested successful for transdermal drug delivery in animal tests.

(2) This study evaluates the performance of a laser-induced microjet in delivering FITC and biotin (as drug substitutes) into a guinea pig's abdominal skin sample. Success in biotin staining demonstrates that the drug is delivered across the guinea pig skin and the delivered drug is not damaged. The rubber membrane between the drug and driving chamber prevents any thermal effects on the drug during the optical breakdown. Thus, one can be assured that the laser-based method achieves micro-jet injection across the guinea pig skin, and expect the delivered drug to act efficiently under the skin.

The present delivery technique will not replace the needle–syringe systems for common injections, such as flu shots. However, the laser-based approach is a novel and promising concept for future drug delivery where precision and painless injections are sought. With controllable depth of penetration, the present scheme of delivery using fast and narrow micro-jets induced by a laser pulse seems to be promising for transdermal injection of a drug solution and easily repeatable, thus making it ideal as a non-intrusive means of small-dose injection in such applications as skin esthetic treatments.

(3) The performance of an Er:YAG laser initiated microjet is evaluated for transdermal drug delivery. Approximately 500 nl per pulse of drug is delivered beyond the skin barrier in the form of a microjet as the injected drugs are effectively dispersed over the epidermis. We ensured controllability of the laser-initiated microjets via the longer pulse (250 μs) at lower energy (<1.57 J), which is an improvement from the Nd:YAG based injection scheme delivering 200 nl per pulse.

(4) Jet characteristics and injector parameters are analyzed in order to establish the optimal conditions of a laser-based microjet system. A use of a step motor allowed continuous refilling of drug reservoir and uniform ejections of the repetitive microjets. Then the drug delivery is confirmed by making sure that there is no thermal damage done to the dosed drugs (two kinds of human growth hormones tested) during and after the microjet injection into a porcine skin. In conclusion, this work contributes to the controlling of jet characteristics and safety assurance of the delivered drug, particularly aimed at general clinical use of the system in the near future.

(5) Bubble and membrane motions in confined condition are analyzed. Combination effect of beam spot size and cylinder height are studied to describe actual bubble behavior inside of injector. Bubble shape such as aspect ratio is determined by initial beam spot size. Small beam spot size makes elongated bubble shape because of high

irradiance of initial beam spot. Chamber wall impedes bubble expansion resulting more sustainable bubble. It is also observed that membrane responses well to bubble motion with certain delay time. Jet velocity which is a criterion for effective drug delivery is measured to suggest optimum condition for microjet generation. In current study, it is clearly seen that both volume growth rate of bubble and membrane are closely related with jet speed.

(6) Two different microjet injection schemes are considered. For Microjet Only case, the focused Er:YAG beam at 150 μs pulse duration generates strong vapor bubble inside the driving water chamber, which is responsible for ejecting a fast microjet of the intended drug solution. The efficiency of drug penetration into a porcine skin or PAAG depends on the kinetic energy of the microjet. As for Pre-ablation Microjet case, the same laser beam is split as such 20% of the source is used to ablate a tiny spot on a skin before the remaining 80% energy driven microjet arrives at the pre-ablated spot for an enhanced drug penetration. Both the kinetic energy of microjet and the condition of the ablated skin are responsible for the noted enhancements.

(7) The Er:YAG laser has a high absorption coefficient in water, which is suitable for generating vapor bubbles. The same laser at a pulse duration of 150 us is capable of ablating the outer most layer of the skin in the present set up for the pre-ablation and microjet injection. The

synchronization of skin ablation beam and subsequent microjet injection is demonstrated, which eliminates potential adverse interactions between the two. The success of the combined strategy is demonstrated through the sectioned images of the treated porcine skins.

(8) A two stage procedure for laser-assisted microjet injection for transdermal drug delivery is described. The Er:YAG laser is selected as a beam source for both pre-ablation of the treatment site and subsequent microjet ejection as it has the highest absorption coefficient in water for its wavelength. Three types of pre-ablation are considered, namely bulk ablation, fractional ablation, and fractional–rotational ablation, prior to administering the laser-assisted microjet injection. In order to meet dual goals, namely efficient drug injection as well as fast recovery, type 3 pre-ablation combined with microjet is chosen, with excellent feasibility. Because type 3 pre-ablation increases the number of micro holes in a unit area, which is related to penetration efficiency. Type 3 pre-ablation also has advantage of fast recovery due to minimized tissue damage near micro-holes. Furthermore, the present system has the potential for use in macromolecule delivery systems, including vaccines, growth hormones, and insulin in the near future.

In conclusion, all aspects of the system including laser parameters effects on bubble growth and microjet generation, skin penetration aspects, repetitive and reliable microjet generation, bubble expansion in confined codition, laser-

assisted drug delivery system have been discussed. The reported results provide a design guideline to build a reliable and functionally optimized non-invasive transdermal drug delivery system based on laser-generated microjet.

References

[1] Kendall, M.A., Needle-free vaccine injection, in Drug Delivery. 2010, Springer. p. 193-219.

[2] Prausnitz, M.R. and R. Langer, Transdermal drug delivery. Nature biotechnology, 2008. 26(11): p. 1261-1268.

[3] Mitragotri, S., Current status and future prospects of needle-free liquid jet injectors. Nature Reviews Drug Discovery, 2006. 5(7): p. 543-548.

[4] Fletcher, D. and D. Palanker, Pulsed liquid microjet for microsurgery. Applied Physics Letters, 2001. 78(13): p. 1933-1935.

[5] Park, M.-a., et al., Er: YAG laser pulse for small-dose splashback-free microjet transdermal drug delivery. Optics letters, 2012. 37(18): p. 3894-3896.

[6] Han, T.-h. and J.J. Yoh, A laser based reusable microjet injector for transdermal drug delivery. Journal of Applied Physics, 2010. 107(10): p. 103110.

[7] Akhatov, I., et al., Collapse and rebound of a laser-induced cavitation bubble. Physics of Fluids, 2001. 13(10): p. 2805-2819.

[8] Vogel, A., S. Busch, and U. Parlitz, Shock wave emission and cavitation bubble generation by picosecond and nanosecond optical breakdown in water. The Journal of the Acoustical Society of America, 1996. 100(1): p. 148-165.

[9] Noack, J., et al., Influence of pulse duration on mechanical effects after

laser-induced breakdown in water. Journal of Applied Physics, 1998. 83(12): p. 7488-7495.

[10] Hale, G.M. and M.R. Querry, Optical constants of water in the 200-nm to 200-μm wavelength region. Applied optics, 1973. 12(3): p. 555-563.

[11] Barnes, P.A., Studies of laser induced breakdown phenomena in liquid water. 1969, Simon Fraser University. Theses (Dept. of Physics).

[12] Plesset, M.S. and A. Prosperetti, Bubble dynamics and cavitation. Annual review of fluid mechanics, 1977. 9(1): p. 145-185.

[13] Mitragotri, S., Immunization without needles. Nature Reviews Immunology, 2005. 5(12): p. 905-916.

[14] Kendall, M.A., Y.-F. Chong, and A. Cock, The mechanical properties of the skin epidermis in relation to targeted gene and drug delivery. Biomaterials, 2007. 28(33): p. 4968-4977.

[15] Brown, M.B., et al., Dermal and transdermal drug delivery systems: current and future prospects. Drug delivery, 2006. 13(3): p. 175-187.

[16] Arora, A., et al., Needle-free delivery of macromolecules across the skin by nanoliter-volume pulsed microjets. Proceedings of the National Academy of Sciences, 2007. 104(11): p. 4255-4260.

[17] Doukas, A.G. and N. Kollias, Transdermal drug delivery with a pressure wave. Advanced drug delivery Reviews, 2004. 56(5): p. 559-579.

[18] Sarno, M.J., et al., Clinical immunogenicity of measles, mumps and rubella vaccine delivered by the Injex jet injector: comparison with standard syringe injection. The Pediatric infectious disease journal, 2000. 19(9): p. 839-842.

[19] Han, T.-h., J.-m. Hah, and J.J. Yoh, Drug injection into fat tissue with a laser based microjet injector. Journal of Applied Physics, 2011. 109(9): p. 093105.

[20] Cavitation, C.B., bubble dynamics [M]. 1995, Oxford University Press, New York.

[21] Dumouchel, C., On the experimental investigation on primary atomization of liquid streams. Experiments in fluids, 2008. 45(3): p. 371-422.

[22] Arora, A., M.R. Prausnitz, and S. Mitragotri, Micro-scale devices for transdermal drug delivery. International journal of pharmaceutics, 2008. 364(2): p. 227-236.

[23] Taberner, A., N.C. Hogan, and I.W. Hunter, Needle-free jet injection using real-time controlled linear Lorentz-force actuators. Medical engineering & physics, 2012. 34(9): p. 1228-1235.

[24] Lefebvre, A.H., Atomization and Sprays, Hemisphere Pub. Corp., New York, 1989. 1989.

[25] Segre, J.A., Epidermal barrier formation and recovery in skin disorders. The Journal of clinical investigation, 2006. 116(5): p. 1150-1158.

[26] Menezes, V., S. Kumar, and K. Takayama, Shock wave driven liquid microjets for drug delivery. 2009, AIP.

[27] Jang, H.-j., et al., Laser-induced microjet: wavelength and pulse duration effects on bubble and jet generation for drug injection. Applied Physics B, 2013. 113(3): p. 417-421.

[28] Maximum recommended Therapeutic Dose (MRTD) database. U.S.

Food and Drug Administration, http://www.fda.gov.

[29] Lambert, P.H. and P.E. Laurent, Intradermal vaccine delivery: will new delivery systems transform vaccine administration? Vaccine, 2008. 26(26): p. 3197-3208.

[30] Theintz, G. and P. Sizonenko, Risks of jet injection of insulin in children. European journal of pediatrics, 1991. 150(8): p. 554-556.

[31] Gibson, D. and J.R. Blake, The growth and collapse of bubbles near deformable surfaces. Applied Scientific Research, 1982. 38(1): p. 215-224.

[32] Blake, J.R. and D. Gibson, Cavitation bubbles near boundaries. Annual review of fluid mechanics, 1987. 19(1): p. 99-123.

[33] Tomita, Y. and T. Kodama, Interaction of laser-induced cavitation bubbles with composite surfaces. Journal of applied physics, 2003. 94(5): p. 2809-2816.

[34] Turangan, C., et al., Experimental and numerical study of transient bubble-elastic membrane interaction. Journal of Applied Physics, 2006. 100(5): p. 054910.

[35] Aghdam, A.H., et al., Effect of the viscosity on the behavior of a single bubble near a membrane. International Journal of Multiphase Flow, 2012. 47: p. 17-24.

[36] Kodama, T. and Y. Tomita, Cavitation bubble behavior and bubble–shock wave interaction near a gelatin surface as a study of in vivo bubble dynamics. Applied physics B, 2000. 70(1): p. 139-149.

[37] Yuan, H., H. Oguz, and A. Prosperetti, Growth and collapse of a vapor

bubble in a small tube. International Journal of Heat and Mass Transfer, 1999. 42(19): p. 3643-3657.

[38] Ory, E., et al., Growth and collapse of a vapor bubble in a narrow tube. Physics of fluids, 2000. 12(6): p. 1268-1277.

[39] Kenning, D., et al., Confined growth of a vapour bubble in a capillary tube at initially uniform superheat: experiments and modelling. International journal of heat and mass transfer, 2006. 49(23): p. 4653-4671.

[40] Yin, L., et al., Experimental investigation on bubble confinement and elongation in microchannel flow boiling. Experimental thermal and fluid science, 2014. 54: p. 290-296.

[41] Jansen, E.D., et al., Partial vaporization model for pulsed mid-infrared laser ablation of water. Journal of applied physics, 1995. 78(1): p. 564-571.

[42] Zeng, L., J. Klausner, and R. Mei, A unified model for the prediction of bubble detachment diameters in boiling systems—I. Pool boiling. International Journal of Heat and Mass Transfer, 1993. 36(9): p. 2261-2270.

[43] Padilla-Martinez, J., et al., Optic cavitation with CW lasers: A review. Physics of Fluids, 2014. 26(12): p. 122007.

[44] Aghdam, A.H., et al., Experimental study on the dynamics of an oscillating bubble in a vertical rigid tube. Experimental Thermal and Fluid Science, 2015. 60: p. 299-307.

[45] Wang, G., et al., A laser induced cavitation pump. Journal of

Micromechanics and Microengineering, 2004. 14(7): p. 1037.

[46] Stachowiak, J.C., et al., Piezoelectric control of needle-free transdermal drug delivery. Journal of Controlled Release, 2007. 124(1): p. 88-97.

[47] Jang, H.-j., et al., Towards clinical use of a laser-induced microjet system aimed at reliable and safe drug delivery. Journal of biomedical optics, 2014. 19(5): p. 058001-058001.

[48] Walsh, J.T. and T.F. Deutsch, Er: YAG laser ablation of tissue: measurement of ablation rates. Lasers in surgery and medicine, 1989. 9(4): p. 327-337.

[49] Walsh, J.T., T.J. Flotte, and T.F. Deutsch, Er: YAG laser ablation of tissue: effect of pulse duration and tissue type on thermal damage. Lasers in surgery and medicine, 1989. 9(4): p. 314-326.

[50] Hibst, R. and R. Kaufmann, Effects of laser parameters on pulsed Er-YAG laser skin ablation. Lasers in medical science, 1991. 6(4): p. 391-397.

[51] Hohenleutner, U., et al., Fast and effective skin ablation with an Er: YAG laser: determination of ablation rates and thermal damage zones. Lasers in surgery and medicine, 1997. 20(3): p. 242-247.

[52] Schramm-Baxter, J., J. Katrencik, and S. Mitragotri, Jet injection into polyacrylamide gels: investigation of jet injection mechanics. Journal of biomechanics, 2004. 37(8): p. 1181-1188.

[53] Komaragiri, U., M. Begley, and J. Simmonds, The mechanical response of freestanding circular elastic films under point and pressure loads. Transactions of the ASME-E-Journal of Applied Mechanics, 2005.

72(2): p. 203-212.

[54] Jang, H.-j., et al., Laser-induced microjet injection into preablated skin for more effective transdermal drug delivery. Journal of biomedical optics, 2014. 19(11): p. 118002-118002.

[55] Norlén, L., Molecular structure and function of the skin barrier, in Percutaneous Penetration Enhancers Chemical Methods in Penetration Enhancement. 2015, Springer. p. 39-42.

[56] Nelson, J.S., et al., Enhances In Vitro Percutaneous Transport of Drugs. 1991.

[57] Koenz, F., et al. Thermal and mechanical damage of corneal tissue after free-running and Q-switched mid-infrared laser ablation. in Europto Biomedical Optics' 93. 1994. International Society for Optics and Photonics.

[58] Vogel, A., et al., Energy balance of optical breakdown in water at nanosecond to femtosecond time scales. Applied Physics B: Lasers and Optics, 1999. 68(2): p. 271-280.

[59] Ith, M., et al., Dynamics of laser-induced channel formation in water and influence of pulse duration on the ablation of biotissue under water with pulsed erbium-laser radiation. Applied Physics B: Lasers and Optics, 1994. 59(6): p. 621-629.

[60] Jansen, E.D., et al., Effect of pulse duration on bubble formation and laser-induced pressure waves during holmium laser ablation. Lasers in surgery and medicine, 1996. 18(3): p. 278-293.

[61] Kang, H.W., et al., Dependence of calculus retropulsion on pulse

duration during Ho: YAG laser lithotripsy. Lasers in surgery and medicine, 2006. 38(8): p. 762-772.

[62] Fogg, D.W. and K.E. Goodson, Bubble-induced water hammer and cavitation in microchannel flow boiling. Journal of Heat Transfer, 2009. 131(12): p. 121006.

[63] Herbig, M.E., et al., A custom tailored model to investigate skin penetration in porcine skin and its comparison with human skin. European Journal of Pharmaceutics and Biopharmaceutics, 2015. 95: p. 99-109.

[64] Kadam, V., et al., A review on needle-free injection system. J Pharm Pharm Sci, 2014. 3(3): p. 763-780.

[65] Hogan, N.C., et al., Needle-free delivery of macromolecules through the skin using controllable jet injectors. Expert opinion on drug delivery, 2015. 12(10): p. 1637-1648.

[66] Jeandidier, N. and S. Boivin, Current status and future prospects of parenteral insulin regimens, strategies and delivery systems for diabetes treatment. Advanced drug delivery reviews, 1999. 35(2): p. 179-198.

[67] Pharm. D, D.L.B. and F. Pass, Delivery of insulin by jet injection: recent observations. Diabetes technology & therapeutics, 2001. 3(2): p. 225-232.

[68] Cefalu, W.T., Evolving strategies for insulin delivery and therapy. Drugs, 2004. 64(11): p. 1149-1161.

[69] Engwerda, E.E., C.J. Tack, and B.E. De Galan, Needle-free jet injection of rapid-acting insulin improves early postprandial glucose control in

patients with diabetes. Diabetes Care, 2013. 36(11): p. 3436-3441.

[70] Hoffman, P., et al., A model to assess the infection potential of jet injectors used in mass immunisation. Vaccine, 2001. 19(28): p. 4020-4027.

[71] Dierickx, C.C., et al., Micro-fractional ablative skin resurfacing with two novel erbium laser systems. Lasers in surgery and medicine, 2008. 40(2): p. 113-123.

[72] Lee, W.-R., et al., Impact of different vehicles for laser-assisted drug permeation via skin: full-surface versus fractional ablation. Pharmaceutical research, 2014. 31(2): p. 382-393.

[73] Nelson, J.S., et al., Mid-infrared laser ablation of stratum corneum enhances in vitro percutaneous transport of drugs. Journal of investigative dermatology, 1991. 97(5): p. 874-879.

[74] Hædersdal, M., et al., Fractional CO2 laser-assisted drug delivery. Lasers in surgery and medicine, 2010. 42(2): p. 113-122.

[75] Genina, E.A., et al., Fractional laser microablation of skin aimed at enhancing its permeability for nanoparticles. Quantum Electronics, 2011. 41(5): p. 396-401.

[76] Lee, W.-R., et al., Laser-assisted topical drug delivery by using a low-fluence fractional laser: imiquimod and macromolecules. Journal of controlled release, 2011. 153(3): p. 240-248.

초 록

바늘 주사를 통한 약물 주입은 경피 타입의 약물 전달 방식으로 저렴한 비용과 효율로 인해서 현재까지 널리 사용되고 있다. 하지만 바늘 주사의 경우 잠재적으로 알려진 단점인 주사 공포증, 고통, 의료 폐기물, 재사용으로 인한 감염 등으로 인해서 기존의 존재하던 바늘 기반의 약물 전달 장치를 대체하기 위한 요구가 존재해 왔다.

경피 타입의 약물 전달 시스템은 확산 및 침투 방식과 같이 여러 종류의 화학 및 물리적 처리 과정을 활용하여 피부 장벽을 투과하도록 하는데 목적이 있다. 그 중에서 액체 젯 방식은 효율적인 약물 전달 방식 중 하나로써 주목을 받았다. 하지만 기대와는 다르게, 액체 젯 인젝터는 약물 주입시 되튀김으로 인한 상호 감염의 문제가 있으며, 충분히 빠르고 얇은 젯이 사용되지 않는 경우에 결과적으로 전달 투여량 및 투여 깊이에 대한 신뢰도가 낮게 되고, 통증 감소 효과가 거의 없는 것으로 확인 되었다.

본 연구에서는 레이저 유도 마이크로젯을 도입하여 효율적인 경피 약물 전달 시스템 구축에 관하여 보고 하였다. 이와 같은 마이크로젯 인젝터 시스템은 약물을 가속시켜서 바늘 없이 피부 내부로 전달 시키며 기존의 액체 젯 방식의 문제점을 극복하는데 목적이 있다. 펄스당 젯의 지름과 양을 줄이고 반복적으로 약물을 주입 함으로써 투여량 및 투여 깊이에 대한 신뢰도를 확보하였고 되튀김 현상을 최소화 하여 성능 최적화를 달성하였다.

한편, 약물 주입 과정에 관한 분석을 위하여 버블 팽창 및

마이크로젯 생성 과정을 초고속 카메라를 활용하여 연구함으로써 심도 있는 분석이 수행되었다. 이를 통해 개발된 마이크로젯 인젝터의 주요한 구동 원리를 이해 할 수 있었다. 또한 현재의 약물 전달 방식에 대한 효율은 동물 피부를 활용한 실험을 통해 평가하였다.

결론적으로 약물 전달 시스템에 관한 전반적인 사항에 대한 논의가 진행되었으며, 일반적인 임상 적용에 적합한 인젝터를 만들기 위한 마이크로 젯 분사 및 반복 분사 과정의 향상이 이루어졌다. 따라서 상기 결과로부터 신뢰성 있고 최적화된 마이크로젯 인젝터 시스템 설계를 위한 지침을 제공하였다.

주요어: 약물 전달 시스템, 경피 투여, 고통 최소화, 마이크로젯, 버블 역학
학 번: 2011-20747